Fabrication and Characterization of Electro-photonic Performance of Nanopatterned Organic Photovoltaics

Doo-Hyun Ko

A dissertation submitted to the faculty of the University of North Carolina at Chapel Hill
in partial fulfillment of the requirements for the degree of Doctor of Philosophy
in the Department of Chemistry.

Chapel Hill
2010

Approved by

Advisor: Professor Edward T. Samulski

Reader: Professor Rene Lopez

Reader: Professor Wei You

Professor Valerie Ashby

Professor Thomas J. Meyer

ABSTRACT

DOO-HYUN KO
Fabrication and Characterization of Electro-photonic Performance of
Nanopatterned Organic Photovoltaics
(Under the direction of Professor Edward T. Samulski)

Incommensurate length scales conspire to degrade photovoltaic efficiencies in organic photovoltaic (OPV) solar cells: The exciton diffusion length is of order 10 nm while the absorption length is typically more than one order of magnitude larger. And when this discrepancy is ameliorated by co-precipitating a bicontinuous donor and accepter phase to form a bulk heterojunction (BHJ), the tortuous carrier transport path and the electric field distribution across the nano-phase separated components become problematic. Photonic crystal solar cells have the potential for addressing the disparate length scales in polymer photovoltaic materials, thereby confronting the major challenge in solar cell technology: efficiency. One must achieve simultaneously an efficient absorption of photons with effective carrier extraction. Unfortunately the two processes have opposing requirements. Efficient absorption of light calls for thicker PV active layers whereas carrier transport always benefits from thinner ones, and this dichotomy is at the heart of an efficiency/cost conundrum that has kept solar energy expensive relative to fossil fuels.

This dichotomy persists over the entire solar spectrum but increasingly so near a semiconductor's band edge where absorption is weak. I report a 2-D photonic crystal geometry that enhances the efficiency of organic photovoltaic cells relative to conventional planar cells. The PC geometry is developed by patterning an organic photoactive bulk

heterojunction via PRINT^{TM}, a nano-embossing method that lends itself to large area fabrication of nanostructures. The photonic crystal cell morphology generally increases photocurrents, and particularly through the excitation of resonant modes near the band edge of the OPV material. The device performance of the photonic crystal cell showed a nearly doubled increase in efficiency relative to conventional planar cell designs. Replication flexibility for various shapes of nanopatterns and materials by PRINT^{TM} provides further feasibility for PC cell fabrication. The optical interference of PC cells depending on device architecture was investigated theoretically and experimentally.

Moreover, the PRINT provides flexibility to fabricate PC geometry for inverted OPV (iOPV) as well as standard OPV. For the PC behavior, the large contrast of refractive index of nanopatternes in the adjacent material is essential. Here, the incorporated layer for the PC behavior affects the device performance electrically as well as optically. In particular, incorporating UV-sensitive electron transport layers (ETL) into organic bulk heterojunction photovoltaic devices dramatically impacts short-circuit current (J_{sc}) and fill factor characteristics. Resistivity changes induced by UV illumination in the ETL of inverted BHJ devices suppress bimolecular recombination producing up to two orders of magnitude changes in J_{sc}. Electro-optical modeling and light intensity experiments effectively demonstrate that bimolecular recombination, in the form of diode current losses, controls the extracted photocurrent and is directly dependent on the ETL resistivity.

ACKNOWLEDGEMENTS

"It's a time to qualify for a Ph.D. when one knows what one really doesn't know."

During the 5 years when I spent to realize this instrumental fact, I am truly indebted to a number people who have helped me at UNC.

Foremost, I recognize the intellectual and moral support of my advisor, Professor Edward T. Samulski. He has been an invaluable mentor to me over the past five years. His many scientific ideas have stimulated me to explore interdisciplinary study, and his encouragement provided fortitude to my life as well as my research. Also, my wife and I owe many thanks to Mrs. Samulski for her support to our family.

I would also like to thank Professor Wei You and Professor Rene Lopez for their support and stimulating discussion. I extremely feel that they are 'co-advisors'. Their intriguing ideas have supported me to overcome many challenges. I would like to thank Professor Joseph M. Desimone for allowing me to follow his creative approach and conduct my research using PRINT technology.

I was very pleased to work with the many talented members of the Samulski lab and the You lab during my time at UNC. I am grateful to Lei Zhang and Walter Schenck for their support, advice and friendship that contributed to my graduation. I would like to give many thanks to Stuart Williams, Ralph House and Jeremy Niskala for their friendship, advice, supports, and good scientific discussion.

A special thank to John R. Tumbleston for his unwavering support should also be given. John's hard work and dedication to his research set an excellent example for me to follow, and his passion for science is obviously contagious.

I would like to thank Professor Jung-Il Jin at Korea University for his invaluable support. His enthusiasm for science has been a role model to me in my life.

I would like to take an opportunity to express my appreciation to people in LG LCD. Dr. In-Jae Chung, CTO, and Dr. In-Byung Kang are gratefully acknowledged for supporting and allowing me to study at UNC. I would like to thank Dr. Nam-yang Lee, Ki-Yong Kim, and Dr. Chang-Wuk Han for their precious advice. I would like to thank Dr. Hyun-Chul Choi to be one of my biggest supporters in Korea. His encouragement and invaluable advice convinced me to obtain a Ph.D. I also thank Dr. Jun-Ho Lee, Sung-Jun Bae, Kyoung-Man Kim, Jong-Hyun Park, and Jun-Seok Lee for their assistance, support and friendship.

Thanks also to my colleagues at UNC who have gone above and beyond to help make life in a graduate school a wonderful experience and especially the members of Korea Chemical Association Society (Dr. Changjun Lee, Dr. Sangwuk Woo, Dr. Jaephil Choi, Dr. Myoungryong Choi, Dr. Jaeho Shin, Dr. Jinwoo Park, Dr. Wonhee Jeong, Myoungryul, Changsun, Sungjin, Ayeon, Sooyeon). Many thanks my buds to In-Yub, Sang-Hyun, Hyun-Jae, Joon-Ho, Han-Joon, Dong-Kyoung, and Young-Joon for their lifelong friendships.

For more reasons than one, I could not have completed my Ph.D. without the support and encouragement of my loving family. Without the life-long encouragement and support from my parents, I never would have made it this far. My parents-in-law have also been instrumental in supporting me in my pursuit of a Ph.D. I have additionally been blessed with my wonderful brothers, sisters-in-law, brothers-in-law and lovely nephews.

Last, but certainly not least, I want to thank to Jeung-Eun, my wife for her love and never-dying belief in my ability to complete my Ph.D. Her support has made Chapel Hill to be one of the most memorable places in my life. I dedicate this thesis to God who has been supervising and leading my life.

To God

To my grandmother in heaven

To my family for love and support

TABLE OF CONTENTS

LIST OF TABLES

Table

LIST OF FIGURES

Figure

LIST OF ABBREVIATIONS AND SYMBOLS

APFO3	Poly[(9,9-dioctylfluorenyl-2,7-diyl)-alt-5,5-(40,70-di-2-thienyl-20,10,30-benzothiadiazole)]
BCP	Bathocuproine
BHJ	Bulk heterojuction
BR	Bimolecular recombination
CuPC	Copper phthalocyannine
DEAP	2,2-diethoxyacetophenone
DMA	dimethacrylate
ETL	Electron transporting layer
FF	Fill factor
FIB-CVD	Focused-ion-beam chemical-vapor-deposition
G	Exciton generation rate
GPC	Gel permeation chromatography
HOMO	Highest occupied molecular orbital
iOPV	Inverted organic photovoltaic
IPCE	Incident-photon-to-current conversion efficiency
IQE	Internal quantum efficiency
IR	Infrared
ITO	Indium tin oxide

J_D	Dark current density
J_L	Illuminated current density
J_{ph}	Photocurrent density
J_{sat}	Saturated photocurrent density
J_{sc}	Short circuit current
k_{diss}	Dissociation rate constant
k_f	Decay rate constant
LUMO	Lowest unoccupied molecular orbital
MDMO-PPV	Poly(2-methoxy-5-(3',7'-dimethyl-octyloxy))-p-phenylene vinylene
MEH-PPV	Poly(2-methoxy-5-(2'-ethyl-hexyloxy)-1,4-phenylene vinylene)
MIM	Metal-insulator-metal
M_n	Number of molecular weight
NIR	Near infrared
OPV	Organic photovoltaic
P3HT	Poly(3-hexylthiophene)
PC	Photonic crystals
PCBM	[6,6]-phenyl-C61-butyric acid
PEDOT:PSS	Poly(3,4-ethylenedioxythiophene):poly(styrenesulfonate)
PFPE	Perfluoropolyether
P_{inc}	Incident power density
PRINT	Pattern replication in non-wetting technology
PTCBI	3,4,9,10-perylenetetracarboxylic-bis-benzimidazole
PTFE	Polytetrafluoroethylene

PVDF	Polyvinylidene fluoride
QD	Quantum Dot
R_s	Series (or serial) resistance
R_{shunt}	Shunt resistance
SEM	Scanning electron microscopy
SERS	Surface enhanced raman spectroscopy
SPP	Surface plasmon polariton
T	Temperature
TDPTD	Thermally deprotectable poly thiophene derivative
THF	Tetrahydrofuran
TiO_x	amorphous titanium oxide
TiO_2	Titanium oxide
UV	Ultra violet
V_{app}	Applied voltage
V_{oc}	Open circuit voltage
nc-ZnO	Nanocrystalline zinc oxide
γ	Recombination strength
η_A	Absorption efficiency
η_{CC}	Charge collection efficiency
η_{CT}	Charge transfer efficiency for hole-electron separation
η_{Diff}	Exciton diffusion efficiency
η_{IQE}	Internal quantum efficiency
η_P	Power conversion efficiency

η_{TR}	Carrier transport efficiency
$< \varepsilon >$	Spatially averaged dielectric constant
μ_e	Electron mobility FIB-CVD (focused-ion-beam chemical-vapor-deposition
μ_h	Hole mobility

Chapter I

LITERATURE REVIEW OF CURRENT ORGAINC PHOTOVOLTAIC CELLS WITH LIGHT TRAPPING SYSTEM AND ELCECTRICAL MODELING

1.1 Mechanism in Organic Photovoltaic Cells

Concerns over global climate change, local air pollution, and resource scarcity make solar cells an increasingly attractive energy supply technology. Although organic photovoltaic cells, (OPV) which use conductive polymers, have attracted much attention for their potential application as a flexible, portable, and low cost energy source, the reported power conversion efficiency of organic photovoltaic cells is less than 10%.[1]

The photocurrent generation mechanism of OPV is illustrated in Figure 1.1, and it is composed of five steps: (1) Light absorption for exciton generation, (2) Exciton diffusion, (3) Charge transfer for exciton dissociation, (4) Carrier transport towards the electrodes, (5) Charge collection at the respective electrodes.[2]

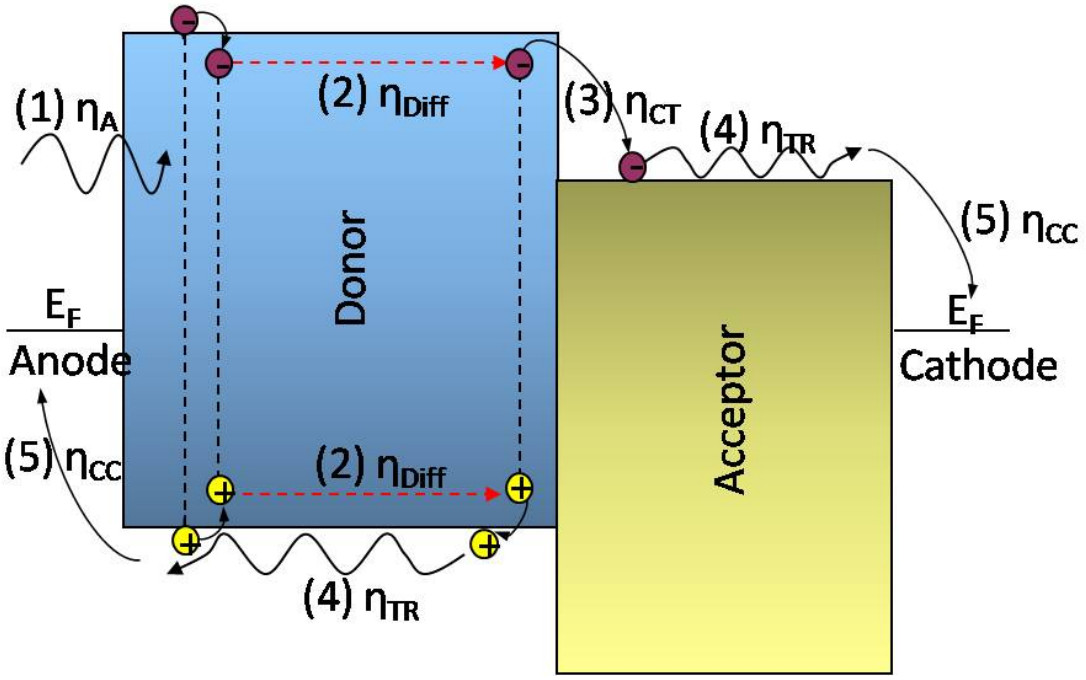

Figure 1.1. Steps in the photocurrent generation process for OPV[2]. The internal quantum efficiency of OPV is defined as the product of the five efficiencies at each step.

1) Absorption efficiency (η_A): OPV devices start to work by absorbing the incident light and creating excitons in p-type donor material. The η_A depends on the value of the optical absorption coefficient as well as on the thickness of the donor material. Thus, thicker donor can be used to absorb the incident light leading to create more excitons. Absorption lengths of the typically used photoactive materials are known to be 100 ~ 200 nm.[3]

2) Exciton diffusion efficiency (η_{Diff}): The photogenerated excitons are strongly bound by the Columbic attraction in donor material, and the binding energy is known to be approximately 0.3~0.4eV in conjugated polymers.[2] The created excitons diffuse into the interface between donor and acceptor layer as long as recombination processes do not occur. The exciton diffusion lengths in most donor materials are between 5nm and 15nm, and thus the created excitons can travel only a few nm.[4, 5] Due to various recombination processes, the exciton diffusion efficiency is below 1.

3) Charge transfer efficiency for hole-electron separation (η_{CT}): If the generated excitons transfer at the interface between donor and acceptor, the excitons dissociate into a hole in donor material and an electron in acceptor material. Since the separation process is very fast (~100fs)[6], no other decay mechanism can compete, so this efficiency is close to unity.

4) Carrier transport efficiency (η_{TR}): Although the dissociation of excitons occurs, the separated charge carriers are still bound due to the Coulomb force between electron and hole. Under typical operation conditions, the photon-to-free-electron conversion efficiency is, therefore, not maximal. If the dissociated excitons can overcome the

Coulombic attraction barrier by an electric field in the devices, the charge carriers are set free and transport towards the anode and the cathode. However, the recombination of the free photogenerated charge carriers might further limit the carrier transport efficiency. For instance, when the transit time of the free charge carriers to the electrodes is longer than their life time, recombination is dominant, resulting in reduced carrier transport efficiency.[7] From this standpoint, the thickness of donor and acceptor material is a critical parameter for the carrier transport efficiency.

5) Charge collection efficiency (η_{CC}): The free carriers arriving at the electrodes become collected and generate currents via an external circuit in the device. When E_F (cathode) is lower than E_{LUMO} (acceptor) and E_F (anode) is higher than E_{HOMO} (donor), the electrodes extract all photogenerated free charge carriers, and $\eta_{CC} \approx 1$.

Therefore, the internal quantum efficiency (η_{IQE}) of OPV can be defined as the product of the five efficiencies mentioned above.

$$\eta_{IQE} = \eta_A \, \eta_{Diff} \, \eta_{CT} \, \eta_{TR} \, \eta_{CC} \tag{1.1}$$

where η_A is the absorption efficiency of light for exciton generation, η_{Diff} is the exciton diffusion efficiency to a dissociation site, η_{CT} is the charge transfer efficiency for hole-electron separation, η_{TR} is carrier transport efficiency toward the electrodes after free charge carrier generation, and η_{CC} is the charge collection efficiency at the respective electrodes.

Considering the working theory of OPV, however, an inherent tradeoff is observed among absorption efficiency (η_A), exciton diffusion efficiency (η_{Diff}) and carrier transport efficiency (η_{TR}) which has opposing requirements for higher performance of OPV. For instance, the photoactive layer should be sufficiently thick to absorb incident light for higher absorption efficiency (η_A) whereas, for higher diffusion efficiency (η_{Diff}), it should be thin enough to allow charges to diffuse into the interface where exciton dissociation occurs. Also the thinner photoactive layer leads to a strong internal electric filed where the photogenerated carriers can move into the electrodes with less recombination, and results in higher carrier transport efficiency (η_{TR}). This dichotomy is at the heart of an efficiency/cost conundrum that has kept solar energy from OPV expensive relative to fossil fuels. Therefore, these efficiencies should be optimized to achieve high performance of OPV.

1.2 Bulk Heterojunction OPV

In order to solve the problem of limited exciton diffusion length in the photoactive material, Yu et al[5] and Halls et al.[4] proposed the bulk heterojunction (BHJ) OPV where the donor and acceptor materials are intermixed together and the active interfaces between donor and acceptor distribute throughout the bulk (Figure 1.2). Here, the nanoscopic mixing of donor and acceptor is designed to overcome the short exciton diffusion length (~10 nm) such that all excitons are created within a diffusion length of an interface between donor and acceptor. Also, large interfacial area for charge separation is made in bulk heterojunction morphology, and thus charge separation is expected to occur with unit efficiency.

1.3 Efficiency of OPV cell

Since the BHJ morphology concept was proposed, the efficiency of OPV has been abruptly improved. Recently, Chen et al.[8] reported 6.77% efficiency of OPV where the small band gap photoactive material was used to match the absorption spectrum of the material with the solar spectrum. For these devices, the BHJ morphology was incorporated into the device by blending the photoactive materials with acceptor materials, PCBM. In Figure 1.3, the performance of OPV is compared with other types of solar cells.[1] Although the efficiency of solar cells has been improved with the BHJ morphology strategy and small band gap materials, the OPV in Figure 1.3 shows relatively low efficiency compared to other types of solar cells, and thus has not reached commercially viable efficiencies of 10 %.

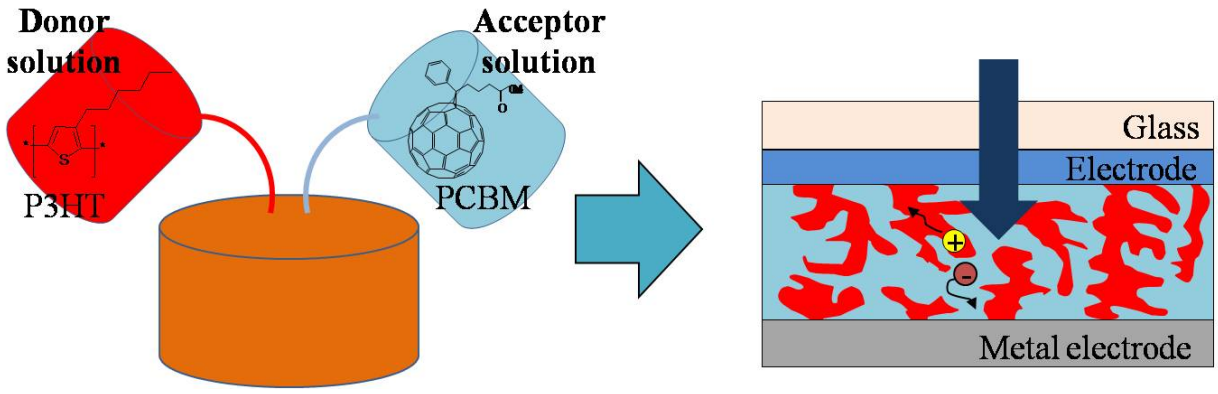

Figure 1.2. Scheme of Bulk heterojunction (BHJ) organic photovoltaic cells (OPV). Donor (P3HT, poly-(3-hexylthiophene)) and acceptor (PCBM, [6,6]-phenyl-C61-butyric acid) materials are mixed in a solution and incorporated into the device by spincasting the solution. Annealing the OPV after device fabrication helps to homogeneously intermix these materials (donor and acceptor) for the improved BHJ morphology and results in higher performance of OPV.

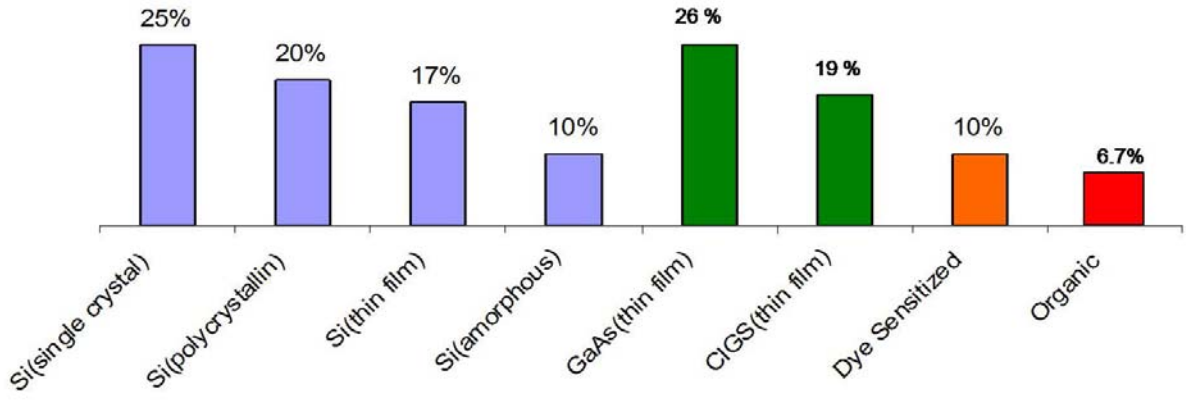

Figure 1.3. Efficiencies of various types of solar cells under the global AM1.5 spectrum (100 mW/cm^2).[1]

1.4 Requirements for high performance of OPV

The low efficiency of OPV is from the inherent tradeoff between absorption efficiency (η_A), exciton diffusion efficiency (η_{Diff}) and carrier transport efficiency (η_{TR}). Although the BHJ morphology could provide a strategy to handle the tradeoff between absorption efficiency (η_A), and exciton diffusion efficiency (η_{Diff}), the antithetical requirements for light absorption efficiency (η_{Diff}) and carrier transport efficiency (η_{TR}) still compete against one another. For instance, the strong internal electric field in the thinner photoactive material induces the photogenerated carriers to efficiently move to the electrodes with less recombination for higher carrier transport efficiency (η_{TR}) whereas the thinner photoactive layer leads to lower absorption in the photoactive layer with low absorption efficiency (η_A). Moreover, the tortuous carrier transport path in the BHJ morphology becomes a problematic barrier to improvements in the OPV efficiency.

1.5 Light trapping system in OPV

In order to solve these intrinsic problems, light trapping system for OPV has been investigated. As shown in Figure 1.4, a light trapping system can be designed to make multiple optical path lengths of incident light such that the chance to absorb the light in the photoactive material can be increased without increasing the thickness. Thus, the light trapping system for OPV offers the possibility of using thinner photoactive layers, which results in high carrier transport efficiency (η_{TR}) as well as high absorption efficiency (η_A).

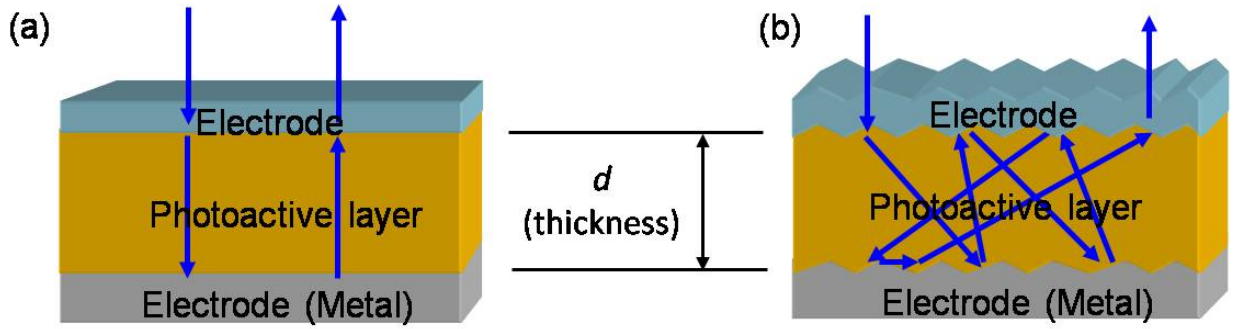

Figure 1.4. Schematic of light rays in the conventional OPV and (b) the OPV with a light trapping system which each have identical photoactive layer thickness (*d*). In the conventional OPV, incoming light strikes medium with reflection, and thus reflected light escape out of device. However, in the OPV with light trapping system, the reflected light is diffracted and can impinge again the surface of medium, thus reducing loss of light.

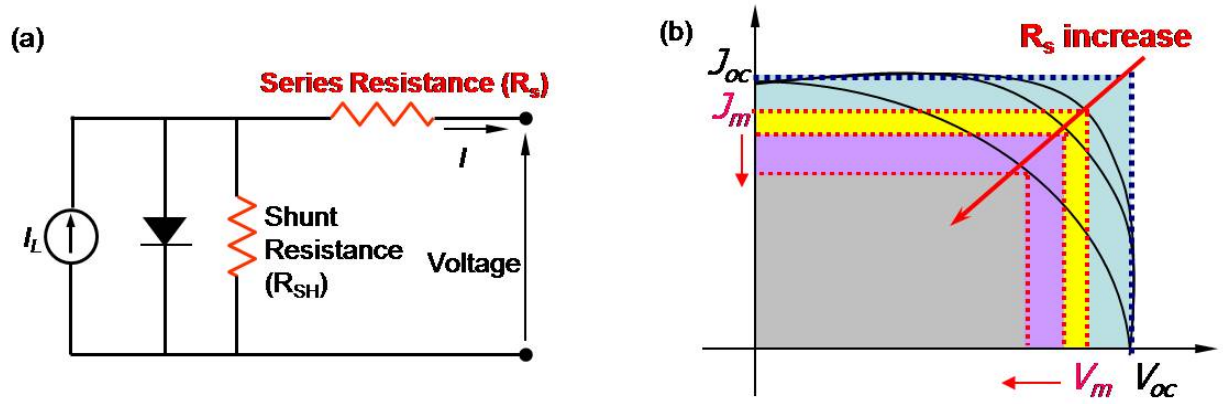

Figure 1.5. Equivalent circuit of OPV (a), and the effect of series resistance variation on I-V curve (b). Here, *FF* (Fill factor) is equal to $V_m J_m / V_{oc} J_{sc.}$

In addition, absorption enhancement without additional increase of the photoactive layer thickness lowers series resistance in OPV devices. For instance, an increase of photoactive layer thickness leads to raise the series resistance (R_s) because the photoactive layer thickness corresponds to one of the series resistance components in an equivalent circuit of the device in Figure 1.5 (a).[9] The main impact of high series resistance is to reduce *FF* (fill factor) as shown in Figure 1.5 (b), where excessively high values may also reduce the short-circuit current, which reduces the power conversion efficiency (η_P) in equation (1.2).

$$\eta_P = \frac{V_{oc} J_{sc} FF}{P_{inc}} \tag{1.2}$$

Where *FF* is the fill factor, V_{oc} is the open circuit voltage, J_{sc} is the short-circuit current density and P_{inc} is the incident power density.

Therefore it is desirable to make a thin photoactive layer with enhanced absorption. In sum, the light trapping system can offer a solution to the carrier transport length / optical absorption length mismatch with the reduced series resistance at the same time. The reduced electrical loss via recombination process and increased exciton dissociation probability in the device with thin photoactive layer are additional benefits of the light trapping system.

1.6 Overview of light trapping schemes in OPV

A variety of light trapping schemes have been advanced to offset the intrinsic problems including metal diffraction gratings,[10] corrector mirrors,[11] buried nano-electrodes,[12] microprism substrates,[13] and V-folded cell configurations.[14] The studies for absorption enhancement for OPV are summarized as below.

1.6.1 Correcting mirrors for OPV

In order to solve the mismatched scales between the optical absorption and the exciton diffusion length, Peumans et al.[11] reported the ultrathin bilayer OPV with a light trapping system. The cell was prepared by deposition of Copper phthalocyannine (CuPC) as a donor, 3,4,9,10-perylenetetracarboxylic-bis-benzimidazole (PTCBI) as an acceptor and bathocuproine (BCP) as electron blocking layer. Here, the small aperture with silver (Ag) layer was placed on the substrate, and the concentrated radiation thorough the aperture could be formed via multiple reflections between Ag cathode on the bottom and the aperture on the top as shown in Figure 1.6. The feasible thin photoactive layer due to light trapping system lower series resistance with less recombination of carriers and allow for improved power conversion efficiency under intense illumination from 1.0% ± 0.1% to 2.4% ± 0.3%. Also, the Winston-type collectors[11] were proposed for a large area and low-cost light trapping system for OPV.

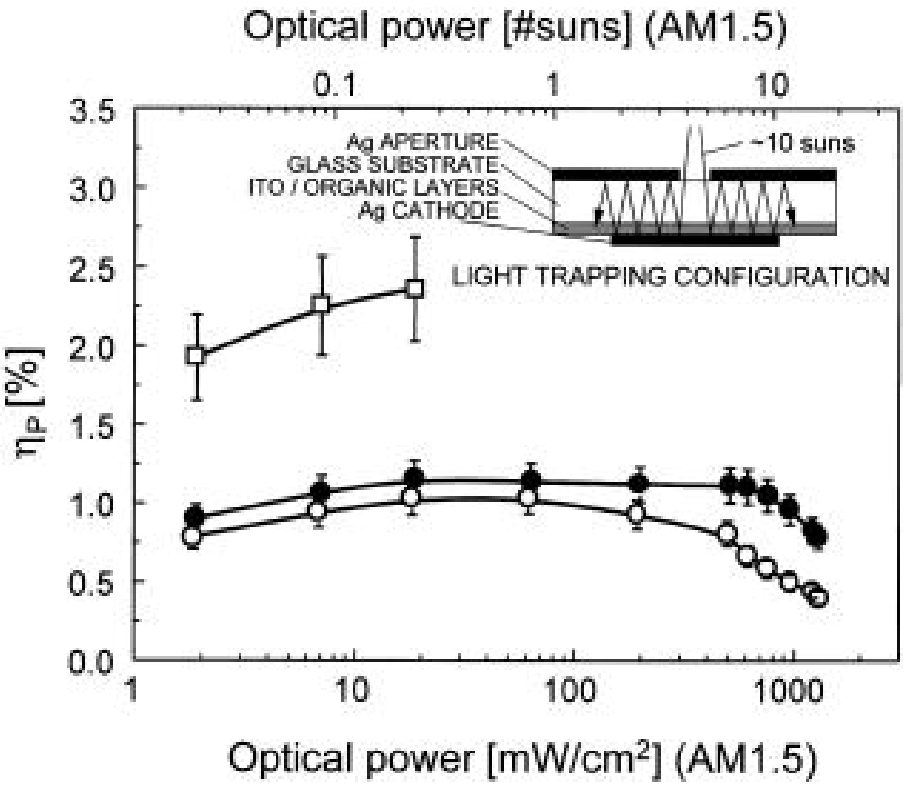

Figure 1.6. Dependence of the power conversion efficiency on the incident optical power density of an ITO/150 Å CuPc/60 Å PTCBI/150 Å (BCP:PTCBI)/800 Å Ag (filled circles) and an ITO/300 Å CuPc/300 Å PTCBI/150 Å (BCP:PTCBI)/800 Å Ag (open circles) PV cell. The open squares are the measured efficiencies of a ITO/60 Å CuPc/60 Å PTCBI/150 Å (BCP:PTCBI)/800 Å Ag PV cell with light trapping. The optical power was calculated as the average power over the total device area. Inset: schematic illustration of the PV cell used in the light trapping configuration. (Reprinted with permission from reference 11. Copyright © 2000, American Institute of Physics.)

1.6.2 Optical spacer for OPV

Heeger et al.[15] reported that the introduction of a highly conductive optical spacer can enhance absorption. In Figure 1.7, optical interference can be tuned by incorporating the TiO_x optical spacer between the photoactive layer (P3HT:PCBM) and aluminum (Al). Also the TiO_x[15] was demonstrated to work as an electron acceptor and a transport material. For the device with the optical spacer layer, the short circuit current increased by ~50%, and the corresponding power-conversion efficiency was 5.0 %. (J_{sc} = 11.1 mA/cm^2, V_{oc} = 0.61 V, and FF = 0.66). In addition to optical enhancement in the devices, recent studies have shown that the optical spacer plays an important role to improve electronic interface between the photoactive layer and Al.[16, 17]

1.6.3 Diffraction grating for OPV

The diffractive optical structure has been investigated for silicon solar cells.[18, 19] Roman et al. first tried to incorporate soft embossed grating structure into an OPV.[10] However, due to the low aspect ratio of the prepared patterns, a large increase in absorption was not observed. However, slightly enhanced photocurrent was obtained in only IPCE (incident photon-to-current conversion efficiency) measurement. Niggeman et al.[12] further developed the diffraction grating patterns and showed enhanced absorption for the devices for polarized incident light. The absorption in photoactive layer with the diffraction grating structure was calculated to increase by 15% in TE polarization. However, the strong dependence on polarization of incident light for absorption enhancement demands structural optimization.

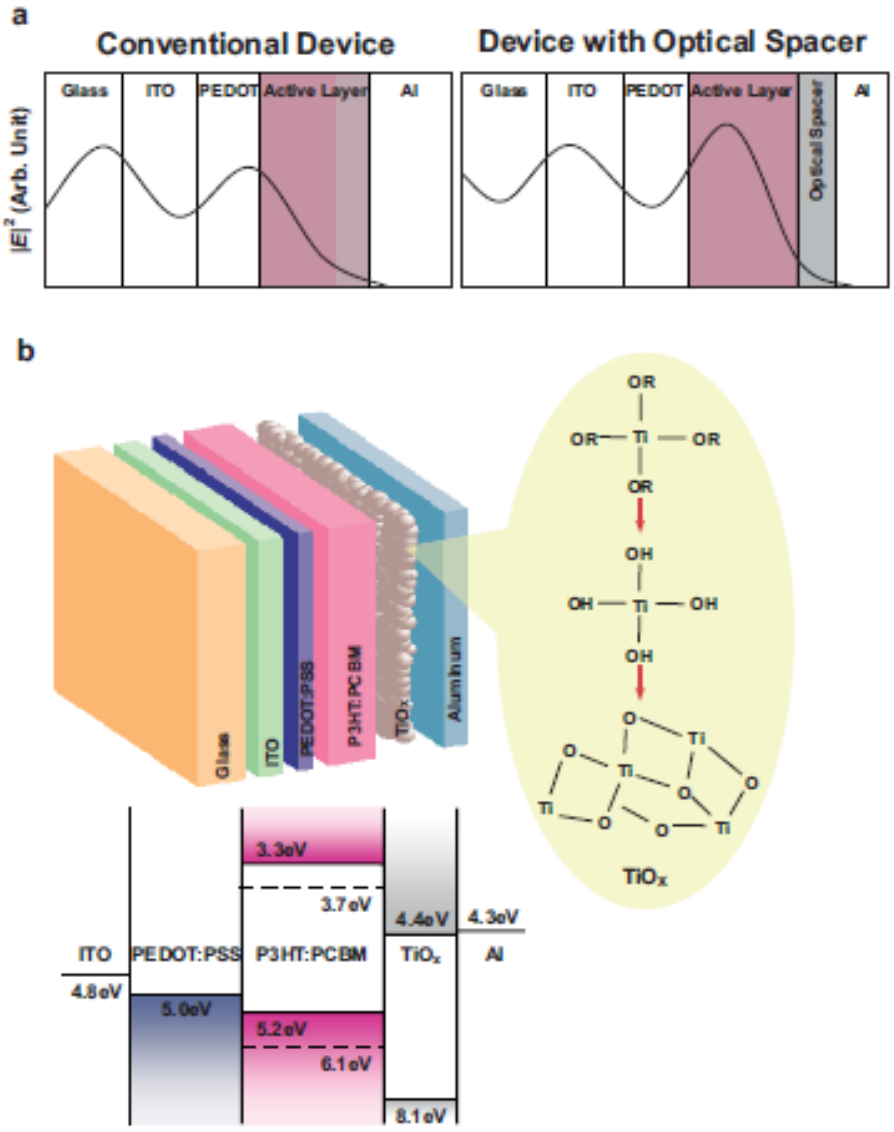

Figure 1.7. (a) Schematic representation of the spatial distribution of the squared optical electric field strength inside the conventional devices and the device with optical spacer. (b) The Device structure with optical spacer, TiO_x, and the energy levels of the components (PEDOT:PSS (Poly(3,4-ethylenedioxythiophene):Poly(styrenesulfonate)), P3HT:PCBM, TiO_x) in the prepared device. (Reprinted with permission from reference 15. Copyright © 2006 Wiley-VCH Verlag GmbH & Co. KGaA.)

1.6.4 Microprism substrates for OPV

In order to take advantage of increased optical path lengths for inclined incident angles, a folded solar structure was demonstrated by Niggemann et al.[13] As shown in Figure 1.8, the OPV devices were prepared on the prism substrate with a supporting metal grid and showed two-fold reflection of the incident light due to the microprism structure. Here, the deposition of uniform thickness of all organic materials (PEDOT:PSS, photoactive layer (P3HT:PCBM)) from solutions is challenging, and the film thickness in the valley of the substrate is usually thicker compared to the top of the substrate. Although the prepared microprism OPVs show relatively lower fill factor and lower open circuit voltage compared to the reference OPV, the short circuit current increased by ~60% due to the enhanced absorption in the photoactive layer. For the microprism OPV, V_{oc} = 0.455V, J_{sc} = 7mA/cm^2, FF = 0.35, η_P = 1.1%.

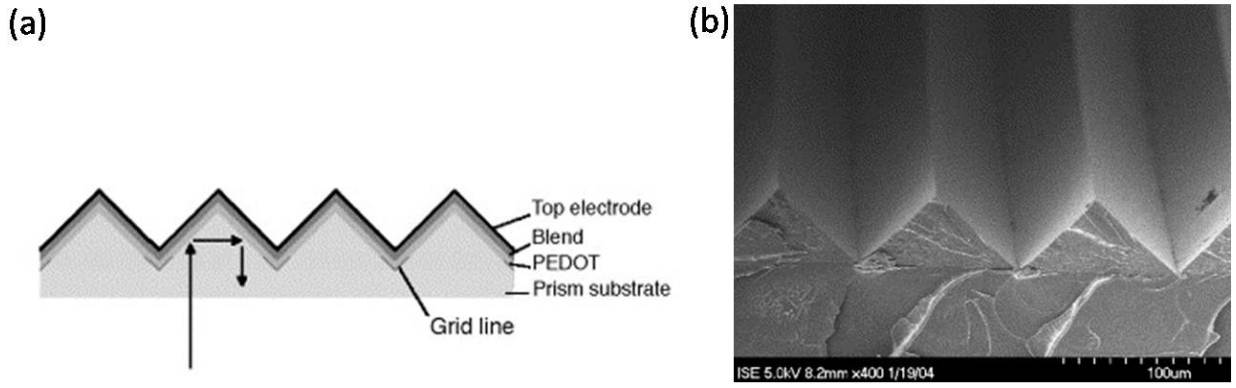

Figure 1.8. (a) Cross section of an organic microprism solar cell (b) Cross section SEM image of microprism structure. (Reprinted from reference 13, Copyright © 2006, with permission from Elsevier)

1.6.5 V-Folded cells for OPV

The longer optical path length of the incident light for OPV could be obtained by V-folded light trapping structures where the incident light can bounce multiple times as shown in Figure 1.9. Rim et al.[14] analyzed the enhanced optical path length in the V-folded OPV as a function of folding angles of V-shape. Here, about 50% increase of exciton generation was estimated, and finally 3.5% efficiency at 35° folding angle was obtained for V-folded P3HT:PCBM devices. However, the complicated processing and strong dependence of device performance on the folding angle become challenging and make the device fabrication more difficult.

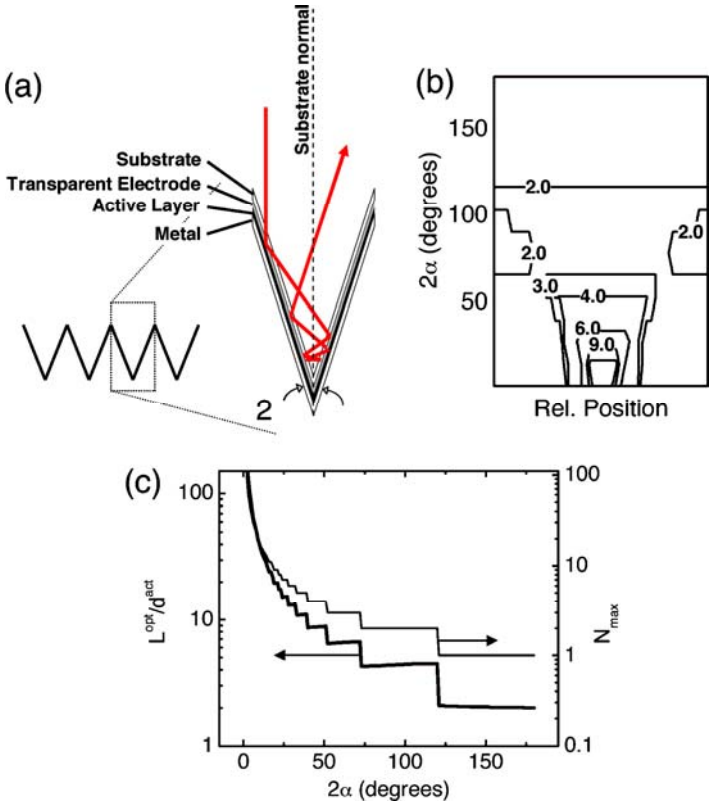

Figure 1.9. (a) The geometry of the V-shaped light trapping structure. The active layer is very thin compared to the thickness of the transparent substrate. (b) The density of ray bounces at each location of the V-shaped substrate compared to that in a planar configuration. (c) Optical path length normalized to the active layer thickness and the maximum number of bounces as a function of the opening angle 2α of the V shape. (Reprinted with permission from reference 14. Copyright © 2007, American Institute of Physics.)

The V-folded light trapping system was utilized to demonstrate reflective tandem cell by adjoining two single cells with V-shape folding as shown in Figure 1.10.[20] Here each single cell absorbs over different spectral ranges of incident light such that the non-absorbed light in one single cell can be reflected into another single cell. While bouncing the incident light in the V-folding tandem cell, each cell can absorb the light relevant to the absorption range of each photoactive layer. Also the multiple optical path length via the V-folding structure was additionally expected to enhance absorption. Tingstedt et al.[20] shows strong dependence on the folding angle for device performance, and finally the enhanced factor of power conversion efficiency was 1.8 ± 0.3.

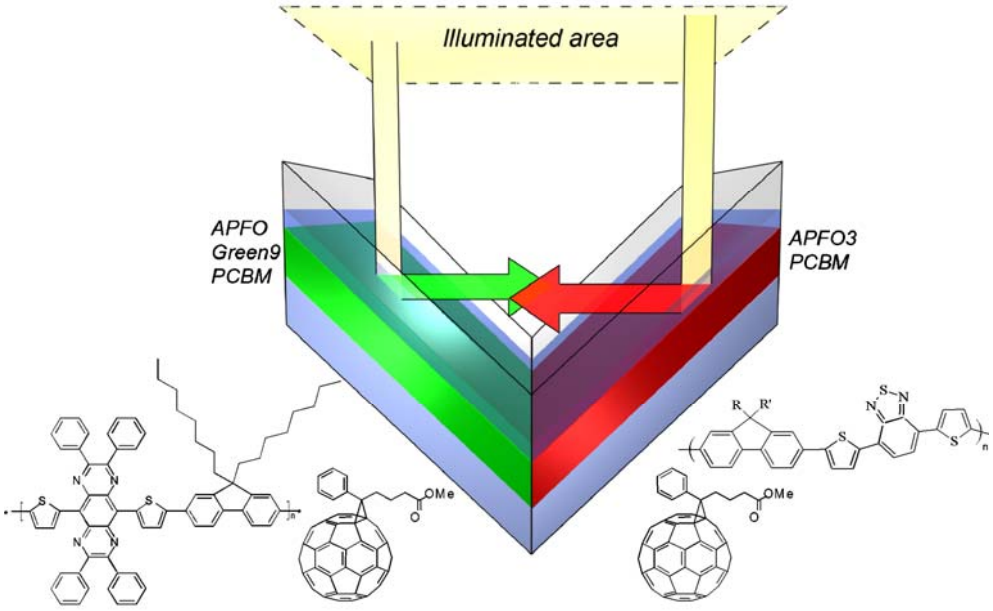

Figure 1.10. Scheme of the folded tandem cell and the chemical structures of the exploited alternating polyfluorenes APFO3, APFO Green-9, and the acceptor molecule PCBM. (Reprinted with permission from reference 20. Copyright © 2007, American Institute of Physics.)

1.6.6 Surface plasmon effect for OPV

Surface plasmons are confined light waves that propagate along the metal/dielectric interface. In order to excite surface plasmons in a resonant manner, the metal nanoparticles of gold[21] and silver[22] have been used to exhibit unique and tunable optical properties. As shown in Figure 1.11, Tvingstedt et al.[23] reported the enhanced absorption in polymer photovoltaic cells induced from surface plasmon effect, showing the change in absorption spectra due to the excitation of surface plasmon resonances. Here the photoactive layer (poly[(9,9-dioctylfluorenyl-2,7-diyl)-alt-5,5-(40,70-di-2-thienyl-20,10,30-benzothiadiazole)] (APFO-3) :PCBM) was deposited on the nano-structured Al substrate with 277 nm periodicity and 50 nm height, and Ti / TiO_x / PEDOT:PSS were sequentially deposited to fabricate the inverted OPV. The increased photocurrent was observed at the resonant region, showing the enhanced absorption was strongly dependent on the polarization of incident light.

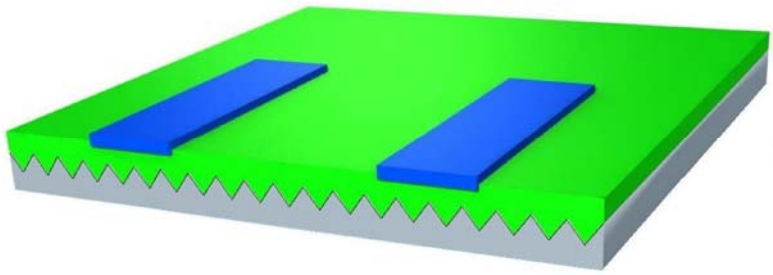

Figure 1.11. Schematic drawing of the inverted solar cell with nanostructured bottom cathode and transparent PEDOT:PSS top anode. In order to acheive a sufficient aspect ratio of the metal nanopatterns, a soft lithography technique for Al was chosen. (Reprinted with permission from reference 23. Copyright © 2007, American Institute of Physics.)

Absorption enhancement via plasmon effect was also seen for standard OPV. Morfa et al. [24] showed in Figure 1.12 that vapor deposited silver nanoparticles on ITO (indium tin oxide) layer induce plasmon enhanced absorption in photoactive layer (P3HT:PCBM). The enhanced short circuit currents via plasmon effect were strongly dependent on thickness of the deposited silver nanoparticle layer, and the resulting conversion efficiency of OPV devices increased from 1.3% ± 0.2% to 2.2% ± 0.1% by averagely 1.7 of improvement factor.

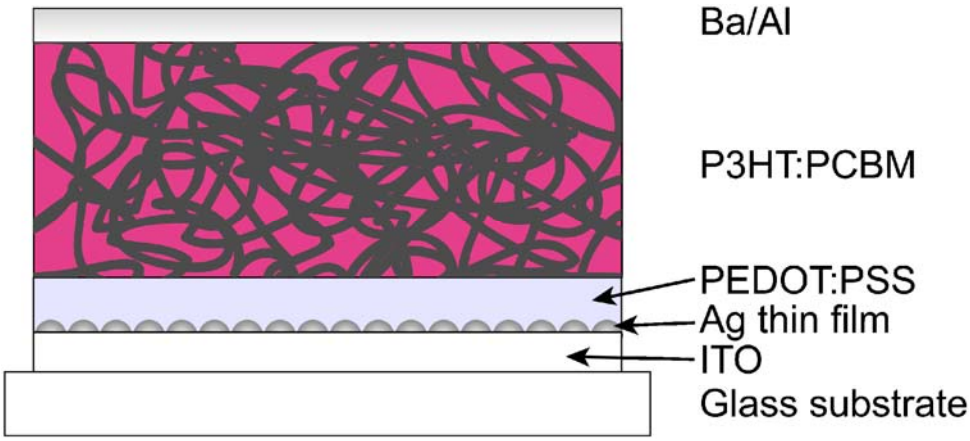

Figure 1.12. Schematic of the fabricated devices. Plasmonic enhanced OPV devices were prepared by deposition of a thin silver film on ITO. PEDOT:PSS and P3HT:PCBM were deposited by spincasting the solutions on the silver film, and barium (Ba) /aluminum were thermally evaporated onto the devices. (Reprinted with permission from reference 24. Copyright © 2008, American Institute of Physics.)

1.6.7 Photonic Crystals (PC) for OPV

In theory, photonic crystals (PC) are a powerful candidate for improving light trapping efficiency over a range of wavelengths as waveguides and low loss mirrors.[25] The PC can be designed to diffract incident beams into highly oblique angles. This approach can be used to offer longer optical path of light in a device. To date, however, only a limited

number of 1-D periodic photonic crystal designs have been reported presumably because of fabrication difficulties. [26, 27, 28.]

1.6.7.1 General concept for PC

Photonic crystals (PC) are periodic dielectric structures that have a band gap that forbids propagation of a certain frequency range of light. This property enables one to control light with amazing facility and produce effects that are impossible with conventional optics.

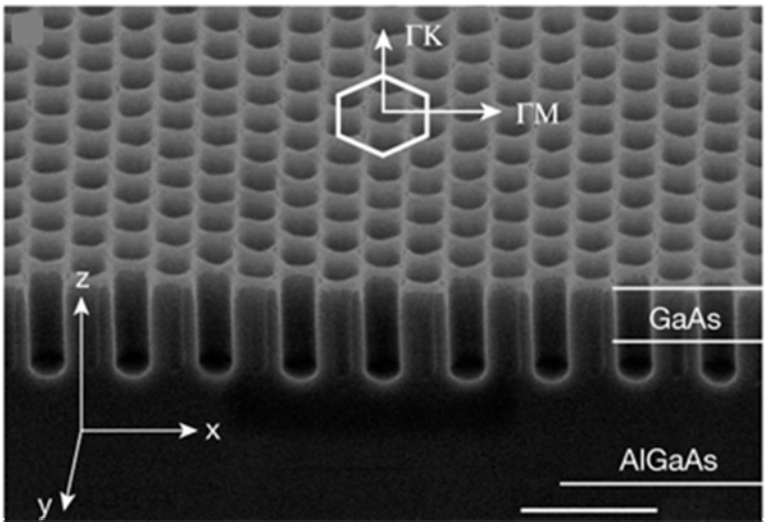

Figure 1.13. Two-dimensional photonic crystal composed of a square lattice of cylindrical air holes etched into a high-index material. The PC was fabricated using combination of electron beam lithography and reactive-ion-beam etching technique. Scale bar is 1 μm. (Reprinted by permission from Macmillan Publishers Ltd: Nature, reference 29, copyright © 2000.)

The PC can be made from a lattice of high-refractive index material within a medium with a lower refractive index as shown in Figure 1.13.[29] Here, it is possible to create energy levels in the photonic band gap by changing the size, periodicity and refractive index of dielectric materials. Basically, the critical parameters required for the PC are below.

(1) Periodic nanopatterns: The PC contains regularly interdigitating materials with high and low dielectric constant. When photons travel through the periodically patterned slab, certain wavelengths are not allowed to propagate through the structure. Therefore, for PC operating in the visible part of the spectrum, the periodicity of the photonic crystal structure has to be of the same length-scale as half the wavelength of the electromagnetic wave.

(2) Refractive index difference in adjacent materials: Since the basic physical phenomenon for PC is diffraction, the refractive index of the nanopatterns has to be sufficiently different for the adjacent materials.

1.6.7. 2. Fabrication of periodic nanopatterns for PC

Many approaches have been reported to make nano-periodic structures for application of photonic crystals such as patterned silicon wafer[30], semiconductor clusters[31], InGaAs quantum well,[32] and block copolymer photonic crystals[33]. However these approaches have the limitation of large scale, process feasibility and low cost, and thus nano-periodic structures makes fabrication of photonic crystals complex and demanding. In order to fabricate periodic nanopatterns with easy process in this thesis, PRINT^{TM} method in Figure 1.14 has been investigated[34]. In particular, the PRINT method can be a powerful solution to these limitations, because it can make mono-disperse nanopatterns that cover large areas in an easy process.

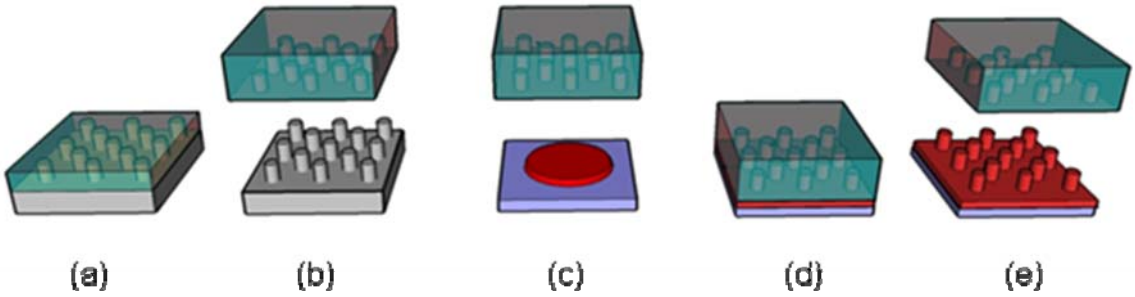

Figure 1.14. (a) The dimethacrylated-funtionalized PFPE was prepared and poured over a nanopatterned silicon master template (b) The nanopattened PFPE replica mold was generated by photochemically curing the poured PFPE. (c) Material desired for patterning is spincasted onto a cleaned substrate where (d) the PFPE mold is placed on top, and pressure and heat are applied. (e) The PFPE replica is peeled off the substrate to give highly ordered and regular nanopatterns.

1.6.7.3 Contrast of refractive index in adjacent materials for PC

Because the photonic effect strongly depends on a large contrast of refractive index between the two adjacent layers composing the nanostructure[35], the PC was designed to incorporate low index material into nanopatterned layer for the device application. Figure 1.15 shows the designed structure for OPV application where the 2-D PC topography is molded in the BHJ layer (P3HT:PCBM), a relatively high refractive index mixture (~2.1 at 550 nm) which in turn, is surrounded by nano-crystalline zinc oxide (*nc*-ZnO), a relatively low refractive index material[36] (~1.4 over whole wavelength range 400 nm – 800 nm). The resulting interdigitated morphology of the patterned P3HT:PCBM and *nc*-ZnO has sufficient optical contrast to exhibit PC behavior.

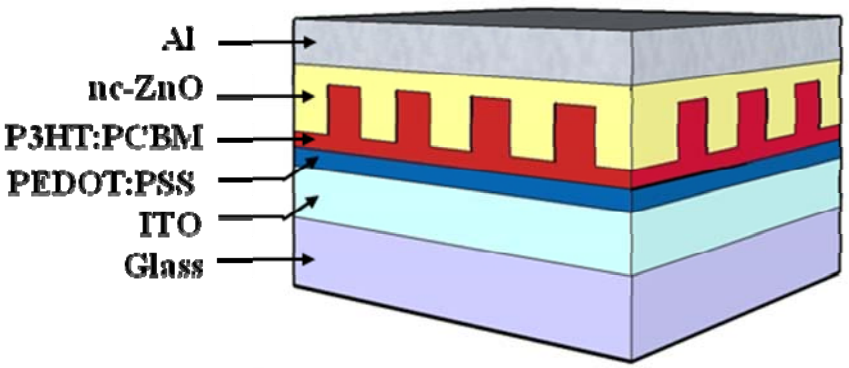

Figure 1.15. PC geometry for OPV. The 2-D photonic crystal topography molded in the bulk heterojunction (P3HT:PCBM) of relatively high refractive index (~2.1 at 550 nm) is embedded in nano-crystalline zinc oxide (*nc*-ZnO), a relatively low refractive index material (~1.4 at 550nm). The resulting interdigitated morphology of patterned P3HT:PCBM surrounded by *nc*-ZnO has sufficient optical contrast to exhibit photonic crystal behavior.

1.7 Electrical modeling for OPV

In order to model OPV, the metal-insulator-metal (MIM) model has been investigated in this thesis, assuming the blend of donor and acceptor materials as one semiconducting material. Here, the charge carriers undergo drift and diffusion in the photoactive layer where the space charge is affected by the electric field, which determines the carrier transport properties. The electrical loss of the photogenrated charge carriers follow a bimolecular recombination process with the Langevin recombination rate.[37] Also, the exciton generation rate is assumed to be homogeneous throughout the device.

1.7.1 Exciton dissociation probability

Mihailetchi et al.[38] investigated exciton dissociation at the interface between donor and acceptor does not directly produce the free charge carriers resulting in bound hole-electron pairs. Here, they described the process to generate the free charge carriers into two

steps: the holes and electrons at the interface between donor and acceptor are treated as the bound pairs, and subsequently the pairs are driven to be dissociated and transported into the electrodes via the internal electric field in the devices. Based on the Brauns' model,[39] the probability of electron-hole pair dissociation, namely the exciton dissociation probability (p), is given by

$$P\left(T, E, \mu_{e,h}, \varepsilon_r, a\right) = \frac{k_{diss}}{k_{diss} + k_f} \tag{1.3}$$

where T is temperature, E is field strength, μ is mobility of carriers, ε_r is the spatial average dielectric constant, a is the initial separation of the bound e-h pair at the interface, k_{diss} is the dissociation rate constant, k_f is the decay rate constant. Here, the k_{diss} is a field dependent constant given by Onsager's theory[40], and Braun[39] derived the constant as given below:

$$k_{diss}(E) = \frac{3R}{4\pi a^3} e^{-E_B/kT}\left[1 + b + \frac{b^2}{3} + \frac{b^3}{18} + \frac{b^4}{180} + ...\right] \tag{1.4}$$

where E_B is the electron-hole pair's binding energy, R is the recombination rate, and b = $q^3E/(8\pi\varepsilon_0\varepsilon_r^2T^2)$. Figure 1.16 shows a schematic of generation of the free charge carriers.[41]

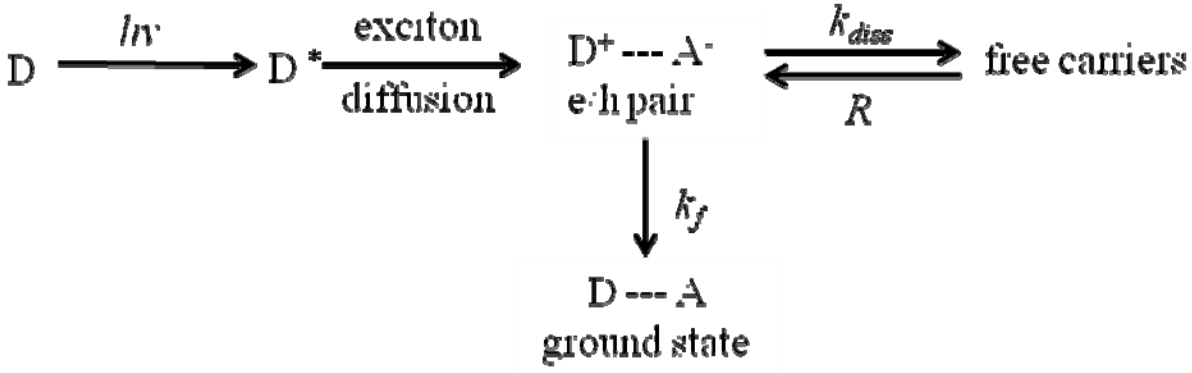

Figure 1.16. Schematic diagram for charge-carrier formation in donor (D) / acceptor (A) films where k_{diss} is a dissociation rate constant, k_f a decay rate and R is the recombination rate. The created exciton in donor diffuses to the interface between donor and acceptor, and the electron is transferred to the donor forming a bound hole-electron pair. The bound hole-electron pair undergoes generation of free charge carriers via the internal electric field or decays to the ground state. Even the dissociated free carriers possibly decay via recombination process.[41]

1.7.2 Experimental characterization for exciton dissociation probability

Mihailetchi et al.[38] show that the exciton dissociation probability can be experimentally determined. Here the photocurrent density (J_{ph}) is experimentally measured by subtracting the dark current density (J_D) from the illuminated current density (J_L). When all created excitons are extracted from devices under non-recombination conditions, the photocurrent becomes saturated.[7] Therefore, the saturated photocurrent density, J_{sat}, can be determined by application of extremely negative bias where recombination of created excitons cannot occur. Goodman and Rose[7] suggested the saturated photocurrent density is given by:

$$J_{ph} = qGL \tag{1.5}$$

with q the electron charge, G the generation rate of excitons, and L is the thickness of the photoactive layer. Because Goodman and Rose considered only drift of charge carriers, Sokel and Hughes[42] developed an analytical solution by including diffusion of carriers given by

$$J_{ph} = qGL\left[\frac{\exp(eV/kT)+1}{\exp(eV/kT)-1} - 2\frac{kT}{eV}\right] \tag{1.6}$$

This solution shows two regimes in J_{ph} vs. the applied effective voltage (V_0-V) properties as shown in Figure 1.17: In regime II where high negative bias is applied, the generated photocurrent is constant regardless of the effective voltage because no recombination process occurs. As the effective voltage is reduced in regime I, electrical loss processes, such as bimolecular recombination process become more meaningful and the photocurrent is linearly dependent on the applied effective voltage.

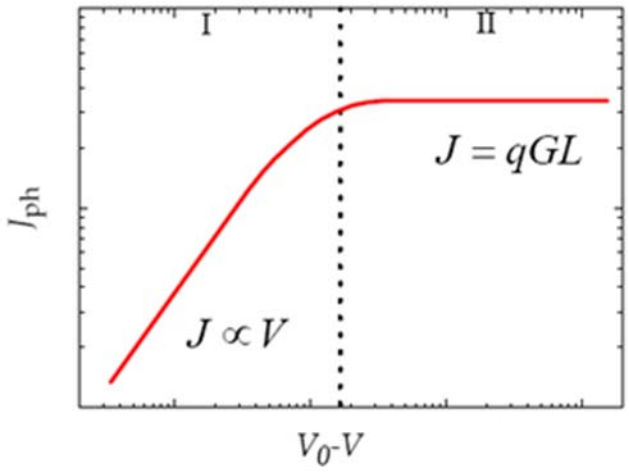

Figure 1.17. Schematic photocurrent Vs. the applied effective voltage (V_o-V) where V_0 is the voltage at J_{ph} = 0. Depending on the effective voltage, the J_{ph} is placed at either a linear regime (I) or a saturation regime (II).

Although the Sokel and Hughes solution well explained generation of free charge carriers in the device, the solution still deviates from the real phenomenon because they assume all dissociated excitons directly generate free charge carriers. However, all bound electron-hole pairs in the actual devices cannot dissociate into free charge carriers and only a certain fraction of maximum G (G_{max}) can form free carriers. Thus, Blom et al.[38] found a more realistic solution given by,

$$G(T, E) = G_{\max} P(T, E) \tag{1.7}$$

Consequently, the exciton dissociation probability (P) can be experimentally obtained by comparing the photocurrent at the desired voltage with the experimentally measured J_{sat}. For the MDMO-PPV(poly(2-methoxy-5-(3',7'-dimethyloctyloxy)-*p*-phenylene vinylene):PCBM device, only 60% of the bound hole-electron pairs dissociate into free carriers under short circuit conditions.

1.7.3 Bimolecular recombination process

In this thesis, the dissociated free carriers were assumed to experience bimolecular recombination process. For the recombination rate *R*, Koster et al.[41] proposed bimolecular recombination process given by

$$R = \gamma\left(np - n_{\text{int}}{}^{2}\right) \tag{1.8}$$

where n_{int} is the intrinsic carrier density of electron and holes given by $n_{int}=N_c\exp(-E_{gap}e/2qkT)$, and γ is the recombination strength. The bimolecular recombination process in OPV can be depicted in Figure 1.18 where the hole and electron are away from the electrodes at distance r_h and r_e respectively from the interface. When the carriers travel a certain distance within r_h and r_e, the faster charge carrier reaches the interface first and must wait for slower charge carrier's arrival. Therefore, the slow charge carriers determine the recombination process in OPV, and the recombination strength is given by, [43]

$$\gamma = \frac{q}{<\varepsilon>}\min\left(\mu_e, \mu_h\right) \tag{1.9}$$

where $<\varepsilon>$ is the spatially averaged dielectric constant, and μ_e and μ_h are electron and hole mobility, respectively.

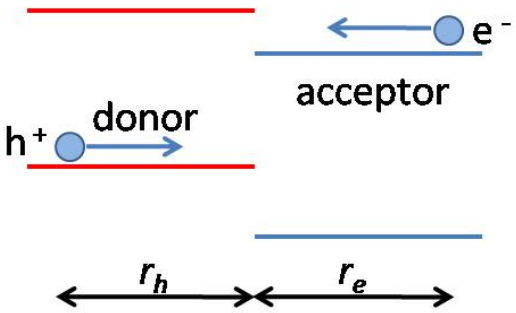

Figure 1.18. Schematic of bimolecular recombination process. The charge carriers possibly travel a certain distance and undergoes bimolecular recombination process.

Here, the bimolecular recombination process is governed by two crucial parameters: First, the higher number of carriers possibly undergoes higher bimolecular recombination processes because more carriers increase the chance to meet each counter carrier (hole or electron). From this standpoint, the working theory for OPV has been studied at the extremely low light intensity in order to cut the possible side effects via recombination processes.[44] In this thesis, the number of generated carriers was controlled by the illuminated light intensity and the bimolecular recombination process was analyzed by varying the light intensity. Second, the strong electric field induces larger extraction of the free charge carriers to the electrodes such that they experience less bimolecular recombination process. These two parameters (carrier density, electric field) play important roles to characterize the bimolecular process.

1.8 Scope of thesis

Consequently, two length scales, the absorption depth and carrier transport length, work against one another during the photovoltaic process. This competition is prevalent over the entire solar spectrum but increasingly so near a semiconductor's band edge where absorption is weak. In order to solve the intrinsic problem, a 2-D photonic crystal geometry was demonstrated in Chapter 1 and 2, showing the enhanced performance of photonic crystal organic photovoltaic cells (PC cells) relative to conventional planar cells. The PC geometry was developed by patterning an organic photoactive bulk heterojunction blend of Poly(3-(2-methyl-2-hexylcarboxylate)thiophene-co-thiophene) and PCBM or P3HT and PCBM via PRINT^{TM}, a method that lends itself to large area fabrication of nanostructures. The large scale of PC cells fabrication technique with facile process was deeply investigated, including

the PC fabrication flexibility of PRINT for the various materials and device architectures. Also, the critical parameters for PC cells that were studied are correlated to device performance. The unique absorption enhancement via the excitation of resonant modes in the PC cells was explored to harness the IR region of incident light and successfully target desired regions of the solar spectrum for absorption enhancements. The associated performance in PC cells with absorption enhancements was analyzed.

For the PC behavior, the large contrast of refractive index of nanopatternes in the adjacent material is essential. When incorporating the layer for the PC behavior, the additional layer would affect the device performance electrically and optically as optical spacer or carrier transporting layer. Therefore, characterizations for electrical performance variation and working theory by introducing the layer should be preceded to optimize the PC cells. In fact, the various additional layers have been incorporated to improve the device performance.[45-47]

In Chapter 3, the UV-sensitive amorphous and crystalline titanium oxides (TiO_x and TiO_2) were used as electron transport layers (ETL). Here the resistivity changes of the ETL by UV illumination was correlated with bimolecular recombination process via electro-optical modeling and light intensity experiments.

1.9 **References**

(1). Green, M. A.; Emery, K.; Hishikawa, Y.; Warta, W. *Prog. Photovolt: Res. Appl.* **2009,** 17, 85.

(2). Moliton, A.; Nunzi, J.-M. *Polym. Int.* **2006,** 55, 583.

(3). Coakley, K. M.; McGehee, M. D. *Chem. Mater.* **2004,** 16, 4533.

(4). Halls, J. J. M.; Walsh, C. A.; Greenham, N. C.; Marseglia, E. A.; Friend, R. H.; Moratti, S. C.; Holmes, A. B. *Nature* **1995,** 376, 498.

(5). Yu, G.; Gao, J.; Hummelen, J. C.; Wudl, F.; Heeger, A. J. *Science* **1995,** 270, 1789.

(6). Zerza, G.; Brabec, C. J.; Cerullo, G.; De Silvestri, S.; Sariciftci, N. S. *Synth. Met.* **2001,** 119, 637.

(7). Goodman, A. M.; Rose, A. *J. Appl. Phys.* **1971,** 42, 2823.

(8). Chen, H.-Y.; Hou, J.; Zhang, S.; Liang, Y.; Yang, G.; Yang, Y.; Yu, L.; Wu, Y.; Li, G. *Nature Photon.* **2009,** 3, 649.

(9). Li, G.; Shrotriya, V.; Yao, Y.; Yang, Y. *J. Appl. Phys.* **2005,** 98, 043704.

(10). Roman, L. S.; Inganäs, O.; Granlund, T.; Nyberg, T.; Svensson, M.; Andersson, M. R.; Hummelen, J. C. *Adv. Mater.* **2000,** 12, 189.

(11). Peumans, P.; Bulovic, V.; Forrest, S. R. *Appl. Phys. Lett.* **2000,** 76, 2650.

(12). Niggemann, M.; Glatthaar, M.; Gombert, A.; Hinsch, A.; Wittwer, V. *Thin Solid Films* **2004,** 451-452, 619.

(13). Niggemann, M.; Glatthaar, M.; Lewer, P.; Müller, C.; Wagner, J.; Gombert, A. *Thin Solid Films* **2006,** 511-512, 628.

(14). Rim, S.-B.; Zhao, S.; Scully, S. R.; McGehee, M. D.; Peumans, P. *Appl. Phys. Lett.* **2007,** 91, 243501.

(15). Kim, J. Y.; Kim, S. H.; Lee, H. H.; Lee, K.; Ma, W.; Gong, X.; Heeger, A. J. *Adv. Mater.* **2006,** 18, 572.

(16). Niggemann, M.; Riede, M.; Gombert, A.; Leo, K. *Phys. Stat. Sol. A* **2008,** 205, 2862.

(17). Park, S. H.; Roy, A.; Beaupre, S.; Cho, S.; Coates, N.; Moon, J. S.; Moses, D.; Leclerc, M.; Lee, K.; Heeger, A. J. *Nature Photon.* **2009,** 3, 297.

(18). Heine, C.; Morf, R. H. *Appl. Opt.* **1995,** 34, 2476.

(19). Delley, B.; Kiess, H. *Sol. Eng. Mater. Sol. Cells* **1994,** 33, 1.

(20). Tvingstedt, K.; Andersson, V.; Zhang, F.; Inganas, O. *Appl. Phys. Lett.* **2007,** 91, 123514.

(21). Lee, J. H.; Park, J. H.; Kim, J. S.; Lee, D. Y.; Cho, K. *Org. Electron.* **2009,** 10, 416.

(22). Pillai, S.; Catchpole, K. R.; Trupke, T.; Green, M. A. *J. Appl. Phys.* **2007,** 101, 093105.

(23). Tvingstedt, K.; Persson, N.-K.; Inganas, O.; Rahachou, A.; Zozoulenko, I. V. *Appl. Phys. Lett.* **2007,** 91, 113514.

(24). Morfa, A. J.; Rowlen, K. L.; Reilly, T. H.; Iii; Romero, M. J.; van de Lagemaat, J. *Appl. Phys. Lett.* **2008,** 92, 013504.

(25). Duche, D.; Escoubas, L.; Simon, J.-J.; Torchio, P.; Vervisch, W.; Flory, F. *Appl. Phys. Lett.* **2008,** 92, 193310.

(26). Cocoyer, C.; Rocha, L.; Sicot, L.; Geffroy, B.; de Bettignies, R.; Sentein, C.; Fiorini-Debuisschert, C.; Raimond, P. *Appl. Phys. Lett.* **2006,** 88, 133108.

(27). Na, S.-I.; Kim, S.-S.; Kwon, S.-S.; Jo, J.; Kim, J.; Lee, T.; Kim, D.-Y. *Appl. Phys. Lett.* **2007,** 91, 173509.

(28). Kim, M.-S.; Kim, J.-S.; Cho, J. C.; Shtein, M.; Guo, L. J.; Kim, J. *Appl. Phys. Lett.* **2007,** 90, 123113.

(29). Chow, E.; Lin, S. Y.; Johnson, S. G.; Villeneuve, P. R.; Joannopoulos, J. D.; Wendt, J. R.; Vawter, G. A.; Zubrzycki, W.; Hou, H.; Alleman, A. *Nature* **2000,** 407, 983.

(30). Lin, S. Y.; Fleming, J. G.; Hetherington, D. L.; Smith, B. K.; Biswas, R.; Ho, K. M.; Sigalas, M. M.; Zubrzycki, W.; Kurtz, S. R.; Bur, J. *Nature* **1998,** 394, 251.

(31). Alivisatos, P. *Nat Biotech* **2004,** 22, 47.

(32). Ogawa, S.; Imada, M.; Yoshimoto, S.; Okano, M.; Noda, S. *Science* **2004,** 305, 227.

(33). Kang, Y.; Walish, J. J.; Gorishnyy, T.; Thomas, E. L. *Nature Mater.* **2007,** 6, 957.

(34). Rolland, J. P.; Maynor, B. W.; Euliss, L. E.; Exner, A. E.; Denison, G. M.; DeSimone, J. M. *J. Am. Chem. Soc.* **2005,** 127, 10096.

(35). Joannopoulos, J. D.; Meade, R. D.; Winn, J. N., *Photonic crystals: Molding the flow light* Princeton university press: New Jersey, 1995.

(36). Tumbleston, J. R.; Ko, D.-H.; Samulski, E. T.; Lopez, R. *Appl. Phys. Lett.* **2009,** 94, 043305.

(37). Langevin, P. *Ann. Chim. Phys.* **1903,** 28, 433.

(38). Mihailetchi, V. D.; Koster, L. J. A.; Hummelen, J. C.; Blom, P. W. M. *Phys. Rev. Lett.* **2004,** 93, 216601.

(39). Braun, C. L. *J. Chem. Phys* **1984,** 80, 4157.

(40). Onsager, L. *J. Phys. Chem.* **1934,** 2, 599.

(41). Koster, L. J. A.; Smits, E. C. P.; Mihailetchi, V. D.; Blom, P. W. M. *Phys. Rev. B* **2005,** 72, 085205.

(42). Sokel, R.; Hughes, R. C. *J. Appl. Phys.* **1982,** 53, 7414.

(43). Koster, L. J. A.; Mihailetchi, V. D.; Blom, P. W. M. *Appl. Phys. Lett.* **2006,** 88, 052104.

(44). Marsh, R. A.; McNeill, C. R.; Abrusci, A.; Campbell, A. R.; Friend, R. H. *Nano Lett.* **2008,** 8, 1393.

(45). Chen, L.-M.; Hong, Z.; Li, G.; Yang, Y. *Adv. Mater.* **2009,** 21, 1434.

(46). White, M. S.; Olson, D. C.; Shaheen, S. E.; Kopidakis, N.; Ginley, D. S. *Appl. Phys. Lett.* **2006,** 89, 143517.

(47). Waldauf, C.; Morana, M.; Denk, P.; Schilinsky, P.; Coakley, K.; Choulis, S. A.; Brabec, C. J. *Appl. Phys. Lett.* **2006,** 89, 233517.

Chapter II

PHOTONIC CRYSTAL GEOMETRY FOR ORGANIC SOLAR CELLS

2.1 Introduction

As summarized in Chapter I, the light trapping schemes based on ray optics have provided enhancement in optical absorption, e.g. collector mirrors[1], microprism substrates[2], and V-folded configurations[3], but in these schemes absorption enhancement was not tailored to a desired spectral range. Methods based on wave optics have shown greater promise, and both diffraction gratings[4,5,6] and photonic crystal (PC) designs have been investigated. In particular, theoretical considerations of PC geometries suggest efficiency improvements would be anticipated[7,8,9] for organic solar cells similar to theoretical work on inorganic devices[10,11]. In spite of this theoretical promise, there has been little progress in experimentally demonstrating PC effects in organic solar cells. While there has been success in nanopatterning the photoactive layer, the primary intention has been to provide an undulating surface for evaporating a metal diffraction grating[4,12,13] or to make an ordered BHJ device[14]. Herein, I explore a two-dimensional periodic PC organic solar cell made from highly ordered arrays of columnar features. The PC is readily fabricated via Pattern Replication In Non-wetting Templates (PRINT^{TM})[15], a materials-agnostic process that lends itself to large area replication of nanoscale features. As a proof of concept we use the BHJ blend, poly(3-(2-methyl-2-hexylcarboxylate) thiophene-co-thiophene)[16] (TDPTD): [6,6]-phenyl-C_{61}-butyric acid methyl ester (PCBM), but the fabrication method could be applied to any photoactive polymer processed from solution.

I demonstrate the fabrication of bulk heterojunction organic solar cells with photonic crystal (PC) geometries using the materials-agnostic PRINT^{TM} process where highly ordered arrays of nanoscale features can be made in a single step. The PC cells successfully target desired regions of the solar spectrum for averaged 3-fold absorption enhancements in part through multiple excitation resonances. I show efficiency improvements of ~70% that result not

only from improved absorption, but also from intriguing electrical improvements where both the fill factor (*FF*) and open circuit voltage (V_{oc}) are enhanced ~10%.

2.2 Experimental Section

2.2.1 Nanocrystalline ZnO (*nc*-ZnO) synthesis

The nanocrystalline ZnO was prepared according to the method by Beek et al[17]. The reaction was carried out in a two-neck flask with a condenser and dropping funnel. Zinc acetate dihydrate (Aldrich >98%, 2.95g) was dissolved in methanol (125 ml) at 60°C for 1hr; a Potassium hydroxide solution (Fisher 86.6%, 1.48 g) in methanol (65 ml) was added to the Zinc acetate dihydrate solution dropwise over 15 min at 60°C under vigorous stirring conditions for 130 min. After completion of the reaction, the heater was removed and the solution was cooled to room temperature over 2 hrs. The solution was centrifuged and the resulting solid was washed with methanol; this was repeated three times. The resulting nanocrystalline zinc oxide (nc-ZnO) was analyzed by a JEOL 100CX II transmission electron microscopy, and the mean diameter of the nc-ZnO particles was about 5nm.

2.2.2. TDPTD (Thermally Deproctectable Poly Thiophene Derivatives) synthesis

TDPTD, alternating Poly(3-(2-methyl-2-hexylcarboxylate)thiophene-co-thiophene), was prepared according to a literature procedure[18]. The synthesis scheme is shown in Scheme 2.1. Thiophene (≥99%, Aldrich)**,** butyllithium solution (2.5M in hexane, Aldrich), trimethyltin chloride solution (1.0M in tetrahydrofuran, Aldrich), 3-thiophenecarboxylic acid (99%, Aldrich), bromium (100%, EM Science), 2-methyl-2-hexanol (97%, Aldrich), 2-chloro-3,5-dinitropyridine (99%, Aldrich), tetrakis(triphenylphosphine)palladium(0) (99%, Aldrich), glacial

acetic acid (100%, Fisher), sodium sulfite (98.4%, Fisher), anhydrous magnesium sulfate (99%, Fisher), calcium hydride (≥97%, Fluka), sodium bicarbonate (100%, Mallinckrodt), anhydrous sodium sulfate (100%, Mallinckrodt), silica gel (230-400 Mesh, Fisher), ethanol (Pharmco-Aaper), ethyl ether (Fisher), petroleum ether (Fisher), ethyl acetate (Fisher), hexane (Fisher), methanol (Fisher), and tetrahydrofuran (Fisher) were used as received without further purification. *N*,*N*,*N*′,*N*′-Tetramethylethylenediamine (99%, Aldrich), pyridine (Fisher), N,N-dimethyl formamide (Aldrich), and toluene (Fisher) were stirred overnight over CaH_2 and filtered prior to use. All reactions were performed under dry nitrogen unless otherwise noted.

For characterization of the synthesized polymers, gel permeation chromatography (GPC) was performed in THF at 40 ˚C using a Waters chromatograph equipped with three Waters columns (Waters Styragel HR2, HR4, and HR5), a Wyatt Optilab DSP interferometric refractometer and a Wyatt Dawn ESO detector, and calibrated with polystyrene standards. M_n of the prepared was 19.8k and polydispersity index was 2.09.

2.2.3 PFPE (perfluoropolyether) mold fabrication

A liquid 1 kDa PFPE-DMA (α, Ω-functionalized dimethacrylate) precursor solution containing 1 wt % 2,2-diethoxyacetophenone (DEAP) was fabricated by the previously reported method.[15] The prepared PFPE was poured over a nanopatterned silicon master template or a piranha cleaned flat silicon wafer. The liquid precursor was then cross-linked using UV photoirradiation (λ_{max} = 365 nm) for 3 min. under a constant nitrogen purge to provide an elastomeric mold of the master template. The fully cured PFPE-DMA elastomeric mold or flat membrane was then released from the nanostructured or flat silicon substrate.

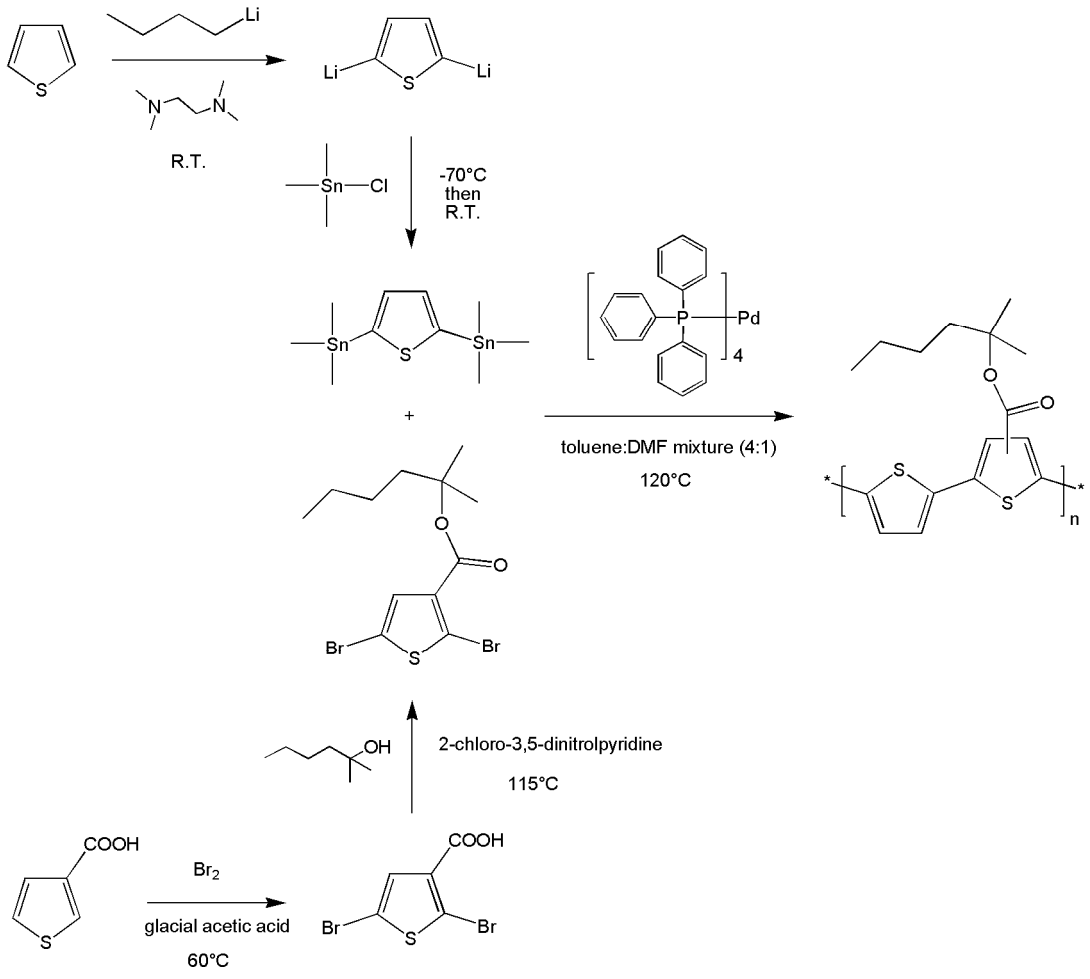

Scheme 2.1. Synthesis of Alternating Poly(3-(2-methyl-2-hexylcarboxylate)thiophene-co-thiophene)

2.2.4 Device fabrication

The device fabrication procedure using the materials described above is shown schematically in Figure 2.1. Both cells employ the transparent conductor ITO (150 nm) on glass with an 30 nm over layer of Poly(3,4-ethylenedioxythiophene):Poly(styrenesulfonate) (PEDOT:PSS), a widely used substrate. ITO-coated glass was cleaned with acetone, isopropyl alcohol and distilled water for 10min each, and then dried overnight in an oven (150 ˚C). The cleaned substrate was treated with UV Ozone for 20min (UVO Cleaner 42, Jelight Company Inc.). The PEDOT:PSS (Baytron PH 500) was filtered with a 0.45μm PVDF filter and then 40 nm of PEDOT:PSS was spincoated onto the substrate and annealed for 10 min at 140°C. The annealed sample was moved into an inert gas (purified nitrogen) glove box. In order to prepare the flash layer, a solution containing TDPTD (10 mg mL^{-1}) and PCBM (8 mg mL^{-1}) in chlorobenzene was filtered with a 0.45μm PTFE filter and spincoated onto the PEDOT:PSS-coated substrate to form a ~40 nm "flash layer." The procedure for controlling the flash layer thickness with the patterned bulk heterojunction was carried out in two steps: First, a TDPTD:PCBM solution was spin-coated with nominal thickness control and thermally cured (200°C for 15min). The thermal curing step deprotects the alternating poly(3-(2-methyl-2-hexylcarboxylate)thiophene-co-thiophene) to yield alternating poly(3-carboxylatethiophene-co-thiophene) as shown in scheme 2.2. Second, a more concentrated solution containing TDPTD (15mg mL^{-1}) and PCBM(12mg mL^{-1}) in chlorobenzene was spincoated on the cured flash layer. The new layer was patterned by contacting a perfluoropolyether (PFPE) mold under pressure at 200°C for 15 min, a variation of the PRINT methodology.[15] The planar cell was simultaneously fabricated by "embossing" the layer with a flat PFPE "mold." The patterning step is followed by spincoating various concentrations of *nc*-ZnO in methanol to get the desired thickness of *nc*-ZnO

film. Finally the device was transferred into a vacuum chamber (2×10^{-6} torr) and 110 nm Al was deposited on defined cell areas (12 mm^2). The device structures were characterized by SEM (Hitachi S-4700). Thickness of layers was monitored by profilometer (Tencor Alpha step-200) and the SEM.

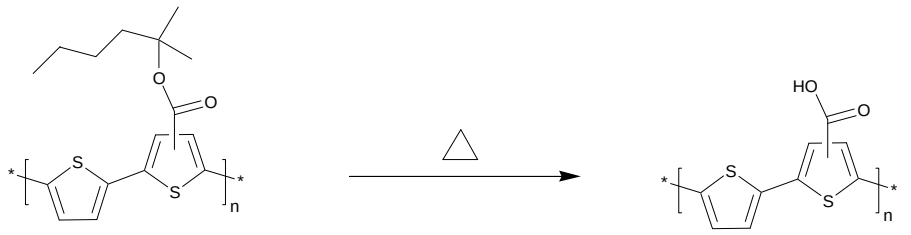

Poly(3-(2-methyl-2-hexylcarboxylate)thiophene-co-thiophene Poly(3-carboxylatethiophene-co-thiophene)

Scheme 2.2. Deprotection process of TDPTD. The alky group of the TDPTD becomes deprotected via thermal annealing step at above 200°C.

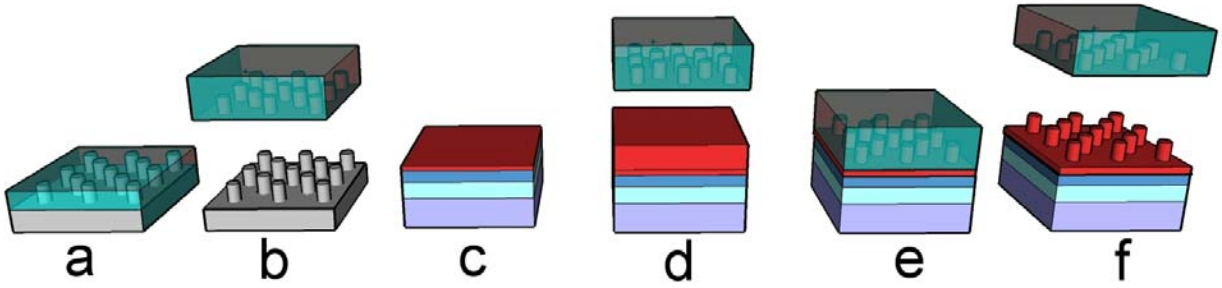

Figure 2.1. Schematic of the PRINT method (planar cells are made with a featureless mold). (a) A dimethacrylated-funtionalized PFPE was prepared and poured over a nanopatterned silicon master template; (b) The nanopattened PFPE replica mold was generated by photochemically curing the PFPE. (c) A TDPTD:PCBM solution was spin-coated on the PEDOT:PSS-coated substrate and thermally cured at 200°C for 15min to prepare the flash layer. (d) A more concentrated solution containing TDPTD and PCBM was spincoated on the cured flash layer. (e) The new layer was patterned with the perfluoropolyether (PFPE) mold under pressure at 200°C for 15 min. (f) The PFPE replica was peeled off the substrate to give highly ordered and regular nanopatterns over the specified substrate area.

2.2.5 Device measurement

All efficiency measurements were performed in inert gas (purified nitrogen) filled glove box at room temperature. Current-Voltage performance was achieved by Keithley 2400 source meter with exposure to 100 mW/cm^2 light, made from Oriel-Newport 300 W solar simulator. The solar spectrum was modulated by AM 1.5G filter without an additional filter. The intensity of the solar simulator was measured by a standard silicon solar cell calibrated by the National Renewable Energy Laboratory.

Polarized angular reflection and IPCE measurements of patterned and planar cells were conducted in air using a 75W HS-190 monochromater by J.A. Woollam Co., Inc and an optical chopper with lock-in amplifier. The angular reflection and IPCE were measured in both p- and s-polarizations with p-polarization oriented along the 400 nm periodicity of the hexagonal photonic crystal (s-polarization rotated 90º). I confirmed that there was no device degradation in air over the maximum measurement time of ~3 hrs.

2.3 Results and Discussion

2.3.1 Fabrication of photonic crystal geometry for organic solar cells

The PC structure is formed in a single PRINT step by nanopatterning the photoactive BHJ blend, a relatively high refractive index material, into a hexagonal array of posts with 400 nm periodicity. The BHJ then interfaces with a transparent, low refractive index form of nanocrystalline zinc oxide (*nc*-ZnO), which provides enough optical contrast to enable PC behavior.

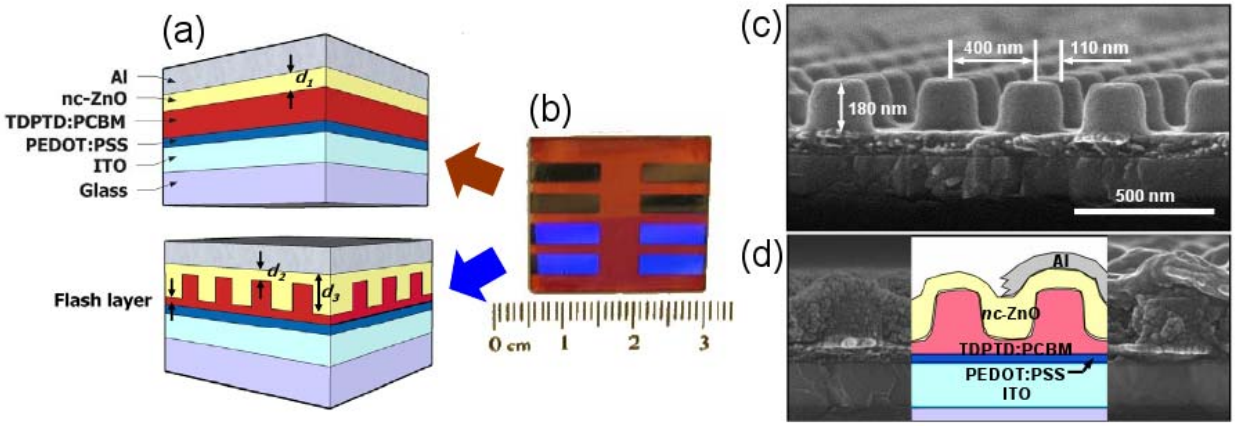

Figure 2.2. PC and planar geometries for organic solar cells. (a) Schematic of planar control (top) and PC (bottom) cells. (b) Planar cells (brown) and iridescent PC cells (blue) on the same device substrate. The angular dependent color from the PC cells derives from diffraction at large incident angles. (c) Scanning electron micrograph of hexagonal array of BHJ columns prior to back-filling with *nc*-ZnO. (d) Cross section of PC cell showing the hierarchical arrangement of components (left without Al overcoat), right (from the top): Al / *nc*-ZnO / patterned TDPTD:PCBM / Flash-layer TDPTD:PCBM / PEDOT:PSS / ITO / Glass

.

Figure 2.2 shows a schematic (a), photograph (b), and scanning electron micrograph (SEM) cross section (c, d) of PC solar cells. PC and planar cells are fabricated on the same device substrate and can be easily distinguished due to the bright iridescence of the PC device. Simultaneously fabricating PC and planar cells on the same substrate ensures that each contains an equivalent volume of photoactive material and undergoes identical fabrication steps and thermal history. In the PC cell, the photoactive TDPTD:PCBM constitutes both the planar flash layer (40 nm) and the hexagonal array of columnar features that are 180 nm in height (see Figure 2.2c). The TDPTD:PCBM mixture becomes insoluble after thermally curing[16] which enables control of the flash layer thickness in a spin-coating step prior to forming the PC geometry. A thin flash layer is critical in two respects: 1) it prevents direct contact between the *nc*-ZnO and the poly(3,4-ethylenedioxythiophene): poly(styrenesulfonate) (PEDOT:PSS) interface, and 2) it determkines height of the TDPTD:PCBM columns–the aspect ratio for equivalent flat-cell PV-active material contents–which, in turn, increases the photonic activity.

The *nc*-ZnO has been used in photovoltaic cells as an optical spacer[19], an electron transport layer[20], a high electron mobility film[21], and an improved electrical contact for metal cathodes[22]. Herein the *nc*-ZnO serves as a refractive index contrast matrix in the PC cell and a "spacer layer" in the planar cell; it is formed by spin-coating a dispersion of freshly synthesized *nc*-ZnO[17] (~5 nm diameter particles) in methanol on both the embossed and planar photoactive strata, respectively (see Supplementary Information for fabrication details). A cross section of the latter structure is shown in Figure 2.1d. Although an IR-VIS-transparent material, the *nc*-ZnO layer can affect the absorption characteristics of the cell via interference effects[19], so PC and planar cells with various *nc*-ZnO thicknesses were fabricated. Thus, in addition to controlling the thickness of the *nc*-ZnO layer in the planar cell (d_1), the thicknesses of the *nc*-ZnO film between

and above the BHJ columns, d_2 and d_3 respectively, were varied (see Figure 2.2a). These values are given for five different sets of PC and planar cells fabricated on different device substrates in Table 2.1.

Table 2.1. Thicknesses of *nc*-ZnO for PC and planar cells fabricated on five different device substrates

	nc-ZnO thickness (nm)	
device number	planar (d_1)	photonic crystal (d_2, d_3)
1	50	10, 30
2	90	40, 100
3	130	60, 150
4	200	70, 220
5	280	120, 300

2.3.2 Optical Performances and IPCE (incident-photon-to-current conversion efficiency) of Planar and PC cells

Figure 2.3a shows the significant refractive index contrast of the optical properties of TDPTD:PCBM and *nc*-ZnO measured via spectroscopic ellipsometry. When combined with the 400 nm hexagonal periodicity of the PC, optimal conditions are met for band edge absorption enhancements in TDPTD:PCBM. Figure 2.3b shows the s-polarized zeroth order reflection measured at normal incidence for the PC and planar cells for device No. 2. (The p-polarization is nearly identical at normal incidence and is not shown.) Due to negligible transmission and scattering, (the iridescence effects are only appreciable at large incidence angles), the reflection

(R) yields an approximation to the absorption (A) using, A = 100 – R. Due to the ~90 nm active layer thickness of the planar cell, there is strong absorption in the visible range where the extinction coefficient of TDPTD:PCBM is high. This corresponds to essentially equivalent absorption in this wavelength range for PC and planar cells. However, for wavelengths longer than 600 nm, there is much stronger absorption in the PC cell as evidenced by the reduced reflection (Fig. 2.3b). Specifically, the absorption is enhanced 3.5 times for the PC cell over the planar one for $\lambda = 660$ nm.

Also shown in Figure 2.3b is the incident-photon-to-current conversion efficiency (IPCE) for the PC and planar cells. There is an enhancement for wavelengths where the PC cell is absorbing more strongly, but there is also an enhancement where they appear to have similar absorption in the visible range. A first step towards reconciling this effect requires a more precise determination of the absorption. The above mentioned approximation of A = 100 – R is a measure of the total absorption where losses in all internal layers are included. Even though PC and planar cells are fabricated on the same substrate and have equivalent volumes of all internal materials, the PC structure alters the optical profile in each internal layer due to its modulated thickness relative to the planar photoactive layer. This will cause changes in the optical field in layers that also absorb light but do not produce photocurrent, such as the indium tin oxide anode (ITO) and PEDOT:PSS. Thus, simply comparing the measured reflection only offers a first approximation to the photoactive absorption. Losses may be individually quantified by fitting a solution to Maxwell's equations to the measured reflection data. Once this is achieved, absorption in each layer is determined by calculating the change in the Poynting vector from interface to interface as is frequently done for planar devices[23].

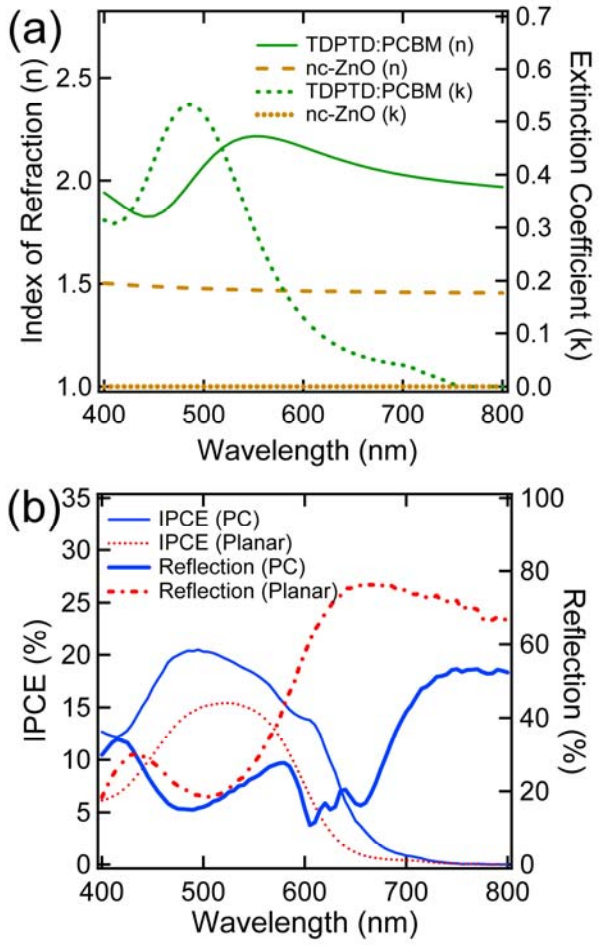

Figure 2.3. (a) Measured optical properties of the two materials that give the PC cell its high index of refraction contrast: the photoactive BHJ material, TDPTD:PCBM, and the transparent conductive oxide, *nc*-ZnO. (b) Zeroth order reflection and IPCE of PC and planar cells for s-polarized light at normal incidence for device No. 2.

2.3.3 Optical simulation for Planar and PC cells

I construct an optical model using scattering matrix theory[24] which is a general form of the transfer matrix method commonly used to model planar organic solar cells[19,23]. The complex dielectric functions of the cell materials (TDPTD:PCBM and *nc*-ZnO shown in Figure 2.3a) are used as input in the model and were measured using spectroscopic ellipsometry. The physical dimensions of the device are then varied over a range close to measured SEM values until an appropriate fit with the experimental data is obtained. These results are given in Figure 2.4a for the PC and planar cells for device No. 3. Good agreement is obtained between the theory and experiment for both polarizations at normal incidence. The model is then used to calculate absorption in the TDPTD:PCBM blend that will yield photocurrent in the external circuit. Blend absorption is plotted for both PC and planar cells in Figure 2.4b for s-polarization. This is a different device with different *nc*-ZnO thicknesses from that presented in Figure 2.3b, but the tendency of enhanced absorption and IPCE is qualitatively identical. There is still essentially equivalent photoactive absorption in the visible range with an enhancement towards the band edge. Specifically, a 4.8-fold absorption enhancement is achieved at $\lambda = 630$ nm for the PC cell relative to the planar one. This contributes to an average tripling of absorption near the band edge ($580 \leq \lambda \leq 750$).

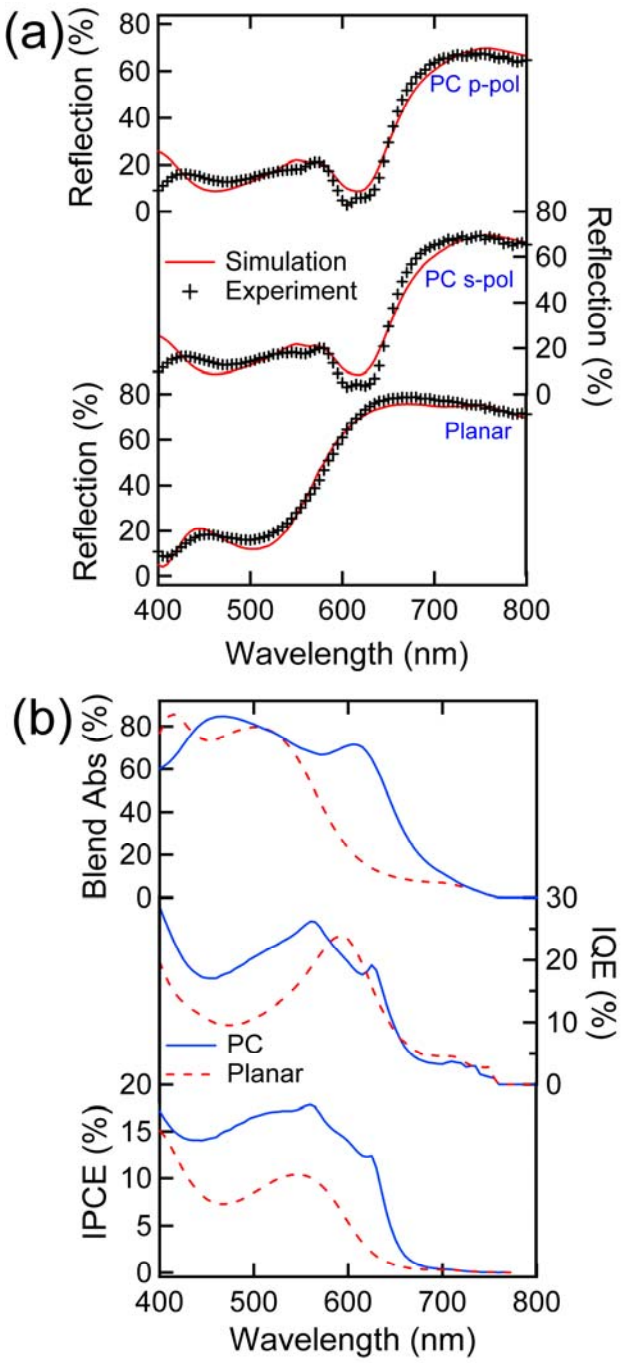

Figure 2.4. (a) Experimental and simulated zeroth order reflection for PC and planar cells for device No. 3 at normal incidence in both p- and s-polarization. The planar cell is equivalent in both polarizations. (b) Calculated TDPTD:PCBM absorption, IQE, and IPCE under s-polarized illumination.

Applying the simulation method to our devices did yield an accurate measure of photoactive absorption, but it did not explain the enhanced IPCE in the visible range where absorption is essentially equivalent between PC and planar cells. By calculating absorption (ABS) in TDPTD:PCBM and measuring IPCE, we can calculate the internal quantum efficiency (IQE) by, IPCE(λ) = IQE(λ)·ABS(λ). The IQE is a measure of the electrical processes in the cells at short circuit and is given for PC and planar device No. 3 in Figure 2.4b. Electrical processes include exciton dissociation at the BHJ donor/acceptor interface, drift and diffusion of free charge carriers through the blend, and carrier collection at the electrodes. As shown in Figure 2.4b, the IQE is enhanced in the visible spectral range, which indicates an inherent electrical enhancement for the PC cell.

2.3.4 Device performance for Planar and PC cells

In order to further investigate the electrical properties, device performance was evaluated in an inert atmosphere (purified nitrogen) under standard AM 1.5 testing conditions. The mean values of the short circuit current (J_{sc}), open circuit voltage (V_{oc}), fill factor (*FF*), and efficiency are summarized in Figure 2.5 where comparisons are made between PC and planar cells fabricated on the same substrate according to Table 2.1. I observe an average enhancement over all devices (~20 cells) of 10% for V_{oc} and 9% for *FF* for the PC devices. On the other hand, the J_{sc} shows more variable enhancements due to changes in optical absorption that result from optical interference. Overall, there is an average 68% efficiency enhancement for PC cells. We are currently investigating the improvement of the IQE, V_{oc}, and *FF* that are caused by the PC structure. It is possible that the PC generates a more favorable carrier creation profile in the

device that results in shorter transport paths for electrons and holes out of the BHJ blend. This may be facilitated by a 45% larger interface area between TDPTD:PCBM and *nc*-ZnO for the PC cells. The PC structure may also alter the static internal electric field in the photoactive region that could change the field-dependent dissociation of excitons at the TDPTD donor and PCBM acceptor interfaces[25].

2.3.5 Excitation of resonant modes for PC cells

Thus far I have described PC performance enhancements under normal light incidence. For non-normal illumination, resonant mode splitting occurs and generates absorption enhancements that exhibit a rich photonic behavior. This is demonstrated in Figure 2.6a-d for PC device No. 3 where the differences between p- and s-polarization can now be resolved in both reflection and IPCE measurements from 12º to 40º. Under normal incidence, resonant mode degeneracy masks the actual number of modes excited in the PC geometry as indicated in the reflection data of Figure 2.3b and 4a. On the other hand, under non-normal conditions, three modes can be resolved in p-polarization with at least two modes in s-polarization near the band edge of TDPTD:PCBM. Enhancements in both polarizations are possible, because the PC geometry is periodic in both lateral dimensions. Arrows track the dispersion of the stronger modes along with the resulting IPCE enhancement. The spectral location of the band edge of TDPTD:PCBM is also apparent near λ = 750 nm, because the resonant modes as shown in reflection retain their shape even after they have red-shifted past the wavelength where TDPTD:PCBM becomes transparent and produces no photocurrent. These long wavelength excitations are possible because other strata in

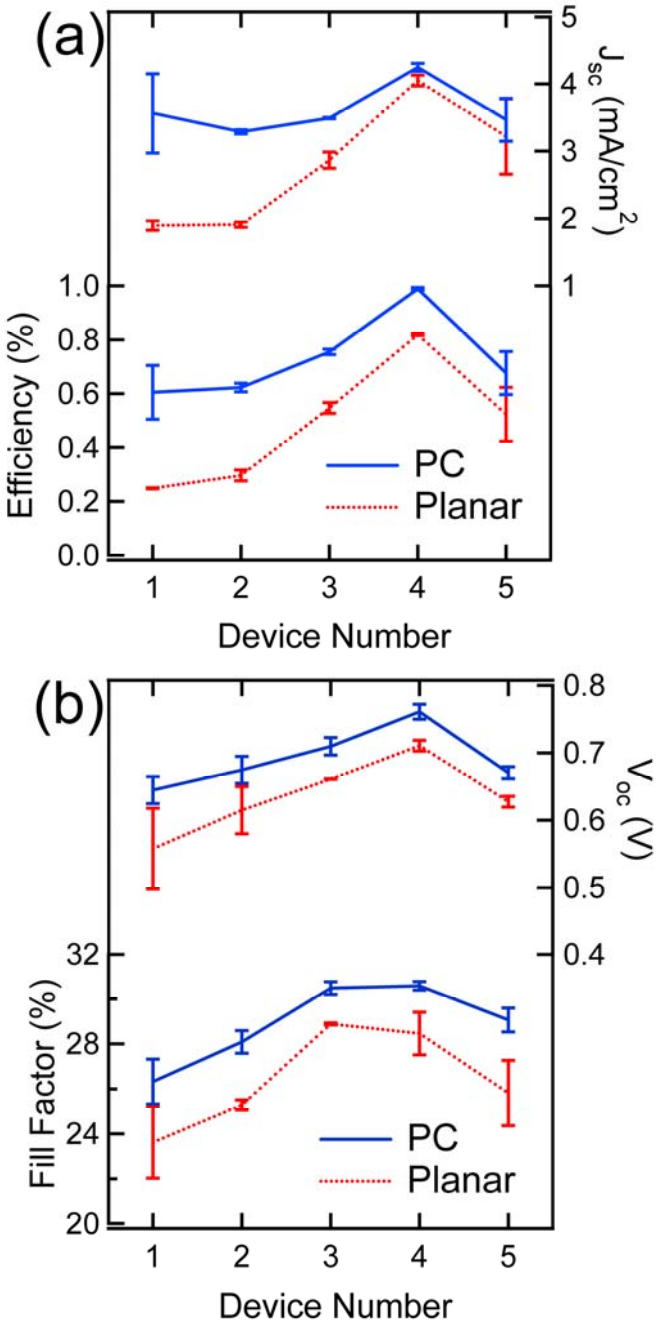

Figure 2.5. (a) Short circuit current (J_{sc}) and efficiency for PC and planar cells where comparisons are made between cells fabricated on the same device substrate. (b) The corresponding values of open circuit voltage (V_{oc}) and fill factor (FF). The mean values and error bars are an average over four cells per device.

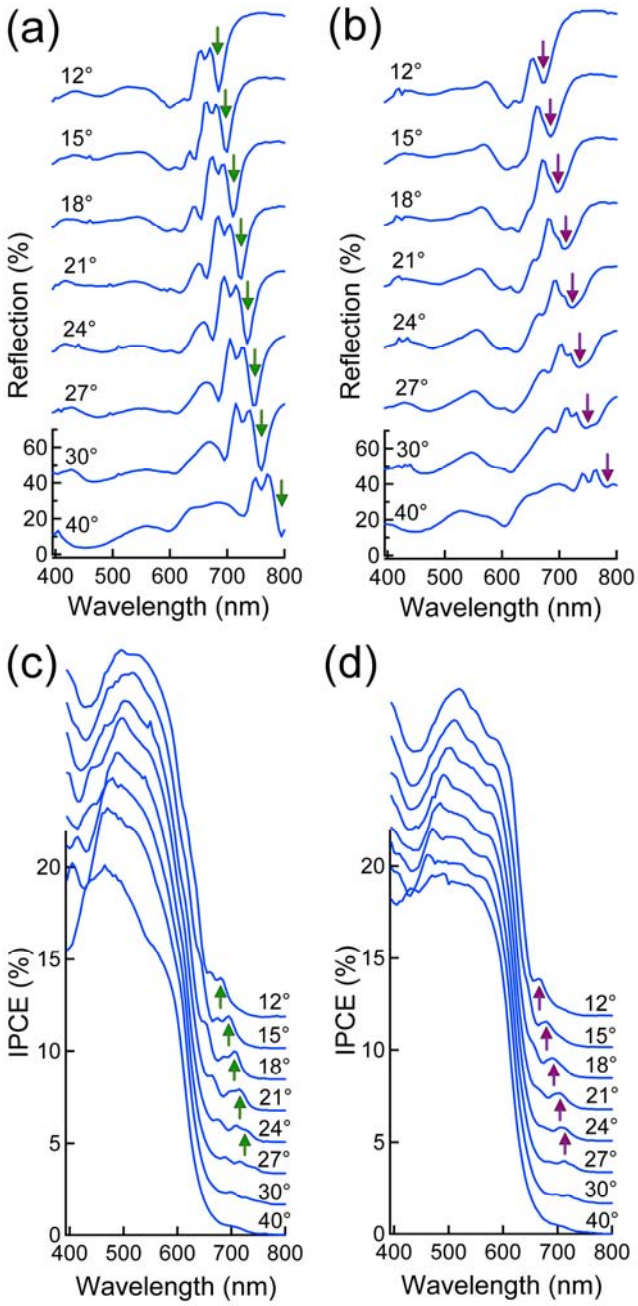

Figure 2.6. Angular dependent zeroth-order reflection and IPCE for PC cells for device No. 3; (a) p-polarized reflection, (b) s-polarized reflection, (c) p-polarized IPCE, and (d) s-polarized IPCE. The arrows denote sharp drops in reflection and corresponding increases in IPCE associated with resonant mode excitation.

the cell such as PEDOT:PSS and ITO have non-zero extinction coefficients and absorb in the near-IR. Optical simulations confirm that ITO and PEDOT:PSS absorb a significant fraction of resonant mode energy for these incident angles even at wavelengths where photocurrent is produced (see Figure 2.7). This limits the observed photocurrent enhancement. Even so, along with the results for normal incidence, this demonstration of significant photonic activity should motivate further studies of BHJ materials with PC geometries that have greater intrinsic performance capabilities including low-bandgap polymer blends.

2.3.6 Optical redistribution of incident light for Planar an PC cell

Losses in each individual layer are also calculated from the change in the z-component of the Poynting vector at each layer interface. All materials in the device, except the glass substrate and *nc*-ZnO, have non-zero extinction coefficients. Only absorption in the photoactive TDPTD:PCBM will contribute to photocurrent, so this is the loss of interest that is given in Figure 2.4 for photonic crystal and planar device No. 3. Determination of all the losses, including absorption in each layer along with zeroth order reflection and non-zero diffractive order scattering, is given in Figure 2.7 for device No. 3. Figure 2.7a and 7b show the photonic crystal cell under s-polarized illumination at normal incidence and 15º, respectively. Figure 2.7c shows the planar cell at normal incidence. As shown in Figure 2.6 of the manuscript, multiple resonant modes can be distinguished in both polarizations at non-normal incidence. The limited incident-photon-to-current conversion efficiency (IPCE) spikes associated with these modes under non-normal illumination is explained by the interception of a significant fraction of optical

energy by ITO and PEDOT:PSS. This is supported in Figure 2.7b for the resonant mode centered at $\lambda = 685$ nm.

As previously mentioned, calculation of the TDPTD:PCBM absorption (including the optical redistribution described above) can only be done after the measured zeroth order reflection is fitted to an appropriate optical model using the simulation method described above. An important point to note is that optical coherence is lost in the relatively thick (~1 mm) glass substrate, so it cannot be included directly in the simulation method. Reflection from the thin film stack (R) where light is incident from a semi-infinite glass substrate is first calculated via the simulation method. The actual reflection (R_{tot}) that is compared to measurement is then calculated from an equation that is a function of R and the reflection coefficient from an air/glass interface (R*). This procedure and subsequent equations are frequently used for optically modeling planar organic photovoltaic cells and is described elsewhere.[26] This also means that the absorption coefficients calculated in Figure 2.7 are determined by comparing the optical power per unit area lost in a given layer with that incident from glass.

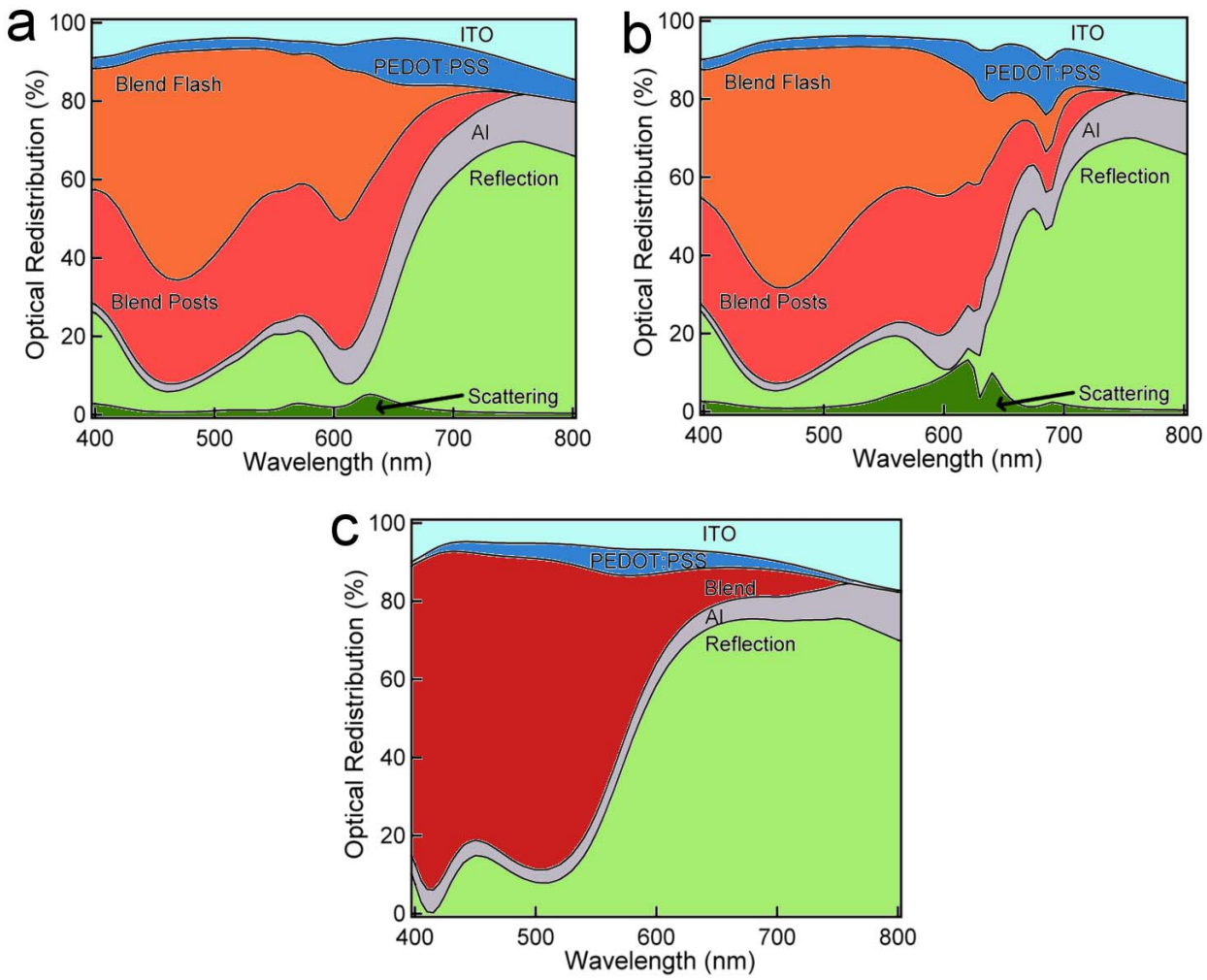

Figure 2.7. Optical redistribution for s-polarization at normal incidence for device No. 3. Photonic crystal device at (a) normal incidence and (b) 15º. (c) Planar device at normal incidence.

2.4 Conclusions

In summary, I have demonstrated the fabrication of BHJ organic solar cells with PC geometries. This has been achieved using the PRINT process where ordered arrays of submicron features can be made in a single step. The PC structure helps transcend the electrical performance constraints of a thin photoactive layer by boosting the *FF* and V_{oc}. Furthermore, it provides a method to target specifically desired regions of the solar spectrum for absorption enhancements via a photonic structure that exhibits multiple resonances.

2.6 References

(1). Peumans, P.; Bulović, V.; Forrest, S. R.; Forrest, S. R. *Appl. Phys. Lett.* **2000,** 76, 2650.

(2). Niggemann, M.; Glatthaar, M.; Lewer, P.; Müller, C.; Wagner, J.; Gombert, A. *Thin Solid Films* **2006,** 511-512, 628.

(3). Rim, S.-B.; Zhao, S.; Scully, S. R.; McGehee, M. D.; Peumans, P. *Appl. Phys. Lett.* **2007,** 91, 243501.

(4). Roman, L. S.; Inganäs, O.; Granlund, T.; Nyberg, T.; Svensson, M.; Andersson, M. R.; Hummelen, J. C. *Adv. Mater.* **2000,** 12, 189.

(5). Niggemann, M.; Glatthaar, M.; Gombert, A.; Hinsch, A.; Wittwer, V. *Thin Solid Films* **2004,** 451-452, 619.

(6). Na, S.-I.; Kim, S.-S.; Kwon, S.-S.; Jo, J.; Kim, J.; Lee, T.; Kim, D.-Y. *Appl. Phys. Lett.* **2007,** 91, 173509.

(7). Duché, D.; Escoubas, L.; Simon, J.-J.; Torchio, P.; Vervisch, W.; Flory, F. *Appl. Phys. Lett.* **2008,** 92, 193310.

(8). Tumbleston, J. R.; Ko, D.-H.; Samulski, E. T.; Lopez, R. *Appl. Phys. Lett.* **2009,** 94, 043305.

(9). Tumbleston, J. R.; Ko, D.-H.; Samulski, E. T.; Lopez, R. *Opt. Express* in press.

(10). Bermel, P.; Luo, C.; Zeng, L.; Kimerling, L. C.; Joannopoulos, J. D. *Opt. Express* **2007,** 15, 16986.

(11). Zhou, D.; Biswas, R. *J. Appl. Phys.* **2008,** 103, 093102.

(12). Na, S.-I.; Kim, S.-S.; Jo, J.; Oh, S.-H.; Kim, J.; Kim, D.-Y. *Adv. Funct. Mater.* **2008,** 18, 3956.

(13). Cocoyer, C.; Rocha, L.; Sicot, L.; Geffroy, B.; de Bettignies, R.; Sentein, C.; Fiorini-Debuisschert, C.; Raimond, P. *Appl. Phys. Lett.* **2006,** 88, 133108.

(14). Kim, M.-S.; Kim, J.-S.; Cho, J. C.; Shtein, M.; Guo, L. J.; Kim, J. *Appl. Phys. Lett.* **2007,** 90, 123113.

(15). Hampton, M. J.; Williams, S. S.; Zhou, Z.; Nunes, J.; Ko, D.-H.; Templeton, J. L.; Samulski, E. T.; DeSimone, J. M. *Adv. Mater.* **2008,** 20, 2667.

(16). Liu, J.; Kadnikova, E. N.; Liu, Y.; McGehee, M. D.; Frechet, J. M. J. *J. Am. Chem. Soc.* **2004,** 126, 9486.

(17). Beek, W. J. E.; Wienk, M. M.; Kemerink, M.; Yang, X.; Janssen, R. A. J. *J. Phys. Chem. B* **2005,** 109, 9505.

(18). Liu, J.; Kadnikova, E. N.; Liu, Y.; McGehee, M. D.; Fréchet, J. M. J. *J. Am. Chem. Soc.* **2004,** 126, 9486.

(19). Gilot, J.; Barbu, I.; Wienk, M. M.; Janssen, R. A. J. *Appl. Phys. Lett.* **2007,** 91, 113520.

(20). Gilot, J.; Wienk, M. M.; Janssen, R. A. J. *Appl. Phys. Lett.* **2007,** 90, 143512.

(21). Roest, A. L.; Kelly, J. J.; Vanmaekelbergh, D.; Meulenkamp, E. A. *Phys. Rev. Lett.* **2002,** 89, 036801.

(22). Yip, H.-L.; Hau, S. K.; Baek, N. S.; Ma, H.; Jen, A. K. Y. *Adv. Mater.* **2008,** 20, 2376.

(23). Dennler, G.; Forberich, K.; Scharber, M. C.; Brabec, C. J.; Tomis, I.; Hingerl, K.; Fromherz, T. *J. Appl. Phys.* **2007,** 102, 054516.

(24). Tikhodeev, S. G.; Yablonskii, A. L.; Muljarov, E. A.; Gippius, N. A.; Ishihara, T. *Phys. Rev. B* **2002,** 66, 045102.

(25). Mihailetchi, V. D.; Koster, L. J. A.; Hummelen, J. C.; Blom, P. W. M. *Phys. Rev. Lett.* **2004,** 93, 216601.

(26). Persson, N.-K.; Arwin, H.; Inganas, O. *J. Appl. Phys.* **2005,** 97, 034503.

Chapter III

APPLICATION OF PHOTONIC CRYSTALS FOR STANDAR AND INVERTED ORGANIC SOLAR CELLS

3.1 Introduction

The incongruity between optical and electrical requirements with regard to the photoactive layer thickness results in a compromise that degrades the optimal efficiency of organic photovoltaic (OPV) cells.[1-3] In theory, a photonic crystal (PC) is a candidate nanopattern for improving absorption over a range of wavelengths acting as resonant structures and low loss mirrors.[4] However the complicated process for fabricating PC nanopatterns over wide areas has been the primary barrier to adopting its advantages in solution processing of the inexpensive OPV components. To date, only a limited number of 1-D periodic PC designs have been reported presumably because of fabrication difficulties.[5, 6, 7, 8, 9,] The intricacies of PC nanopatterns, the range of feasible PV materials, and the device architectures, severely limit the conventional lithographic process of PC fabrication. In Chapter 2, I showed a route to fabricate scalable 2-D PC nanopattern in OPV devices via a facile processing strategy called PRINT[10, 11] that exhibited enhanced performance.[12] However, I was restricted to using a low efficiency BHJ system, TDPTD (thermally deprotectable polythiophene derivatives):PCBM. In this chapter, I explore that the benefit of PC geometry in OPV devices may be extended to the high-performance BHJ materials (P3HT:PCBM)[13] in both standard and inverted[14] cell architectures. This was enabled by the insertion of a robust photoactive layer underneath the PC-patterned BHJ layer, which in turn, provided extended the absorption to longer wavelength.

In this chapter, I demonstrate the flexibility of PRINT by presenting geometries of various nanopattern shapes and materials. The device performance for PC and planar control cells is evaluated from both the optical and the electrical points of view. Specifically, I show theoretically and experimentally how optical interference can greatly affect absorption in the photoactive layer depending on the device architecture. When absorption is maximized for both

PC and planar cells with P3HT:PCBM BHJ materials, an enhancement of 13% is possible. A portion of this enhanced absorption comes in the form of resonant mode excitations that are observed for many PC cells.[6, 7, 12, 15]

3.2 Experimental sections

3.2.1 TiO_2 sol-gel synthesis

TiO_2 sol-gel was prepared by previously reported method.[16] 10mL of titanium isopropoxide (Aldrich, 99.999%) precursor, 50mL of 2-methoxy methanol (Aldrich, ≥99.9%) and 5mL of ethanolamine (Aldrich, ≥99%) were mixed in argon gas condition. The solution was heated at 80°C for 2 hrs with vigorous stirring and subsequently heated at 120°C for 1hr. The heating steps were repeated. In order to get desired thickness of TiO_2 (or TiO_x) layer by spincasting, the solution was diluted with isopropyl alcohol.

3.2.2 Nanocrystalline ZnO (*nc*-ZnO) synthesis

The nanocrystalline ZnO was prepared according to the method by Beek et al[S2]. The reaction was carried out in a two-neck flask with a condenser and dropping funnel. Zinc acetate dihydrate (Aldrich >98%, 2.95g) was dissolved in methanol (125 ml) at 60°C for 1hr; a Potassium hydroxide solution (Fisher 86.6%, 1.48 g) in methanol (65 ml) was added to the Zinc acetate dihydrate solution dropwise over 15 min at 60°C under vigorous stirring conditions for 130 min. After completion of the reaction, the heater was removed and the solution was cooled to room temperature over 2 hrs. The solution was centrifuged and the resulting solid was washed with methanol; this was repeated three times. The resulting nanocrystalline zinc oxide (nc-ZnO)

was analyzed by a JEOL 100CX II transmission electron microscopy, and the mean diameter of the nc-ZnO particles was about 5nm.

3.2.3 Nanopatterning procedures by PRINT

In order to make PC nanopatterns, PRINT technique was introduced.

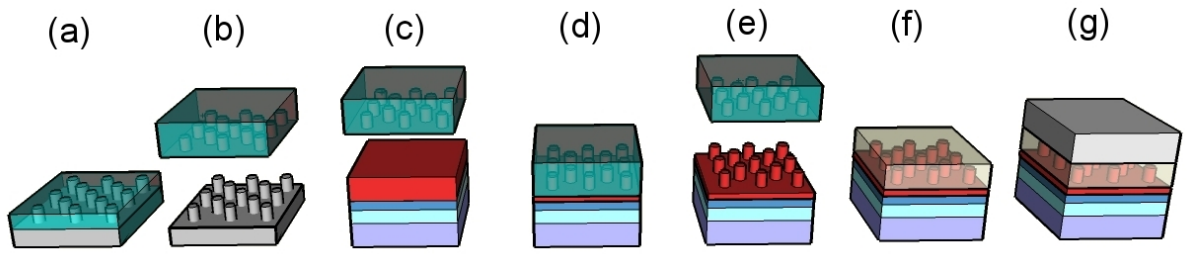

Figure 3.1. Schematic of the PRINT method (a) A dimethacrylated-funtionalized PFPE was prepared and poured over a nanopatterned silicon master template (b) The nanopattened PFPE replica mold was generated by photochemically curing the PFPE. (c) A P3HT:PCBM solution was spin-coated on the PEDOT:PSS-coated substrate (d) The new layer was patterned with the prepared perfluoropolyether (PFPE) mold under pressure at 145°C for 30 min. (e) The PFPE replica was peeled off the substrate to give highly ordered and regular nanopatterns over the specified substrate area. (f) nc-ZnO solution in methanol was spincoated on the nanao-patterns (g) Aluminum was thermally deposited to complete the device.

3.2.4 Device fabrication

In order to study PC effect with various device configurations, standard and inverted organic photovoltaic cells were prepared. In table 3.1, each device configuration was summarized.

3.2.4.1 PT devices

ITO-coated glass was cleaned with acetone, isopropyl alcohol and distilled water for 10min each, and then dried overnight in an oven (150 ˚C). The cleaned substrate was treated with UV Ozone for 20min (UVO Cleaner 42, Jelight Company Inc.). The PEDOT:PSS (Baytron PH 500) was filtered with a 0.45μm PVDF filter and then 30 nm of PEDOT:PSS was spincoated onto the substrate and annealed for 10 min at 140°C. The annealed sample was moved into a inert gas (purified nitrogen) glove box. In order to prepare the flash layer, a solution containing P3HT (15 mg mL^{-1}) and PCBM (12 mg mL^{-1}) in chlorobenzene was spincoated onto the PEDOT:PSS-coated substrate. The spincasted layer is patterned by contacting a perfluoropolyether (PFPE) mold under pressure (18 kilogram-force centimeter) at 145°C for 30 min, a variation of the PRINT methodology.[5, 11]; the planar cell is simultaneously fabricated by "embossing" the layer with a flat PFPE "mold." The patterning step is followed by spincoating various concentrations of *nc*-ZnO[17] in methanol to get the desired thickness of *nc*-ZnO film. Finally the device was transferred into a vacuum chamber (2×10^{-6} torr) and 100 nm Al was deposited on defined cell areas (12 mm^2). The device structures were characterized by SEM (Hitachi S-4700).

3.2.4.2 PT-Cu devices

The copper phthalocyanine (CuPC) film (13nm) was thermally deposited with 0.2 Å/s rate on the PEDOT:PSS layer prepared by the above mentioned way. The following patterning and metal deposition processes were identical to process for the PT.

3.2.4.3 iPT devices

The TiO_2 sol-gel was prepared by the previously reported method.[16] The TiO_2 sol-gel was spincasted on the cleaned ITO, and the film was annealed at 450°C for 30 min. to form crystalline TiO_2. The P3HT:PCBM solution was spincoated on the TiO_2 layer (10nm) and was embossed with PFPE at 145°C for 30min for planar and PC cell. Finally the device was transferred into a vacuum chamber (2×10^{-6} torr) and the Ag / WO_3 layers were subsequently thermally deposited on the both area.

3.2.4.3 iPT-Ti devices

The TiOx nano-patterns was formed by embossing the prepared TiO_2 sol-gel with PFPE mold and subsequent annealing the film at 150°C for 90min. The identical P3HT:PCBM solution was spincoated on the patterned and planar TiO_x layer and the devices were annealed at 145°C for 30min. The device was completed by depositing the Ag / WO_3 layers in a vacuum chamber (2×10^{-6} torr).

3.2.5 Device measurement

All measurements were performed in inert gas fulfilled glove box at room temperature. Current-Voltage performances are achieved by Ketheley 2400 source meter with exposure of 85mW/cm^2 light, made from Oriel-Newport 300W solar simulator. Solar spectrum was modulated by AM 1.5 filter without additional filter. The intensity of solar simulator was measured by a standard silicon photovoltaics calibrated by the National Renewable Energy Laboratory. The angular reflections were measured in s-polarizations with s-polarization rotated 90º around the 400 nm periodicity of the hexagonal photonic crystal.

3.3 Results and discussion

3.3.1 Replication of nanopatterns by PRINT

Figure 3.2 shows a variety of nanopatterns of P3HT:PCBM and amorphous titanium oxide (TiO_x)[16] made by PRINT including triangle, rectangle, grating and columnar structures. The PRINT method[10, 12, 18] was used to fabricate a precision PC of P3HT:PCBM and amorphous titanium oxide (TiO_x)[16] over large areas (2.50 cm x 1.25 cm). For standard OPV device application, nanopatterns of P3HT:PCBM were replicated in PEDOT:PSS (Poly(3,4-ethylenedioxythiophene):poly(styrenesulfonate)) on ITO, while TiO_x was patterned on an ITO substrate for inverted OPV (iOPV) cells. All replicated patterns are periodic with PC dimensions and each includes a "flash layer" below the nanopatterned features as shown in Figure 3.2e. The hexagonal array of column-like features was chosen for this study as its 2-D periodicity is capable of enhancing absorption of both polarizations of light, and a 400 nm periodicity when coupled with the inherent optical properties of the nanopatterned materials resulted in resonant modes near the band edge of P3HT:PCBM.

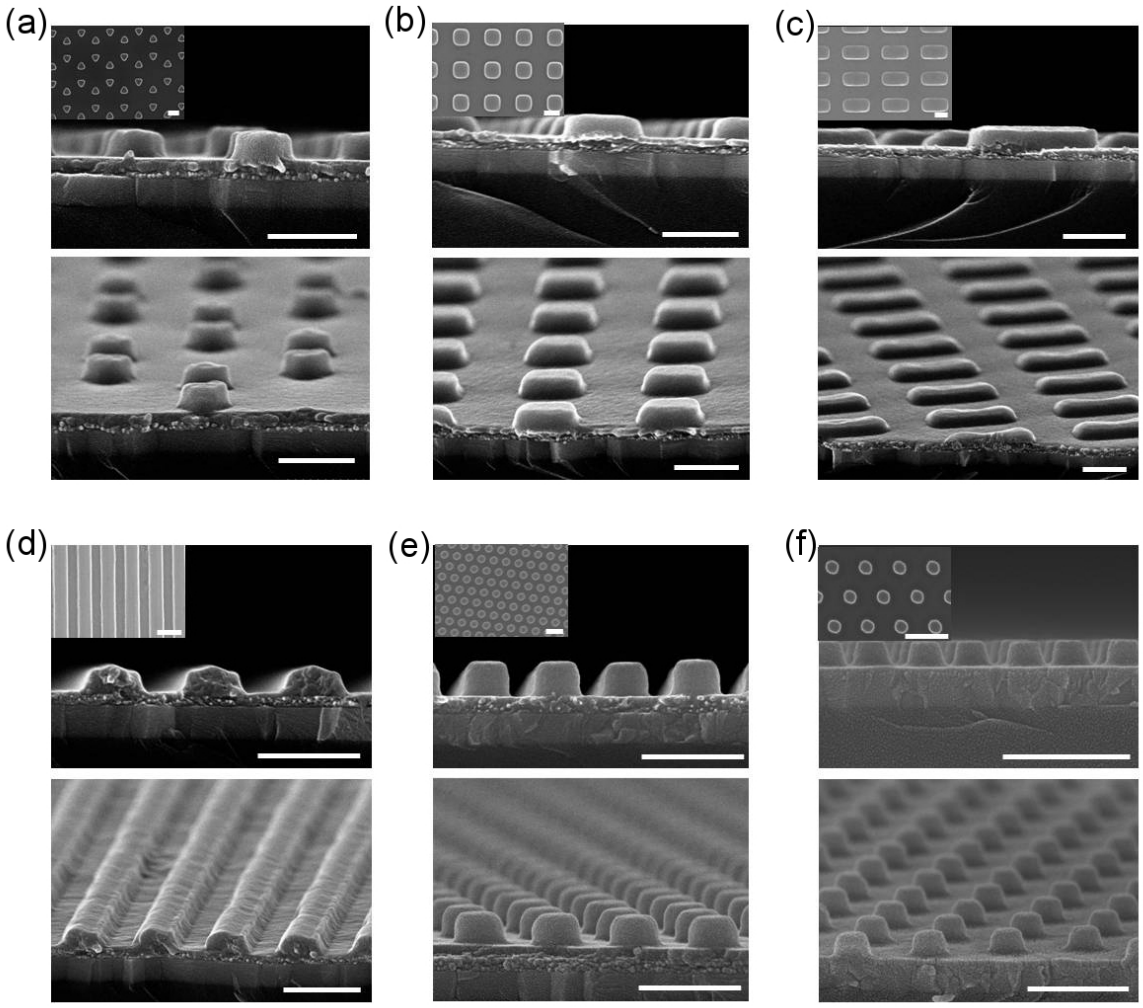

Figure 3.2. SEM (Scanning electron microscope) pictures for P3HT:PCBM replicas of PC nanopatterns using PRINT to fabricate features having a range of geometries: (a) hexagonal (b) square (c) rectangular (d) linear grating, and (e) rows of columns. All patterns (a-e) are embossed on a PEDOT:PSS/ITO substrates. In (f) columnar hexagonal TiO_x nanopatterns were prepared on an ITO substrate. SEM pictures show respectively cross section views (top) and oblique views (bottom) with corresponding normal views (insets). Scale bars are 500 nm.

3.3.2 Optical properties for PC cells

For device applications, the nanopatterened P3HT:PCBM or TiO_x was incorporated into the OPV and iOPV devices. The photonic effect depends on a large refractive index contrast between the two adjacent nanopatterned layers[19], as a result, the PC cell was designed to incorporate a low index material (*nc*-ZnO) into the nanopatterned BHJ layer or conversely, incorporating the BHJ layer into the nanopatterned TiO_x. For instance, if the 2-D PC topography is embossed into the BHJ layer, a relatively high refractive index mixture (~2.1 at 550 nm in Figure 3.3), it is surrounded by nano-crystalline zinc oxide (*nc*-ZnO), a relatively low refractive index material (~1.4 over whole wavelength range 400 nm – 800 nm). The resulting interdigitated morphology of the patterned P3HT:PCBM and *nc*-ZnO surround has sufficient optical contrast to exhibit PC behavior. Likewise, the patterning of low index TiO_x when surrounded by P3HT:PCBM also meets the PC refractive index requirement (see Figure 3.3). For some devices where the evaporated metal electrode partially filled the nanopattern and its surrounding matrix, interesting photonic activity was observed. This was the case for OPV devices where only partial filling of *nc*-ZnO occurred and for iOPV devices with thin overlayers of WO_3.

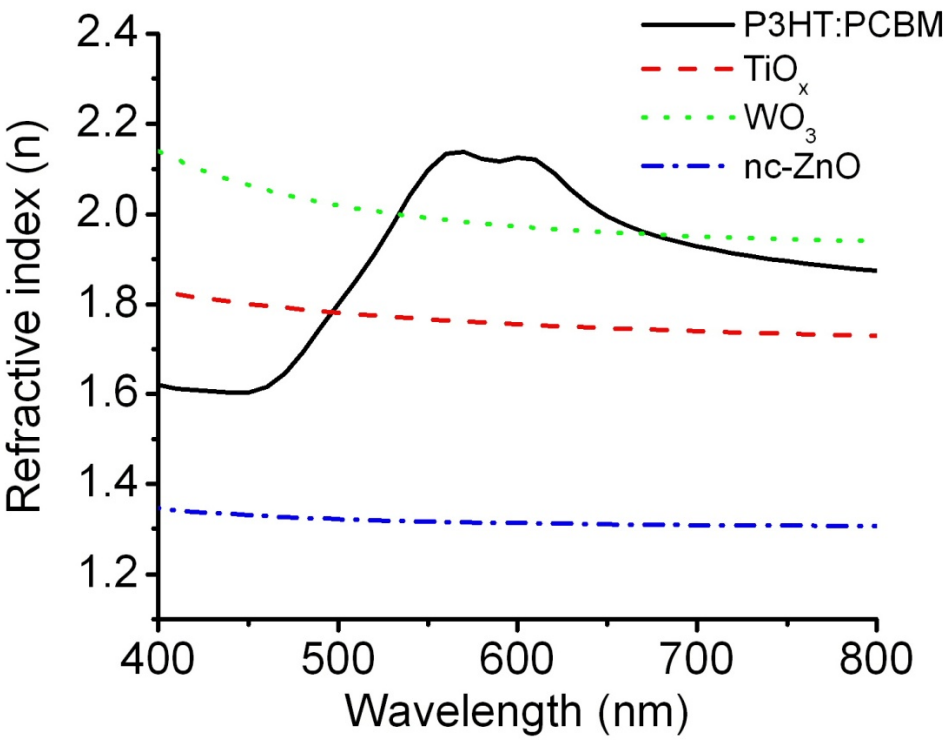

Figure 3.3. Refractive indices of P3HT:PCBM, TiO_x, WO_3 and *nc*-ZnO film.

3.3.3 Device application for PC cells

With the optical properties of the components in mind, both standard OPV and iOPV devices were fabricated. The configurations of the prepared devices is summarized in Table 3.1, and Figure 3.4 shows (a) a photograph, (b, c, d) scanning electron micrograph (SEM) cross sections, and (e) schematics of planar and nanopatterned PC cells for PT devices. For the PC cell as shown in Figure 3.4e, the flash layer was introduced along with the nanopattern during the PRINT process. However, as the thickness of the flash layer affects the absorption of incident light, the flash layer thickness was fixed to 40nm. (The optical effect of the flash layer will be discussed below.) Also, the thicknesses of layers adjacent to the nanopatterns that generate a large refractive index contrast are defined as d_2 and d_3 and correspond to d_1 for the planar cell (see Figure 3.4e).

Table 3.1. The configurations of PC and planar cells; the bold faced components are the PC nanopatterns on standard and inverted devices. The photoactive material (P3HT:PCBM) was nanopatterned in PC cells for PT, PT-Cu, and iPT devices, whereas the TiO_x was nanopatterned in PC cells for the iPT-Ti device. The layer embossed with PFPE film in each cell is indicated by "planar" or "PC" for flat and nanopatterned cells, respectively. The nanopatterned features are surrounded by an "overlayer" which has sufficient optical contrast to exhibit photonic crystal behavior. In addition to the thickness of the overlayer in the planar cell (d_1), the thickness of "filler" between PC features (d_2), and overlayer above the PC columns (d_3), are important variables that influence the absorption performances. A detailed device configuration is shown in Figure 2 (e). All devices were prepared on the ITO (150 nm) substrate, and PEDOT:PSS (35nm) and Al (100nm) were used for the standard devices.

OPV device type	Name	Architecture	Dimension (nm) planar[a], PC[b]	Dimension (nm) d_1, d_2, d_3
Standard	PT	ITO/PEDOT:PSS/ **P3HT:PCBM**/*nc*-ZnO /Al	90, 180	90, 190, 10
Standard	PT-Cu	ITO/PEDOT:PSS/CuPC/**P3HT:PCBM**/*nc*-ZnO/Al	80, 170	90, 200, 20
Inverted	iPT[c]	ITO /TiO_2/**P3HT:PCBM** /WO_3/Ag	95,180	10, 10, 10
Inverted	iPT-Ti[d]	ITO/**TiO_x**/P3HT:PCBM/ WO_3/Ag	40, 135	95, 150, 40

[a] : Thickness of the embossed layer for planar cell.
[b]: Height of the replicated nanopatterns for PC cell.
[c]: For iPT devices, TiO_2 (10nm) and Ag (120nm) were incorporated.
[d]: For iPT-Ti devices, WO_3 (30nm) and Ag (100nm) were deposited.

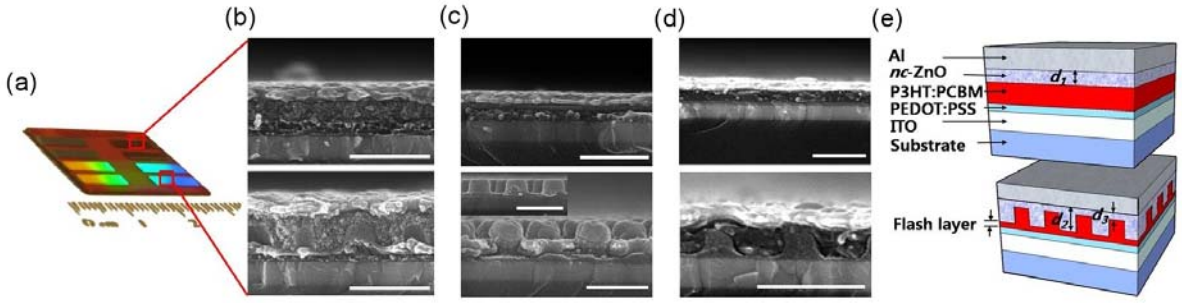

Figure 3.4. (a) Photograph of planar and iridescent PC organic solar cells on the same device; (b, c, d)) SEM pictures showing the planar (top) and PC cell (bottom); (e) device schematic architectures. The respective device structures are (b) PT (Al/ *nc*-ZnO / P3HT:PCBM / PEDOT:PSS / ITO), (c) iPT (Ag/ WO_3 / P3HT:PCBM / TiO_2 / ITO) and (d) iPT-TI (Ag / WO_3 / P3HT:PCBM / TiO_x / ITO). The PC geometries were prepared by patterning either the P3HT:PCBM (b, c) or the TiO_x layer (d).

Figure 3.4b shows SEM cross sections for PC and planar cells for PT device, showing the photoactive layer (P3HT:PCBM) patterned on PEDOT:PSS for the standard OPV device. In order to make meaningful comparisons between planar and PC cells, the same volume of photoactive layer (P3HT:PCBM) was incorporated into both by preparing them simultaneously on the same device substrate. This insured that both kinds of cells were subjected to the same fabrication steps and thermal history. During the PRINT step, the planar cell was "embossed" with a featureless flat perfluoroelastomer (PFPE) film while the PC cell was contacted with the nanopatterned PFPE mold. The thickness of the planar photoactive layer in the control cells was held constant at 90 nm. The two types of cells can be readily distinguished by the iridescent color reflected at glancing angles from the PC morphology (Figure 3.4a). The actual photoactive P3HT:PCBM layer in the PC cell consists of a flash layer (40 nm) covered by a hexagonal array of column-like features (Figure 3.4b) with height = 180 nm, dia. = 220 nm, and a translational periodicity of 400 nm. Subsequently, the *nc*-ZnO "filler" or surround layer in the PC cell (and the *nc*-ZnO "spacer" layer in the planar cell) was formed by spin-coating a dispersion of freshly synthesized *nc*-ZnO[17] (~5 nm diameter particles) in methanol on both the planar and the molded bulk heterojunction stratum. Finally Aluminum (Al, 100 nm) was thermally deposited for electrical contact.

The PRINT method was used to build a PC architecture in a tandem cell design (PT-Cu)[20, 21] prepared by placing a thin (13 nm) layer of copper phthalocyanine (CuPC) underneath P3HT:PCBM. The IR region of the solar spectrum where P3HT:PCBM cannot contribute to the photocurrent generation is utilized by the CuPC absorption. CuPC has low absorption bands between 400 and 550 nm where P3HT:PCBM absorbs strongly, however it has strong absorption above 550nm as shown in Figure 3.5. Also, the HOMO (3.5 eV) and LUMO (5.2 eV) of CuPC[20]

is well matched with P3HT:PCBM energy levels for favorable carrier transport. CuPC was thermally deposited on PEDOT:PSS / ITO, and the PC and planar cells were fabricated on the same substrate by embossing the spincoated P3HT:PCBM layer with a PFPE mold. Subsequently, *nc*-ZnO and Al were deposited in the same manner as for the PT device.

In inverted OPV architectures (iPT, iPT-Ti), nanopatterns in the photoactive layer (P3HT:PCBM) and in the inorganic electron transporting layer (TiO_x) were respectively formed. Finally, WO_3 / Ag layers were subsequently thermally deposited on the both cells (see Figure 3.4c and 3.4d). Further detailed processes for device fabrication were described in experiment section.

3.3.4 Optical performances for PC and planar cells in each device

In order to characterize the optical performance of PC and planar cells, the reflection spectra for both the planar and PC cells were measured with s-polarized light (Figure 3.6a). Even though absorption in the photoactive blend cannot be measured directly, the reflection spectrum of the entire cell is an effective indicator of absorption losses in the device due to the negligible transmission through the metal cathode and minimal scattering close to normal incidence. Figure 3.3shows the respective reflection spectra for PC and planar cells for each device that are characteristic of the device architecture and material components. The PC cell in PT and PT-Cu (Figure 3.6a, 3.6b) devices shows absorption enhancement due to lower reflection. The loss of reflection at certain wavelengths is apparent to the naked eye (insets of Figure 3.6a). On the other hand, iOPV devices have similar reflection spectra for planar and PC cells especially in the visible region as shown in Figure 3.4c and 3.4d. This mainly arises from

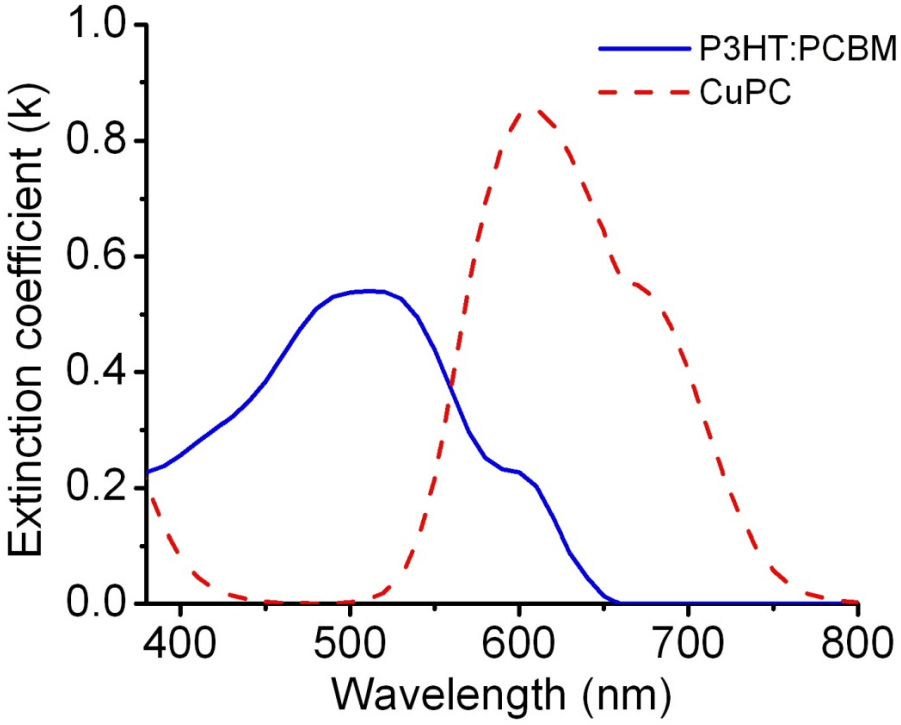

Figure 3.5. Extinction coefficients of P3HT:PCBM and CuPC film

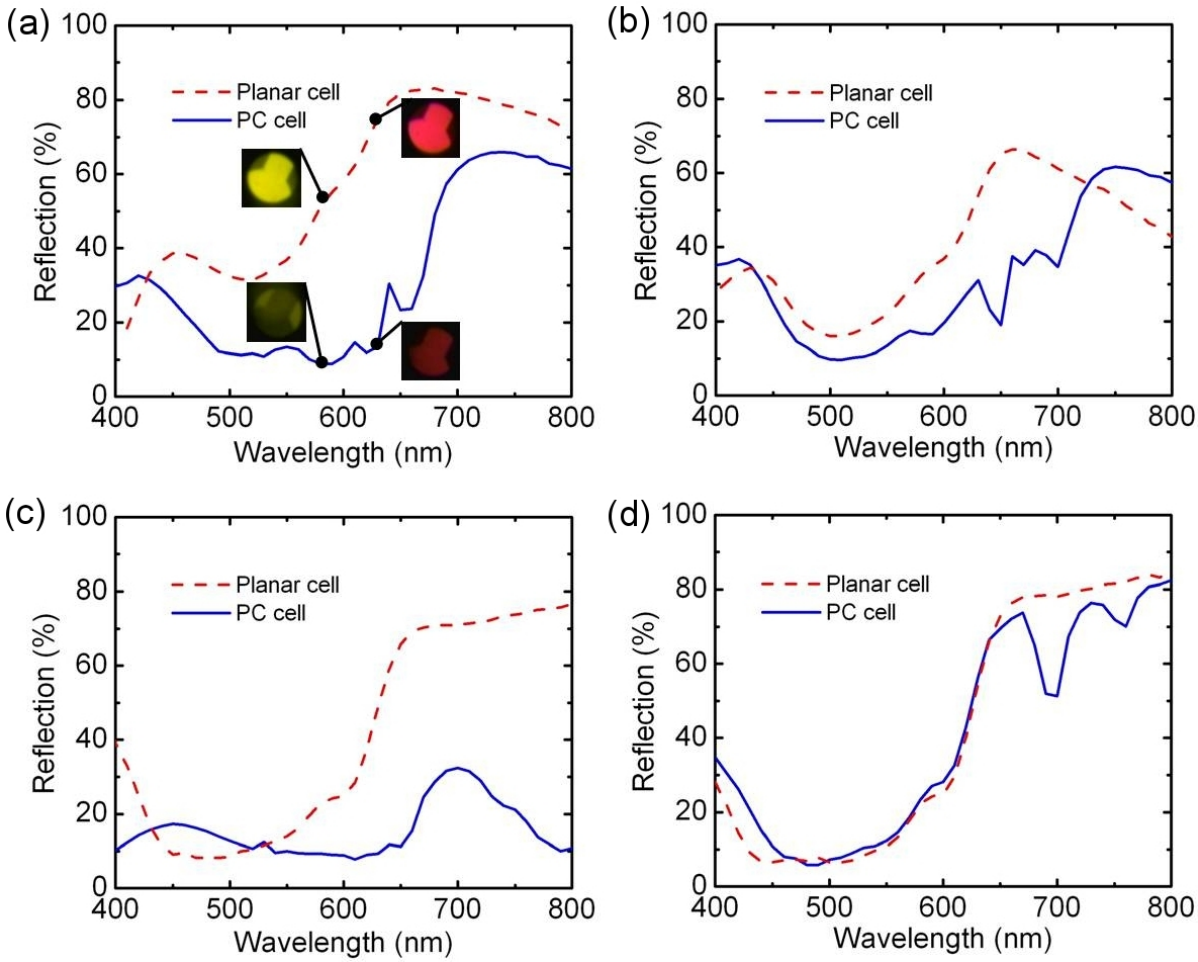

Figure 3.6. Zeroth order reflection for PC and planar cells for s-polarized light at 15 degree incidence for standard cell architecture; (a) PT and (b) PT-Cu, and inverted cell architecture; (c) iPT and (d) iPT-Ti.

differences in optical interference for each cell in respective device. For instance, absorption in the photoactive layer is not only controlled by the absorption coefficient of the blend, but also by the each layers' reflective index and physical dimensions. For the case of PC cells, physical dimensions such as height and periodicity of the nanopatterned layer also plays an important role[22-24]. This must be critically evaluated for each device type and will be discussed below in further detail.

3.3.5 Excitation of resonant modes for PC cells in standard and inverted OPV devices

The unique absorption enhancements in PC cells are partially due to the excitation of resonant modes which trap incident light in the photoactive layer. This is demonstrated in Figure 3.7a where the presence of reflection losses corresponds to light trapping by the photonic structure. There is a dramatic loss of reflection between 640 nm and 760 nm depending on the incident angle. The spectral location of the peaks varies as the incident angle changes from 12° to 30°. Likewise, resonant modes were also observed in iOPV device as shown in Figure 3.7b where contribution of these modes to the overall photocurrent is small due to the small absorption by the photoactive layer.

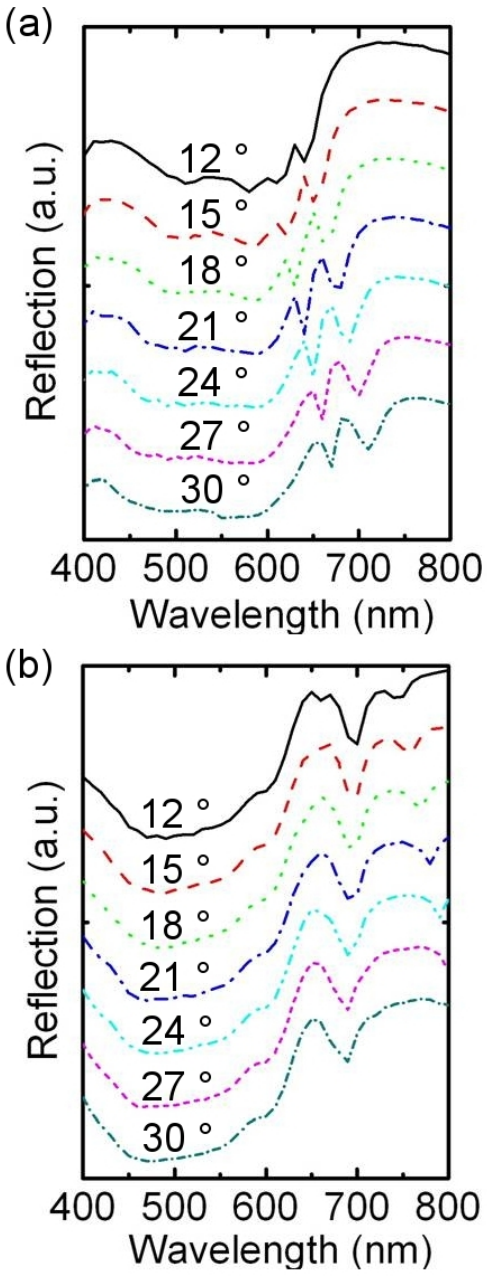

Figure 3.7. Angular dependent reflection spectra for PC cellin (a) PT and (b) iPT-Ti devices. The dips in reflection between 600 nm and 800 nm as the incident angle changes indicate the excitation of resonant modes.

3.3.6 Optical redistribution of lights and current-voltage performance for PC and planar cells

Even though device reflection characteristics are a good indicator of absorption, an optical model of the device is an invaluable tool to parse absorption in the photoactive layer and other lossy components of the cell. For instance, PEDOT:PSS, ITO, and Al also absorb light and reduce reflection, but do not produce photocurrent. So it is important to fully characterize absorption in each layer because even resonant modes may be trapped in PEDOT:PSS and ITO.[12] By fitting a solution to Maxwell's equations to the measured reflection data,[12] the optical redistribution of incident light in PT device was calculated for PC and planar cells (Figure 3.8a and 3.8b). Considerable absorption (~42%) occurs in the relatively thin (40nm) photoactive flash layer, while Al and PEDOT:PSS also contribute to absorption above 670 nm where P3HT:PCBM is transparent. By multiplying the fraction of absorption in the photoactive layer from optical redistribution of light by the AM 1.5 solar spectrum and integrating the calculated values spectrally, the exciton generation rate under 1 Sun conditions was obtained. The exciton generation rate showed that the absorption by P3HT:PCBM in the PC cell was enhanced by about 50% relative to the planar cell, and this is apparent in the J-V measurement. Under 85mW/cm^2 illumination, the J_{sc} for PC cell (8.93 mA/cm^2), was 40% higher than the planar cell (6.36 mA/cm^2), as shown in Figure 3.8c, which is in agreement with the absorption enhancement predicted by the optical model. Finally, the efficiency for the PC cell is 2.91% with 0.61V open circuit voltage (V_{oc}) and 46% fill factor (FF).

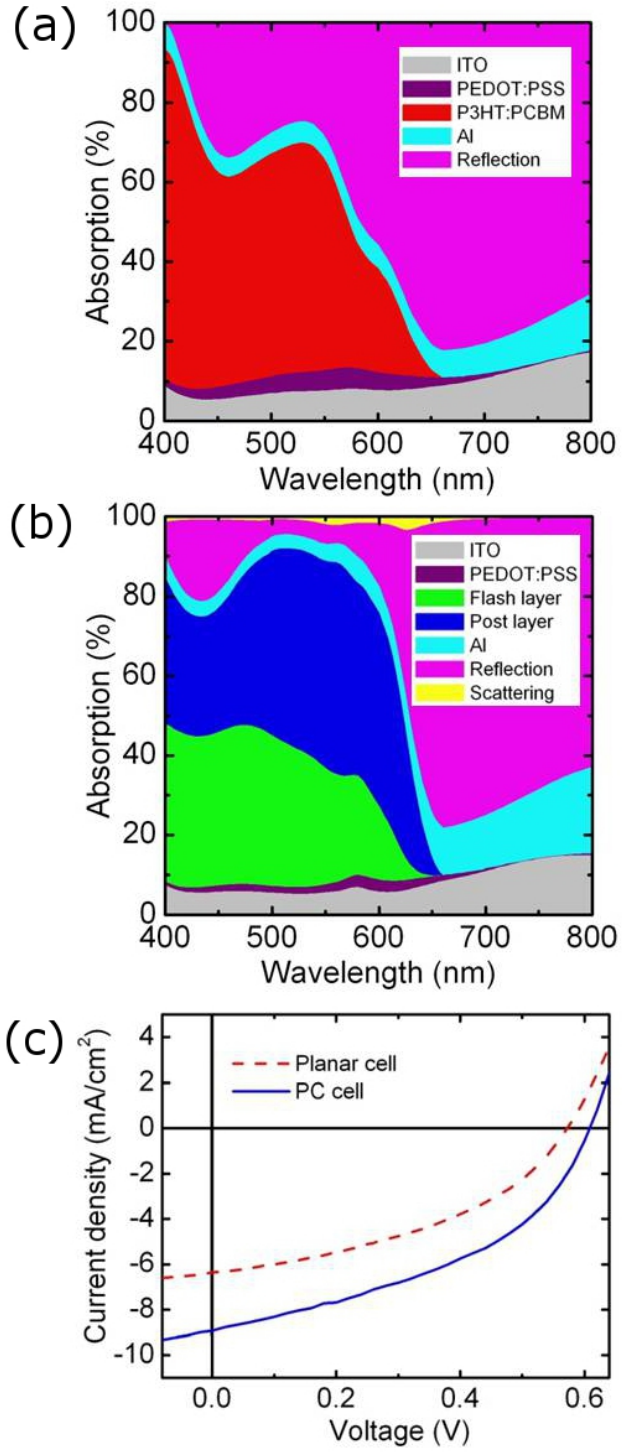

Figure 3.8. Optical redistributions at normal incidence for (a) planar and (b) PC cells for PT device. The current - Voltage (J-V) behavior for PC and planar cells (c) exhibit the absorption enhancement predicted by the optical model.

3.3.7 Critical parameters for PC cells

3.3.7 Parameters for device performance for PC cells

Even though the PC cells for PT device shows an enhanced absorption and J_{sc} relative to the planar cell fabricated on the same substrate, optical interference plays a major role in determining absorption and the resulting J_{sc} for both PC and planar cells. For instance, the thickness of the transparent PC surround filler material, *nc*-ZnO, affects absorption characteristics making it important to explore a range of thicknesses to determine the maximum absorption.[25, 26] Figure 3.9a shows the spectrally-integrated P3HT:PCBM absorption calculated with the optical model as a function of the *nc*-ZnO thickness for PC and planar cells. This value is deemed the exciton generation rate as it takes into account the AM 1.5 solar spectrum and the optical redistribution of incident light in all constituted layers (see Figure 3.8a and 3.8b). Here the thickness of the *nc*-ZnO layer (d_3) above the BHJ columns was varied while keeping the *nc*-ZnO thickness (d_2) between the columns fixed to the column height (180 nm). This resulted in a variation in the thickness of the *nc*-ZnO layer for the planar cell (d_1) (see Figure 3.4e). Absorption for both PC and planar cells oscillated with *nc*-ZnO thickness with a ~90% variation from maximum to minimum for the planar devices. Comparing the peak values of exciton generation rate for each cell suggests a 13% absorption enhancement for PC cells. However, further enhancement would be possible via idealized geometry for PC nanopatterns in P3HT:PCBM devices.[27] The measured reflection data were fit to the optical model enabling the calculation of the absorption. As shown in Figure 3.9a, the measured values were well matched with calculated values.

Using the calculated absorption values, the J_{sc} in the photoactive layer was calculated assuming an internal quantum efficiency (IQE) of unity and illumination with AM1.5 at 100mA/cm^2 (Figure 3.9b).[28] The variation in the absorption with *nc*-ZnO thicknesses impacts the calculated J_{sc} and is compared with experiment in Figure 3.8c. Since the *nc*-ZnO is an additional electron transporting layer, its thickness may affect the electrical device performance. The IQE is a measure of the electrical processes in cells at short circuit and could be calculated by dividing the optical absorption by the measured J_{sc} However the IQE is relatively constant regardless of *nc*-ZnO thickness as shown in Figure 3.9c. Therefore, it was presumed that the high conductivity *nc*-ZnO was not a critical parameter for device performance indicating that the observed change in J_{sc} with *nc*-ZnO thickness is an optical effect.

Another factor that affects absorption in the PC cell is the flash layer thickness. The PV-active blend layer thickness is 90 nm in planar cells. A comparable blend volume in the PC cell must be partitioned between the flash layer and the PC nanopattern. In Figure 3.9d, normalized exciton generation rates for PC cells were obtained as a function of flash layer thickness at the fixed *nc*-ZnO thickness (d_3 = 20 nm). A thinner flash layer will allow more blend to be used in the patterned PC layer, which in turn, increases the photonic activity as shown in Figure 3.6d. PC cells with high aspect ratio patterns are less sensitive to *nc*-ZnO thickness (less variation in absorption with thickness, see Figure 3.10), however, thin flash layers are susceptible to shorting via direct contact between the *nc*-ZnO and PEDOT:PSS interface. Therefore, control of the flash layer thickness is crucial for both electrical and optical performance. Herein the thickness of the flash layer was controlled by the applied pressure during the PFPE embossing process, and the initial thickness of the photoactive blend to be patterned. We observed that 15 inch/pounds pressure consistently yielded a 40 nm flash layer in the PC cells. Earlier we reported that the

flash layer thickness could be controlled by preparing an insoluble PV film layer by thermal curing, and subsequent PC patterning showed enhanced performance.[12] Alternately the incorporation of an additional layer underneath the photoactive layer is an option if the additional

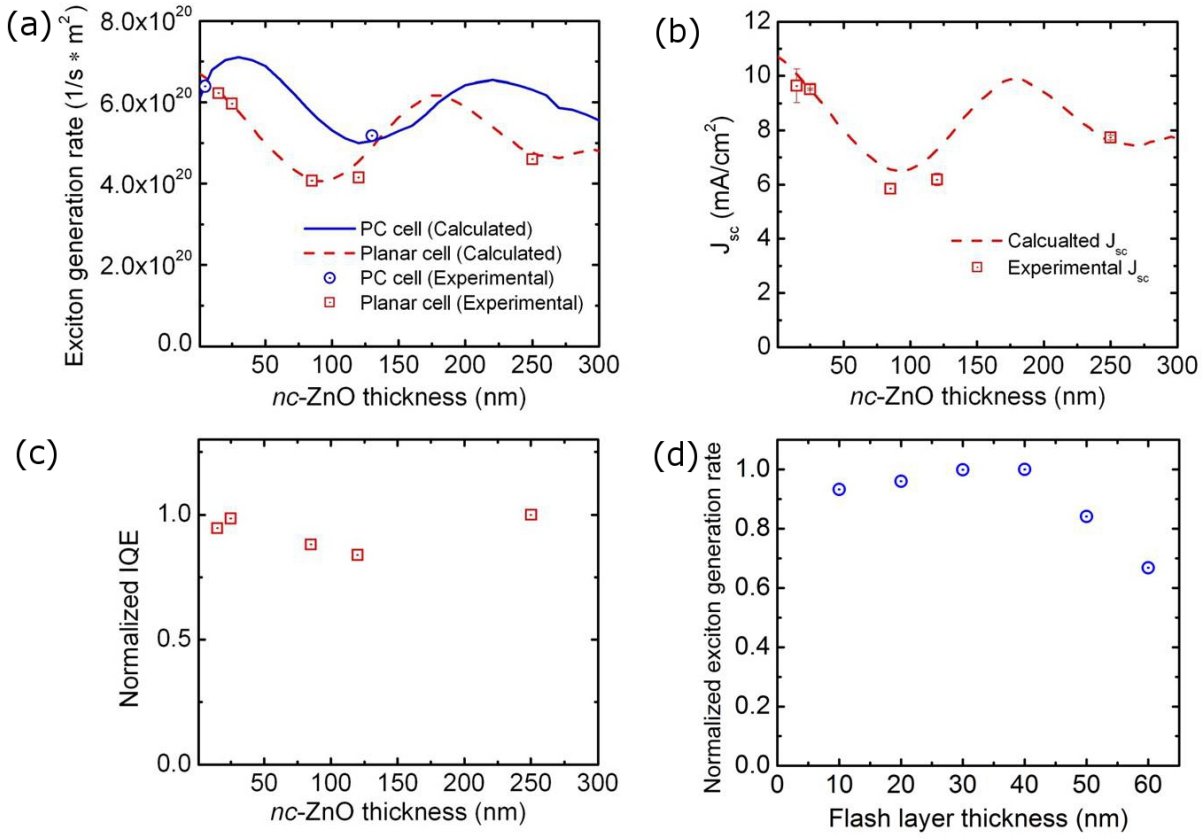

Figure 3.9. Calculated and experimental (a) exciton generation rates and (b) short circuit currents as a function of *nc*-ZnO thickness for PT devices. The normalized internal quantum efficiency (c) is relatively independent of *nc*-ZnO thickness. The normalized exciton generation rate (d) at the fixed *nc*-ZnO (d_3 = 20nm) is a strong function of the flash layer thickness.

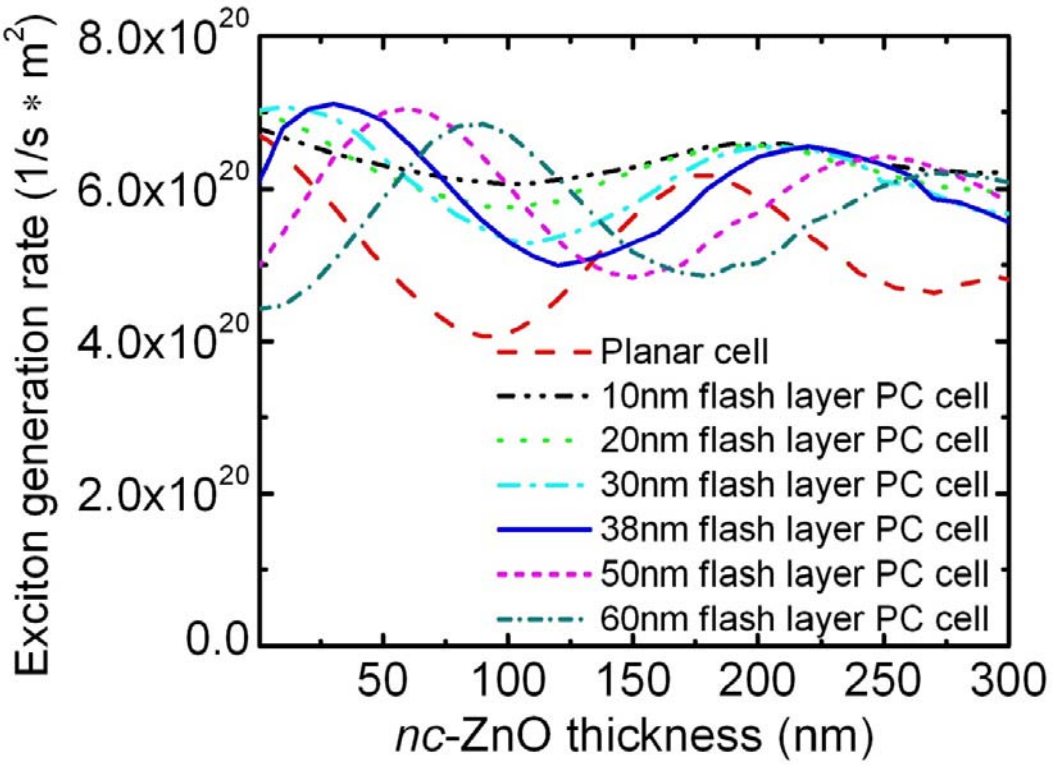

Figure 3.10. Extinction generation rates under variable flash layer thickness for PC cells.

layer is conductive enough not to hinder carrier transport. Also the layer's absorption spectra should not significantly overlap that of the photoactive layer.

3.3.8 Tandem PC cell

In this spirit, the PT-Cu structure with various *nc*-ZnO thickness was studied with a thin CuPC layer (13 nm) underneath the photoactive P3HT:PCBM layer in both PC and planar cells. The corresponding thickness of *nc*-ZnO in planar and patterned devices is summarized in Table 3.2. The CuPC layer protects against direct shorting between PEDOT:PSS and *nc*-ZnO in the PC cell including those PC cells with a thin flash layer of P3HT:PCBM. In summary, CuPC absorption in the IR as well as its electrical isolation property is advantageous for device performance.

Table 3.2. Thicknesses of *nc*-ZnO for PC and planar cells fabricated on four different device substrates

	nc-ZnO thickness (nm)	
device number	planar (d_1)	photonic crystal (d_2, d_3)
1	70	40, 90
2	90	50, 150
3	150	30, 180
4	165	50, 185

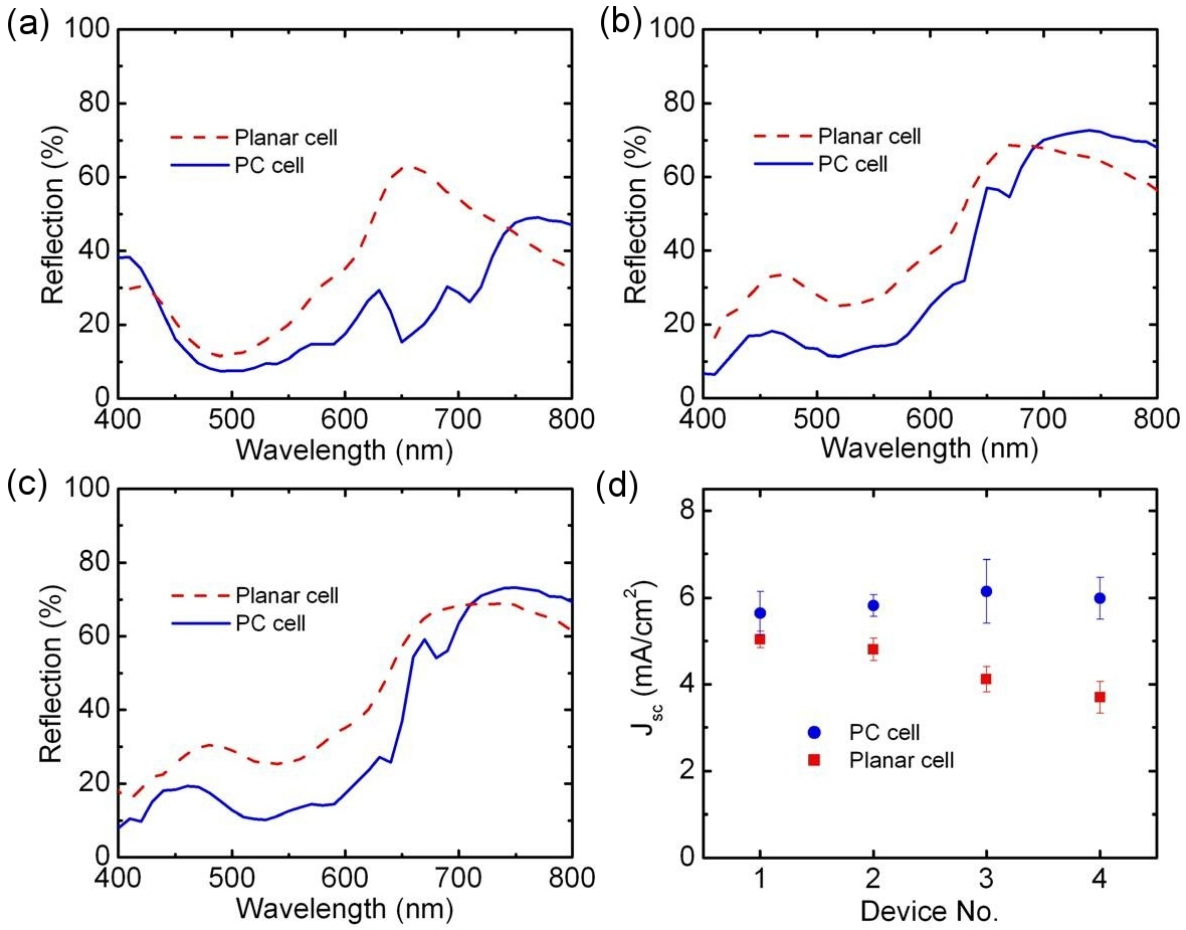

Figure 3.11. Reflection spectra of PC and planar cells for (a) No.1, (b) No.3, (c) No. 4 PT-Cu devices. Reflection spectrum of cell No.2 is shown separately in Figure 3.6b. (d) The short-circuit-current under 100mW/cm^2 for each device.

Figure 3.11 (a, b, c) shows reflection spectra for PC and planar cells indicating an enhanced absorption for all of the PC cells. This result was confirmed by the J_{sc} measurement where all PC cells, irrespective of *nc*-ZnO thickness, show significant improvements in J_{sc}. For example, for device No. 3, the J_{sc} for a PC cell was 6.2 mA/cm^2 whereas the planar cell on the same device exhibited a smaller J_{sc} (4.2 mA/cm^2). The absolute values of the observed J_{sc} are lower than in optimized P3HT:PCBM device[1, 26] without a CuPC layer. This could be due to both optical and electrical reasons associated with using a relatively thick CuPC layer: First, the overlap of the absorption spectra of a thick CuPC layer with that of P3HT:PCBM would reduce the incident photons which can be utilized in the P3HT:PCBM layer. Second, an exciton created in the thick CuPC layer cannot diffuse to the CuPC/P3HT:PCBM interface due to its short diffusion length. Thus, in our study, the thick CuPC layer (13 nm) may hamper device performance. Also, use of a relatively thin photoactive layer of P3HT:PCBM (80 nm) in our devices might reduce photocurrents. The influence of CuPC thickness in OPV devices was recently reported to show that optimization of the CuPC layer thickness with the P3HT:PCBM thickness is critical for high OPV performance.[21].

3.4 Conclusion

In conclusion, PRINT is a powerful method to simply fabricate accurate photonic crystals of large scale in a controlled way. Nanopatterns with different shapes, various pitch, and material flexibility provide the possibility to exploit the PC geometry in OPV devices. Contrasting refractive indices in the nanostructure in standard OPV and iOPV exhibit the photonic effect. The optical interference in PC cells was strongly affected by not only physical dimensions such as height and periodicity of the nanopatterned layer but also device

architecture. Herein we showed how the enhanced absorption through photonic effect could directly lead to the enhancement of device performance. We envision further improvements in the photonic crystal solar cell if the nano-pattern is optimized, and if we employ PV active materials that absorb more efficiently at the selected quasiguided modes in, for example, tandem cells.

3.5 References

(1). Li, G.; Shrotriya, V.; Huang, J.; Yao, Y.; Moriarty, T.; Emery, K.; Yang, Y. *Nature Mater.* **2005,** 4, 864.

(2). Li, G.; Shrotriya, V.; Yao, Y.; Yang, Y. *J. Appl. Phsys* **2005,** 98.

(3). Coakley, K. M.; McGehee, M. D. *Chem. Mater.* **2004,** 16, 4533.

(4). Duche, D.; Escoubas, L.; Simon, J.-J.; Torchio, P.; Vervisch, W.; Flory, F. *Appl. Phys. Lett.* **2008,** 92, 193310.

(5). Roman, L. S.; Inganäs, O.; Granlund, T.; Nyberg, T.; Svensson, M.; Andersson, M. R.; Hummelen, J. C. *Adv. Mater.* **2000,** 12, 189.

(6). Niggemann, M.; Glatthaar, M.; Gombert, A.; Hinsch, A.; Wittwer, V. *Thin Solid Films* **2004,** 451-452, 619.

(7). Cocoyer, C.; Rocha, L.; Sicot, L.; Geffroy, B.; de Bettignies, R.; Sentein, C.; Fiorini-Debuisschert, C.; Raimond, P. *Appl. Phys. Lett.* **2006,** 88, 133108.

(8). Na, S.-I.; Kim, S.-S.; Kwon, S.-S.; Jo, J.; Kim, J.; Lee, T.; Kim, D.-Y. *Appl. Phys. Lett.* **2007,** 91, 173509.

(9). Kim, M.-S.; Kim, J.-S.; Cho, J. C.; Shtein, M.; Guo, L. J.; Kim, J. *Appl. Phys. Lett.* **2007,** 90, 123113.

(10). Rolland, J. P.; Maynor, B. W.; Euliss, L. E.; Exner, A. E.; Denison, G. M.; DeSimone, J. M. *J. Am. Chem. Soc.* **2005,** 127, 10096.

(11). Hampton, M. J.; Williams, S. S.; Zhou, Z.; Nunes, J.; Ko, D.-H.; Templeton, J. L.; Samulski, E. T.; DeSimone, J. M. *Adv. Mater.* **2008,** 20, 2667.

(12). Ko, D.-H.; Tumbleston, J. R.; Zhang, L.; Williams, S.; DeSimone, J. M.; Lopez, R.; Samulski, E. T. *Nano Lett.* **2009,** 9, 2742.

(13). Ma, W.; Yang, C.; Heeger, A. J. *Adv. Mater.* **2007,** 19, 1387.

(14). Chen, L.-M.; Hong, Z.; Li, G.; Yang, Y. *Adv. Mater.* **2009,** 21, 1434.

(15). Bermel, P.; Luo, C.; Zeng, L.; Kimerling, L. C.; Joannopoulos, J. D. *Opt. Express* **2007,** 15.

(16). Kim, J. Y.; Kim, S. H.; Lee, H. H.; Lee, K.; Ma, W.; Gong, X.; Heeger, A. J. *Adv. Mater.* **2006,** 18, 572.

(17). Beek, W. J. E.; Wienk, M. M.; Kemerink, M.; Yang, X.; Janssen, R. A. J. *J. Phys. Chem. B* **2005,** 109, 9505.

(18). Hampton, M. J.; Williams, S. S.; Zhou, Z.; Nunes, J.; Ko, D.-H.; Templeton, J. L.; Samulski, E. T.; DeSimone, J. M. *Adv. Matr.s* **2008,** 20.

(19). Joannopoulos, J. D.; Meade, R. D.; Winn, J. N., *Photonic crystals: Molding the flow light* Princeton university press: New Jersey, 1995.

(20). Zhang, C.; Tong, S. W.; Jiang, C.; Kang, E. T.; Chan, D. S. H.; Zhu, C. *Appl. Phys. Lett.* **2008,** 92, 083310.

(21). Zhang, C.; Tong, S. W.; Jiang, C.; Kang, E. T.; Chan, D. S. H.; Zhu, C. *Appl. Phys. Lett.* **2008,** 93, 043307.

(22). Gippius, N. A.; Tikhodeev, S. G.; Ishihara, T. *Phys. Rev. B* **2005,** 72, 045138.

(23). Andreani, L. C.; Gerace, D. *Phys. Rev. B* **2006,** 73, 235114.

(24). Ferry, V. E.; Verschuuren, M. A.; Li, H. B. T.; Schropp, R. E. I.; Atwater, H. A.; Polman, A. *Appl. Phys. Lett.* **2009,** 95, 183503.

(25). Tumbleston, J. R.; Ko, D.-H.; Samulski, E. T.; Lopez, R. *Opt. Express* **2009,** 17, 7670.

(26). Ma, W.; Yang, C.; Gong, X.; Lee, K.; Heeger, A. J. *Adv. Funct. Mater.* **2005,**15,1617.

(27). Tumbleston, J. R.; Ko, D.-H.; Samulski, E. T.; Lopez, R. *Appl. Phys. Lett.* **2009,** 94, 043305.

(28). Gilot, J.; Barbu, I.; Wienk, M. M.; Janssen, R. A. J. *Appl. Phys. Lett.* **2007,** 91, 113520.

Chapter IV

SUPPRESION OF BIMOLECULAR RECOMBINATION BY UV-SENSITIVE ELECTRON TRANSFER LAYERS IN ORGANIC SOLAR CELLS

4.1 Introduction

A quickly evolving approach to enhancing the efficiency of bulk heterojunction (BHJ) organic solar cells involves the insertion of additional layers between the photoactive layer and the electrodes that enhance electrical or optical characteristics.[1-7] In particular, improving the absorption of light in the photoactive layer by inserting an optical spacer layer into the device architecture enables a straightforward gain in short-circuit current (J_{sc}). This phenomenon has been demonstrated experimentally[2, 5] and addressed theoretically[6, 8] using a well-understood optical model. On the other hand, insertion of additional layers for electrical enhancement often modifies J_{sc}, the fill factor (FF), and the open-circuit voltage (V_{oc}),[3-5, 9-13] making it difficult to decouple the fundamental physical processes involved. Even in cases where V_{oc} remains constant and the extra layer only improves J_{sc} and/or FF,[2, 14-18] the relationship between the electrical properties of the additional and photoactive layer remains unclear. Herein, we demonstrate that tuning the electrical properties of an electron transport layer (ETL) adjacent to the photoactive blend determines the values of J_{sc} and FF.

In metal-insulator-metal architectures of BHJ solar cells without additional layers, performance characteristics have been directly linked to microscopic device physics that controls the photogenerated current ($J_{photo} = J_{light} - J_{dark}$). These include the two fundamental electric field-dependent loss processes that can inhibit J_{sc} and FF, namely, exciton dissociation at the donor/acceptor interface and bimolecular recombination of charge carriers.[19-21] These processes have been elucidated to identify limitations of polymer/fullerene systems like P3HT (Poly(3-hexylthiophene)) : PCBM (Phenyl-C61-butyric acid methyl ester),[22, 23] but have not been analyzed in complex cell architectures with additional non-photoactive layers. On the other hand, macroscopic parameters of the traditional photovoltaic circuit model such as the device serial

resistance (R_{series}) can also dramatically alter J_{sc} and FF[24] where the additional layers may result in unwanted parasitic losses. In order to maximize the performance of organic photovoltaics, it is essential to understand the effects of these extra layers both in terms of the microscopic processes that affect the photocurrent and in the context of the macroscopic equivalent circuit interpretation. A comprehensive understanding is prerequisite for judiciously selecting cell architectures from this fast-growing approach to solar cell fabrication.

In this chapter, I explore inverted organic photovoltaic (iOPV)[25] solar cells with P3HT:PCBM as the photoactive layer. The ETL such as TiO_x,[14-16, 26, 27] TiO_2,[12, 28, 29] ZnO,[17, 30, 31] and Cs_2CO_3[11] for iOPV are necessary to operate the device by matching energy levels with the photoactive layer. In particular, the UV sensitivity of TiO_x has been studied and is known to affect iOPV device performance.[16, 26] However the relationship between the electrical properties of the ETL and the photoactive layer in the device is still elusive. We incorporate TiO_x as an ETL in an iOPV in order to exploit the temporal evolution of cell properties due to UV exposure. Our observations enable us to systematically track the variation of electrical properties associated with the ETL and the photoactive layer. We observe that after UV exposure, J_{sc} improves by two orders of magnitude while FF increases by a factor of three under solar simulated light. UV exposure does not alter the device optical performance, V_{oc}, or the P3HT:PCBM electrical properties. Hence, both the micro- and macroscopic electrical mechanisms that affect J_{sc} and FF upon insertion of an additional layer can be probed. Through the use of device modeling and light intensity experiments, we show that an increase in the resistivity of the ETL effectively turns on bimolecular recombination that is dominated by losses related to the diode current in P3HT:PCBM.

4.2 Experimental sections

4.2.1 TiO_2 sol-gel synthesis

TiO_2 sol-gel was prepared by previously reported method.[5] 10mL of titanium isopropoxide (Aldrich, 99.999%) precursor, 50mL of 2-methoxy methanol (Aldrich, ≥99.9%) and 5mL of ethanolamine (Aldrich, ≥99%) were mixed in argon gas condition. The solution was heated at 80°C for 2 hrs with vigorous stirring and subsequently heated at 120°C for 1hr. The heating steps were repeated. In order to get desired thickness of TiO_2 layer by spincasting, the solution was diluted with isopropyl alcohol.

4.2.2 Device fabrication

ITO-coated glass was cleaned with acetone, isopropyl alcohol and distilled water for 10 min each and then dried overnight in an oven (150˚C). The cleaned substrate was treated with UV Ozone for 20 min (UVO Cleaner 42, Jelight Company Inc.). The prepared TiO_2 sol-gel was spincasted on the ITO substrate and annealed at 150ºC for 1 hr in air to form an amorphous TiO_x film. For TiO_2 electron transporting layer, the spincasted film was annealed at 450 ºC for 30 min in air. The sample was then moved to an inert gas (purified nitrogen) glove box where a solution of P3HT (15mg mL-1) and PCBM (12mg mL-1) in chlorobenzene was spincoated on the TiO_x layer or TiO_2 layer and annealed at 150ºC for 30 min. Finally the device was transferred to a vacuum chamber (2e^-6 torr) and 8 nm WO_3 / 90 nm Ag was sequentially deposited on defined cell areas (12 mm^2).

4.2.3 Device measurement

Device performance was measured under 85 mW/cm^2 solar simulated light using a 400 nm UV cut-off filter. For UV illumination, the 365 nm UV source (UVP Model B 100 A with a 100 W Sylvania Model H44GS-100M bulb) was used. IPCE and light intensity (green laser) measurements were done in air, while all others were conducted in an inert glovebox. The properties of all devices are strongly dependent on UV illumination.[16, 26]

4.2.4 Electrical simulations

Electrical simulations are done using the computational platform, COMSOL Multiphysics incorporating the model outlined by Koster et. al.[32] The electron mobility (2.0e^-7 $m^2/V \cdot s$), dielectric constant (3.0e^-11 $C^2/N \cdot m^2$), effective density of states in the conduction and valence band of P3HT:PCBM (2.5e^25 m^{-3}), initial electron/hole separation distance (1.8 nm), and decay rate of bound electron/hole pairs (2.0e^4 s^{-1}) are taken from literature.[22, 33, 34] The energy gap between the HOMO of P3HT and LUMO of PCBM is taken to be 0.92 eV, slightly lower than used previously.[12] The hole mobility (1.5^e-8 $m^2/V \cdot s$) and generation rate of excitons (6.75e^27 $m^3 \cdot s$) are taken from results from this work. Each of these parameters remains unchanged for all simulations. Finally, the modified form of Langevin recombination is also used.[34]

4.3 Results and discussion

4.3.1 UV-sensitive performance of devices

Solar cells with two different thicknesses of the TiO_x ETL (50 and 25 nm) along with devices fabricated with a TiO_2 ETL (25 nm – annealed at 450º C for 30 min) were studied using

various UV exposure times (λ = 365 nm). The properties of all devices are strongly dependent on UV illumination.[16, 26] Even with the UV cut-off filter, performance changes in both TiO_x and TiO_2 iOPV devices are noted as shown in Figure 4.1. The device with TiO_2 as the ETL nearly saturates to a high performing device after 30 min illumination with solar simulated light using the UV cut-off filter. Equivalent illumination on a device with TiO_x as the ETL led to a near-zero starting efficiency. Thus, for all experiments this initial solar simulated illumination was performed prior to the first 30 min cycle of UV illumination with the λ = 365 nm source.

Figure 4.2 shows that the dark (J_{dark}) and light (J_{light}) current densities in TiO_x devices undergo considerable changes after 30 min time intervals of UV illumination.[16, 26] Clearly, the dark rectification, J_{sc}, and the FF are extremely poor prior to UV exposure leading to efficiencies well below 0.01%. Following consecutive UV illumination periods, performance steadily increases by more than two orders of magnitude and approaches saturation values. The UV response is somewhat sensitive to the TiO_x thickness as shown in Figure 4.2 where J_{sc}, V_{oc}, FF, and R_{series} are shown after each successive 30 min exposure to UV light. Longer exposure periods are needed to achieve saturation for thicker ETLs: J_{sc} is saturated after 60 min and 120 min for devices with 25 nm and 50 nm of TiO_x, respectively. The change is most dramatic in J_{sc}, which increases from 0.07 to 8.3 mA/cm^2 after a 120 min UV exposure (25 nm TiO_x device). The FF also improves from 15% to 51% yielding an efficiency of 2.8%. However, devices with TiO_2 as the ETL are relatively insensitive to even prolonged UV illumination where the efficiency is near its saturation value prior to UV exposure (see Figure 4.1).

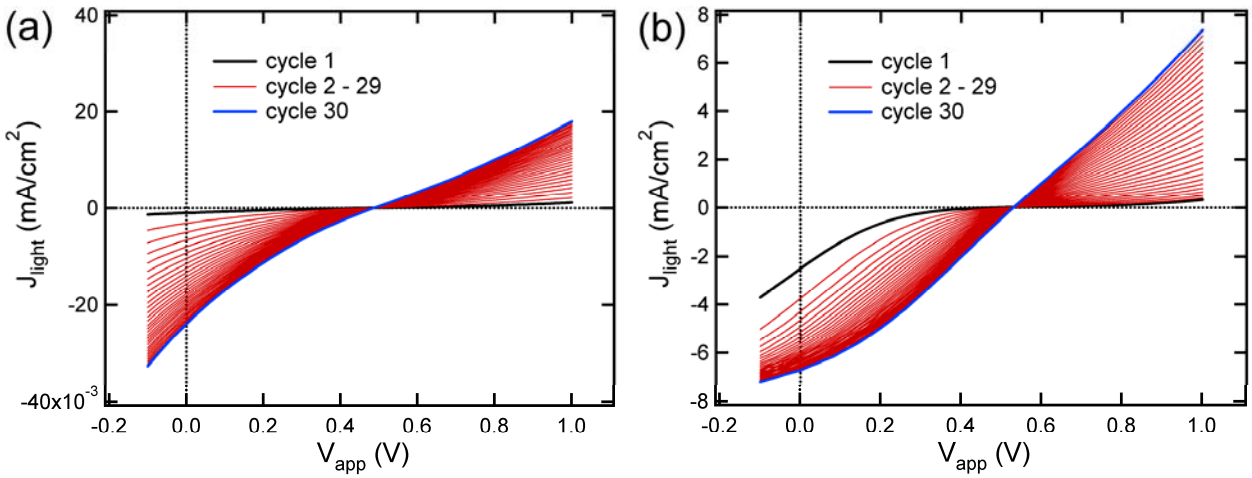

Figure 4.1. Illumination under 85 mW/cm^2 solar simulated sunlight using 400 nm cut-off filter for devices with (a) TiO_x and (b) TiO_2 as the ETL. Each cycle consists of the time required for a voltage scan (~1 min).

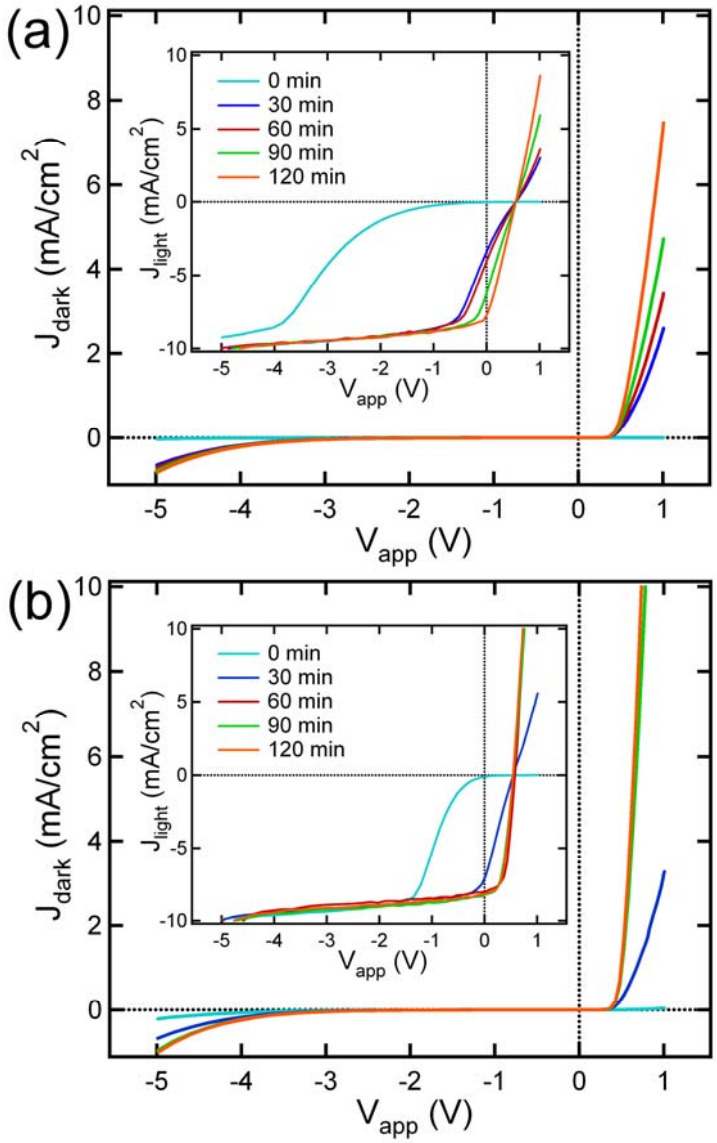

Figure 4.2. Dark current and light current (inset) densities for iOPV devices with (a) 50 nm and (b) 25 nm TiO_x electron transporting layers under solar simulated light (with a UV cut-off filter) after successive 30 min UV (λ = 365 nm) exposure times.

In spite of the dramatic changes observed in J_{sc} and FF, Figure 4.3 also indicates that V_{oc} remains constant after each cycle of UV illumination. Furthermore, R_{series} (defined as the inverse slope of the current-voltage curves at V_{oc}) undergoes a dramatic reduction of three orders of magnitude for devices with TiO_x as the ETL. On the contrary, devices with TiO_2 as the ETL are relatively insensitive to prolonged UV illumination as shown in Figure 4.4.

Commonly, a modification in R_{series} with constant V_{oc} is given as the primary reason for altered performance characteristics caused by the insertion of additional non-photoactive layers.[3, 4, 10] However, this view does not specify the origin of the performance change.

4.3.2 UV illumination effect on the properties of the photoactive layer (P3HT:PCBM)

Standard organic photovoltaic cells were fabricated with ITO (150 nm) / PEDOT:PSS (40 nm) / P3HT:PCBM (100 nm) / Al (100 nm). For the photoactive layer, a solution containing P3HT (15 $mg \cdot mL^{-1}$) and PCBM (12 $mg \cdot mL^{-1}$) in chlorobenzene was spincoated onto the PEDOT:PSS coated substrate. The device was annealed at 150° C for 30 min before measurement under 85 mW/cm^2 solar simulated light using a 400 nm UV cut-off filter. As shown in Figure 4.5, the properties of the standard device are unaffected by UV illumination compared to inverted organic photovoltaic (iOPV) cells. The constant hole mobility of P3HT:PCBM with UV illumination is also shown in Figure 4.5. The hole-only P3HT:PCBM devices (Pd / P3HT:PCBM / PEDOT:PSS / ITO) was prepared by the previously reported method[35] and measured after annealing at 150° C for 30 min in a nitrogen glove box. The hole mobility of P3HT:PCBM measured to be 1.5e-8 $m^2/V \cdot s$ and constant with UV illumination. Both experiments confirm that UV illumination does not significantly alter the properties of the photoactive layer.

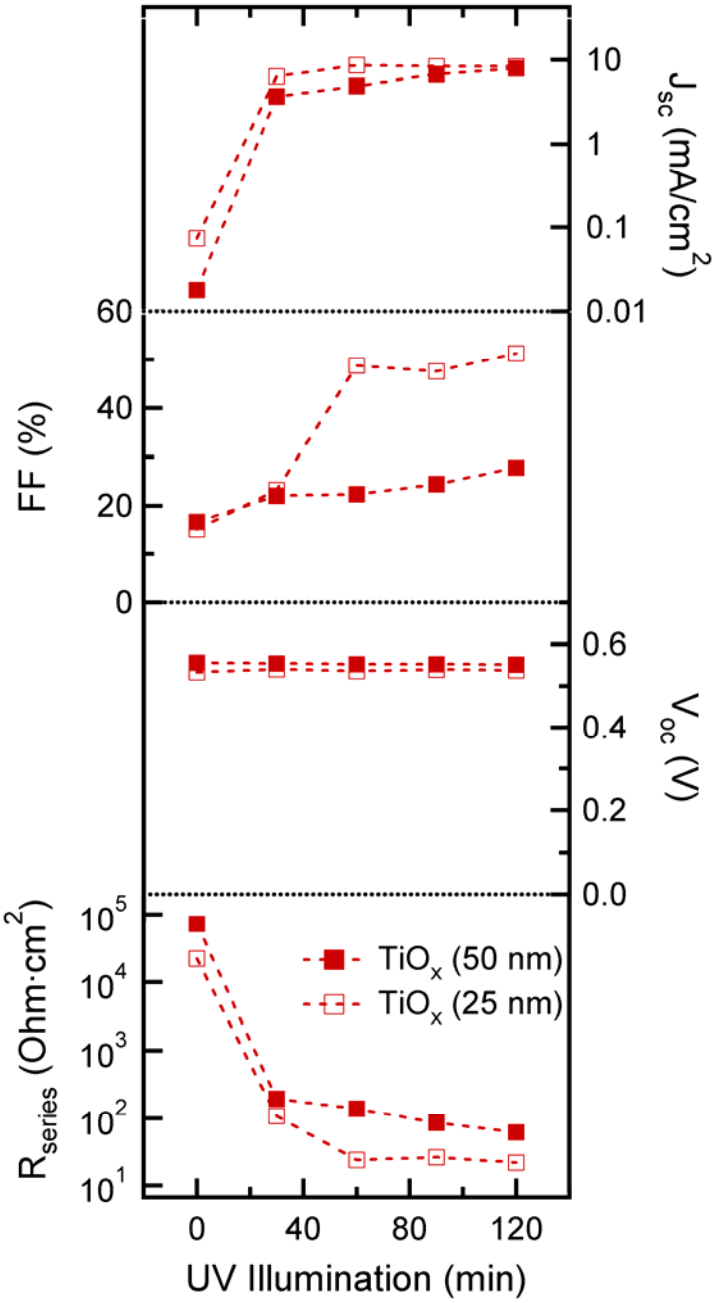

Figure 4.3. Short-circuit current (J_{sc}), fill factor (FF), open-circuit voltage (V_{oc}), and series resistance (R_{series}) of devices with TiO_x as the ETL after successive 30 min intervals of UV exposure.

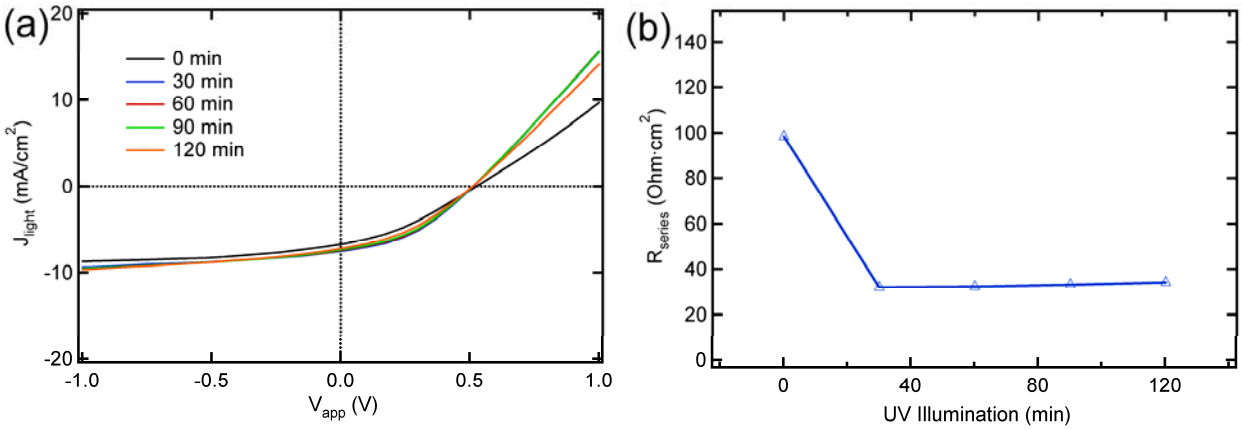

Figure 4.4. (a) Device performance and (b) corresponding series resistance of device with TiO_2 as the ETL after successive exposures to UV illumination.

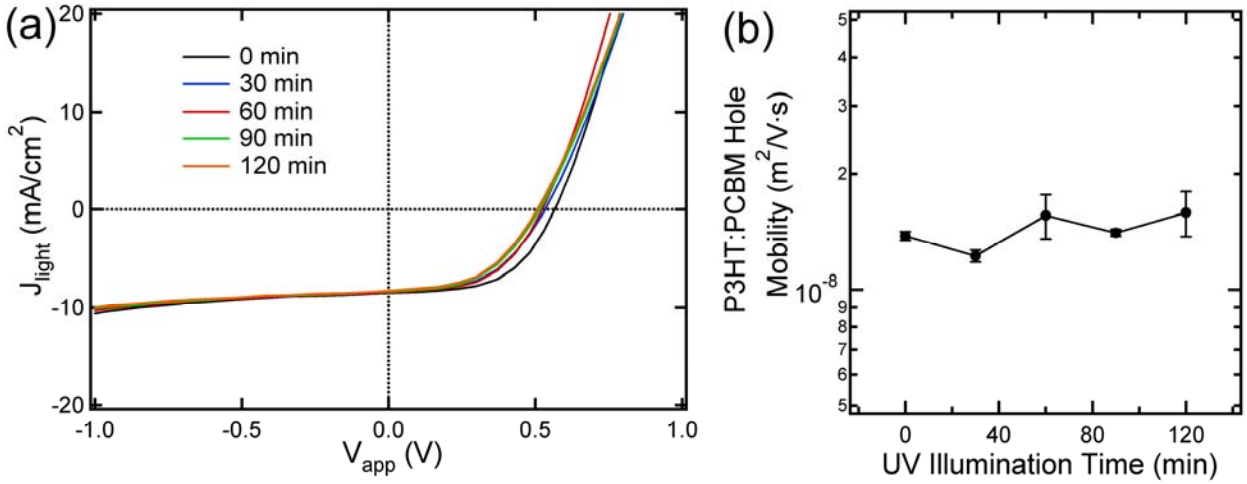

Figure 4.5. (a) Standard P3HT:PCBM device and (b) P3HT:PCBM hole mobility after successive cycles of UV illumination. The properties of the standard device are unaffected by UV illumination compared to inverted organic photovoltaic (iOPV) cells, and the constant hole mobility of P3HT:PCBM with UV illumination is also observed.

4.3.3 UV illumination effect on the interface between TiO_x and P3HT:PCBM

The P3HT:PCBM and TiO_x interfaces was modified by the previously reported method. [29, 36] The interface was tuned with *p*-amino benzoic acids (p-AB) and *p*-nitro benzoic acid (p-NB), which have opposite dipole moment directions[37]. In Figure 4.6, the J_{sc} dramatically changes with UV illumination, while J_{sat} values are close to the unmodified devices and remains constant. Other properties (V_{oc}, FF, R_{series} etc, not shown in the chapter) showed similar trends as the unmodified devices under UV illumination.

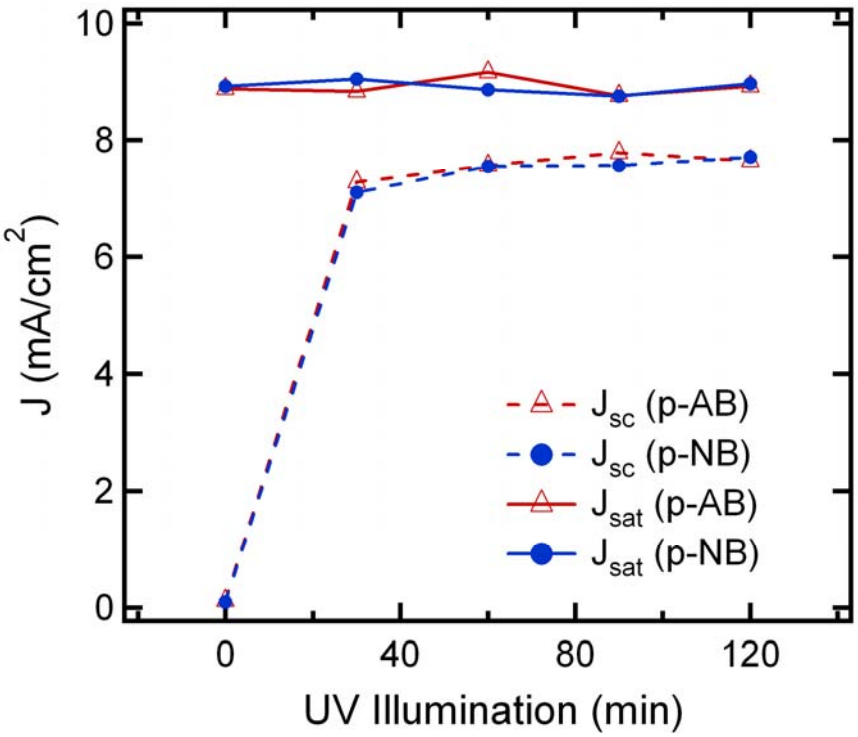

Figure 4.6 Saturated photocurrent (J_{sat}) and short-circuit current (J_{sc}) for devices with TiO_x as the ETL fabricated with two different materials with opposite dipole moment polarity (*p*-amino benzoic acid (p-AB) and *p*-nitro benzoic acid (p-NB)) at the TiO_x/P3HT:PCBM interface.

4.3.4 UV illumination effect on photon absorption property

We provide an in-depth explanation based on fundamental optical and electrical processes associated with the iOPV device. First, we turn our attention to photon absorption. Improvements in J_{sc} are frequently a result of increased light absorption due to a more favorable optical interference profile in the photoactive layer.[15, 17] As shown in Figure 4.2, at high reverse bias where electric field-dependent losses are minimized, J_{light} is constant for all devices and is consequently controlled by light absorption.[38, 39] In Figure 4.2, the experimental photocurrent density at high reverse bias ($J_{exp.\ photo} = J_{light} - J_{dark}$) approaches a saturation value ($J_{sat} \sim 9.8$ mA/cm^2 ; inset of Figure 4.7)); J_{sat} is constant for each device type and for all UV exposure times.

From these values, the generation rate of bound electron/hole pairs, G, is determined via $J_{sat} = q \cdot G \cdot L$, where q is the elementary charge and L is the active layer thickness.[38, 39] An average value of $G = 6.75 \times 10^{27}$ m$^{-3} \cdot$s^{-1} is obtained for all devices (Figure 4.7) consistent with previously reported values for P3HT:PCBM.[33] This result was checked by measuring the spectral reflection for each device and fitting it to an optical model (see section 4.3.3).[40] A calculation of G values follows directly,[41] and the agreement between the two ways of determining G is shown in Figure 4.7. This result supports the perspective that both the ETL material choice and the period of UV exposure have a negligible effect on photon absorption in the photoactive layer.[15, 42] Furthermore, measurements of standard devices (Al / P3HT:PCBM / PEDOT:PSS / ITO) and hole-only P3HT:PCBM devices (Pd / P3HT:PCBM / PEDOT:PSS / ITO)[22] under UV illumination in Figure 4.5 confirm that UV light at these levels does not significantly alter the electrical properties of P3HT:PCBM. These observations imply that UV illumination only directly influences the bulk electrical properties of the titanium oxide ETL.

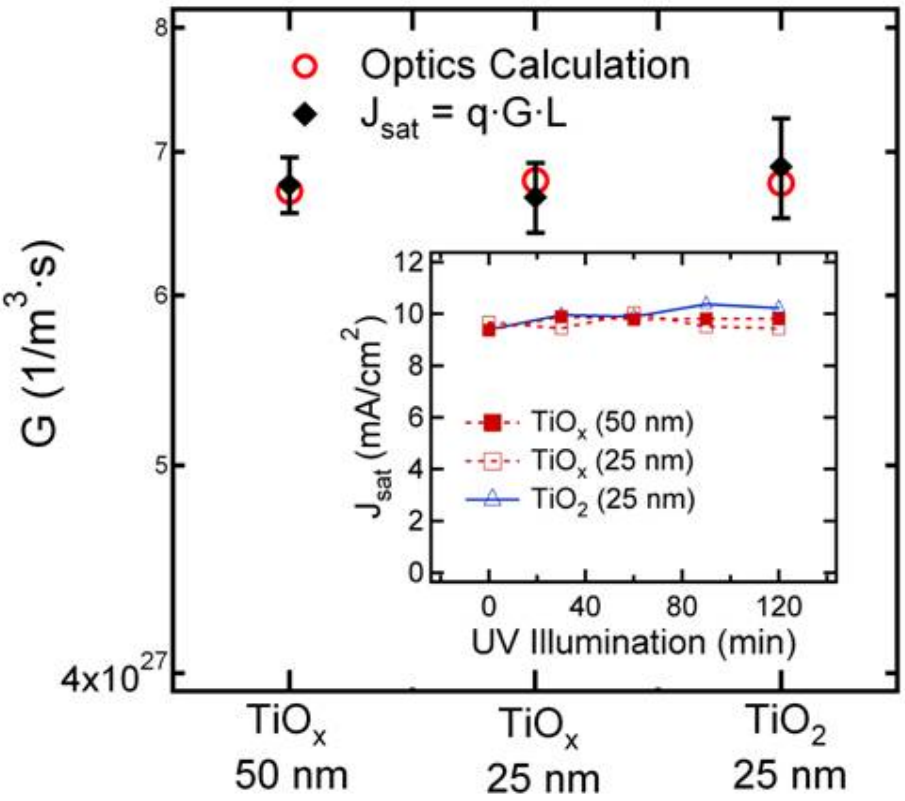

Figure 4.7. Exciton generation rate, G, determined from both the saturated photocurrent J_{sat} (inset) and a separate optical reflection measurement/calculation.

4.3.5 Exciton creation rate optical calculation

Determination of the generation rate of excitons in the photoactive layer, G, is simply done by measuring the saturated photocurrent (J_{sat}) and using the equation, $J_{sat} = q \cdot G \cdot L$ as described in the manuscript where q is the elementary charge and L is the photoactive layer thickness. A determination of G is also done via an optical measurement and calculation. First, zeroth order reflection is measured in s-polarization under an incident angle of 15º. This is shown in Figure 4.8a for the device with thicker TiO_x as the ETL. The optical properties of each material, as given in Figure 4.8b-c, are incorporated into an optical simulation program[43] to fit for the thicknesses of each cell material[40]. The optical properties were measured using spectroscopic ellipsometry, except for the properties of the silver electrode that are taken from literature.[44] Finally, the optical model is used to determine the absorption of light in the photoactive layer, so G can be calculated using the standard AM 1.5 solar spectrum.

4.3.6 UV illumination effect on electrical properties of the ETL

The electrical properties of the ETL layer are characterized by measuring the dark resistivity after varying the UV illumination time for isolated layers in sandwich devices of ITO / TiO_x or TiO_2 / Al with the same dimensions as the iOPV devices. As shown in Figure 4.9, TiO_x resistivity decreases by an order of magnitude (from 1.0×10^7 to 1.2×10^6 Ohm·cm) for $V_{app} = 0$ V, and approaches the resistivity of TiO_2 (which is almost unaffected by UV illumination).

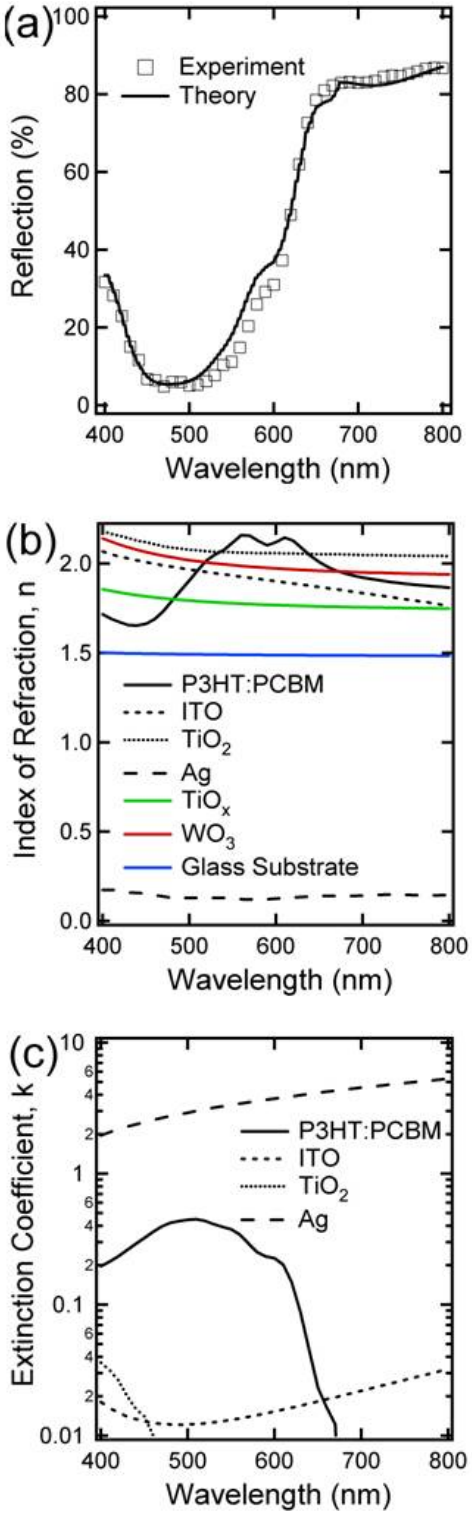

Figure 4.8. (a) Experimental and simulated s-polarized reflection of device with thicker TiO_x ETL. Optical properties of all constituent cell materials where (b) is the index of refraction and (c) is the extinction coefficient. The extinction coefficients of TiO_x, WO_3, and the glass substrate are taken to be zero over the measured spectral range.

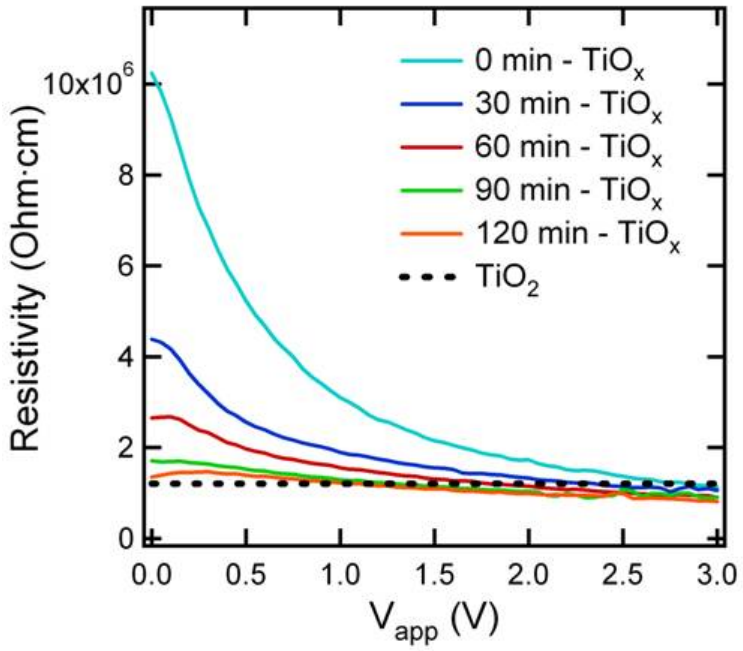

Figure 4.9. Dark resistivity of TiO_x versus UV illumination. The resistivity of TiO_2 changes insignificantly relative to TiO_x.

4.3.7 Electrochemical mechanism of TiO_x

For simple metal-oxide diodes, changes in resistivity under both UV illumination and positive bias application have been attributed to an electrochemical mechanism[26, 45, 46] that involves the filling of negatively charged oxygen traps in the metal-oxide. The injection of free electrons and holes under forward bias and the creation of electron/hole pairs during UV illumination separately result in a free electron left behind in the conduction band of the ETL causing an increase in the conductivity. Indeed, we observed that holding the device under positive bias for specified time intervals in the dark has the same effect on device performance as UV illumination. Figure 4.10 shows J_{sc} under solar simulated light after 30 minute applications of bias voltage in the dark. A considerable increase is noted for positive bias only that resembles the effect of UV illumination as presented in the manuscript. Conductivity increases in metal-oxide diodes under both UV illumination and positive bias application have been attributed to an electrochemical mechanism.[46, 47] This involves the elimination of negatively charged oxygen traps in the metal-oxide either by the injection of free electrons and holes under forward bias or by the creation of electron/hole pairs under UV illumination. In both cases, the free electrons left behind in the conduction band after neutralization of the negative trap by the free hole increases the conductivity. Neutralization of the negative trap leads to oxygen release from the oxide layer. Changes are not noted for reverse bias due to the large energy barriers for injection of electrons and holes.

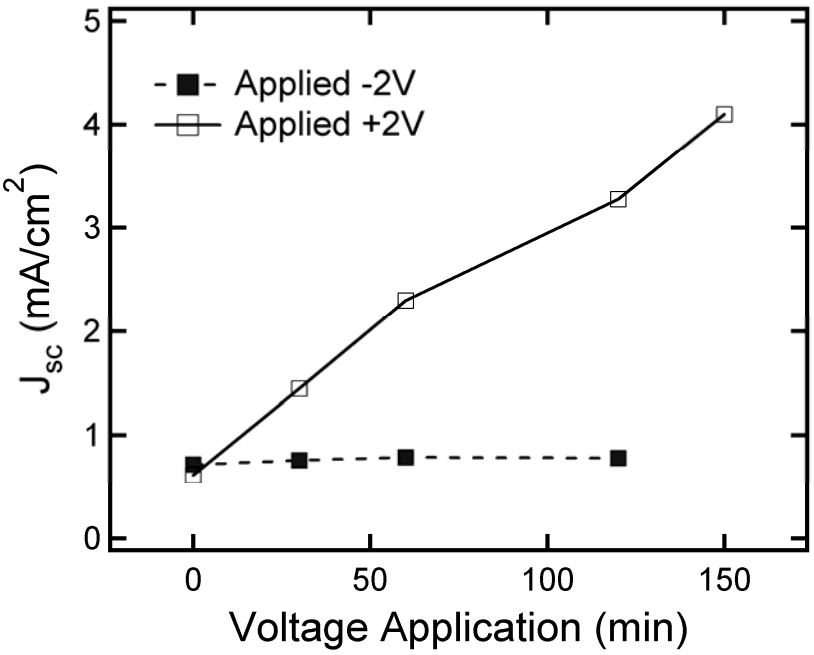

Figure 4.10. J_{sc} for device with TiO_x as the ETL where bias voltage with opposite polarity is applied instead of UV illumination. A change similar to that with UV illumination is observed only under forward bias of +2 V.

4.3.8 Electrical models for the OPV

In order to understand how a resistivity change confined to the ETL influences the physical processes in the photoactive layer, we first consider a model for standard organic BHJ solar cells that includes drift and diffusion of photogenerated carriers under the influence of bimolecular recombination that undergo a field-dependent dissociation at the donor/acceptor interface.[32] The measured changes in an isolated TiO_x or TiO_2 layer's resistivity (sandwich devices of ITO / TiO_x or TiO_2 / Al; see Figure 4.9), in conjunction with the photoactive material's UV-independence, imply that UV exposure only affects the electrical transport properties of the ETL. Furthermore, the device V_{oc} remains constant under UV illumination indicating that the ETL energy levels are unaffected.[42] Thus, the UV effect is modeled as a change in the effective potential difference across the photoactive layer leading to a weakening of the internal electric field. The potential boundary conditions are modified to include an ohmic voltage drop that is the product of the extracted current and a resistor. In this way, a UV-dependent serial resistance is incorporated into the model and used as a fitting parameter to approximate the current-voltage data in the first and forth quadrants. Series resistance values fall within 20% of the measured values in Figure 4.3. Other model parameters describing P3HT:PCBM are taken as constant including the exciton generation rate (Figure 4.7), carrier mobilities, dielectric constant, and built-in voltage.[33] The model simulations are shown in Figure 4.11(a) where the trends of Figure 4.3 for V_{oc}, J_{sc}, and FF are reproduced. The model is then used to calculate the spatially averaged percentage of photogenerated free carriers that undergo bimolecular recombination ($<BR_{photo}>$) for each UV illumination time. These results are shown in Figure 4.11(b) where it is observed that

longer UV exposure times leads to an increased internal electric field and reduced bimolecular recombination.

At first glance it appears that recombination of photogenerated carriers is the primary cause of the reduced current output. However, its relative importance may be probed by setting $<BR_{photo}> = 0$ for all applied voltages. Interestingly, this recombination pathway has little effect on the extracted current as shown in Figure 4.11(a) for 30 min UV exposures. The current at short-circuit is modified by less than 8%. This result is primarily due to the fact that recombined carriers first form a bound electron-hole pair before decaying to the ground state, which has some probability of dissociation back into free charges.[33] The probability of exciton dissociation is near 90% at short-circuit for standard P3HT:PCBM devices meaning that most of the free carriers that recombine will again dissociate back to free carriers making this a minimal loss process.[22] Furthermore, we do not attribute UV-dependent current losses to exciton dissociation due to its weak dependence on the internal electric field[22] and demonstrated negligible loss for P3HT:PCBM solar cells near open-circuit conditions.[48]

The relative unimportance of these loss mechanisms on the photocurrent indicates that J_{photo} may be approximated as constant for all applied voltages. A simple replacement circuit model may then be used as is frequently done with BHJ devices, especially P3HT:PCBM:[49-51]

$$J = J_o\left[\exp\left(\frac{e\left(V_{app} - JR_{series}\right)}{nk_BT}\right) - 1\right] + \frac{\left(V_{app} - JR_{series}\right)}{R_{shunt}} - J_{photo} \tag{4.1}$$

where J_0 is the reverse saturation current, e is the elementary charge, n is the diode ideality factor, k_B is Boltzmann's constant, T is the temperature, V_{app} is the applied voltage, R_{shunt} is the shunt resistance, R_{series} is the series resistance, J is the current density, and J_{photo} is

the photogenerated current that is constant with applied voltage. The first term on the right-hand side constitutes J_{diode}.

As with the drift-diffusion model, fits to the experimental current-voltage curves in the 1st and 4th quadrants are obtained by varying R_{series}. These curves show negligible deviations from the drift-diffusion model of Figure 4.11(a) and are not shown. Other model parameters including the reverse saturation current ($J_o = 2.0x10^{-4}$ mA/cm^2) and diode ideality factor (n = 2.0)[52] that describe the diode current (J_{diode}), shunt resistance ($R_{shunt} = 5.0x10^5$ ohm·cm^2), and photogenerated current (J_{photo} = 8.5 mA/cm^2) remain unchanged in each simulation. The case where R_{series} = 0 ohm·cm^2 is also displayed showing that further reduction would primarily result in a higher FF. The primary utility of this model is the calculation of J_{diode}, so that a comparison can be made with J_{photo}. In the power generating regime of the current-voltage curve (i.e. 4th quadrant), high levels of J_{diode} will cause a reduction in current in the external circuit. For example, the ratio J_{diode} / J_{photo} is unity at V_{oc}. Recently, J_{diode} has been microscopically understood to be a bimolecular recombination process that resembles BR_{photo} described above for the drift-diffusion model, but is related to the inherent diode function instead of the photogenerated current.[48, 52] Therefore, we interpret J_{diode} as a bimolecular recombination process (BR_{diode}) that is separate from BR_{photo}. The ratio J_{diode} / J_{photo} is given in Figure 4.4(c) where the effect of high values for R_{series} can be quickly understood. For each UV exposure time, this ratio is unity at V_{oc} where all J_{photo} "flows" through the diode and recombines. Likewise, for no (0 min) UV illumination where R_{series} >> 0, the ratio is close to unity over the entire forward bias range. As the device is illuminated with UV light, the series resistance decreases along with the ratio J_{diode} / J_{photo}. Ultimately this causes a reduction in BR_{diode}.

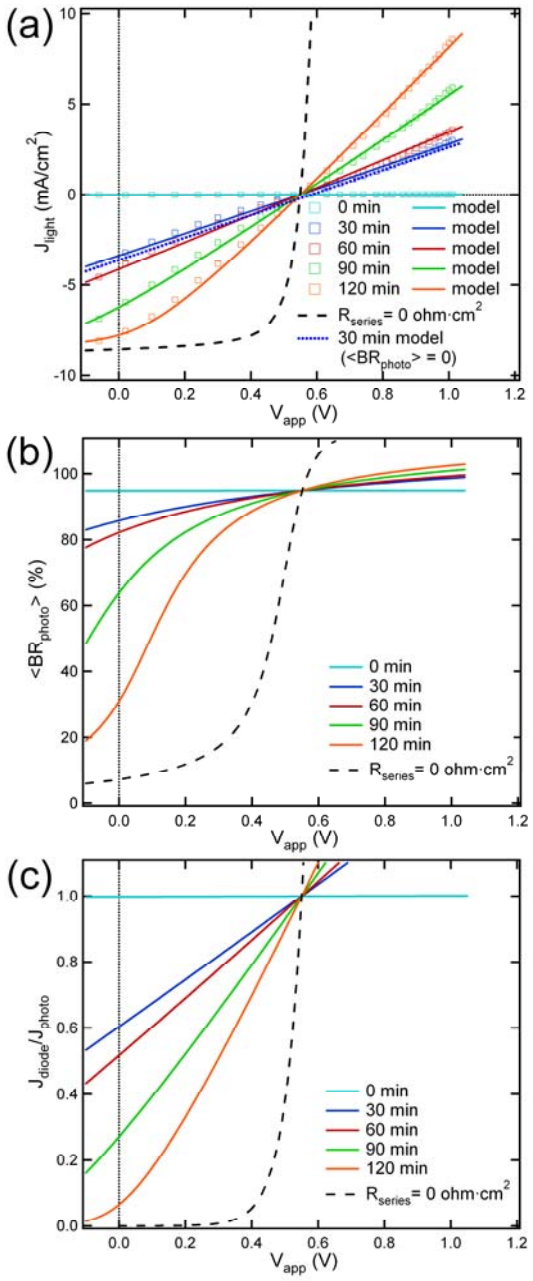

Figure. 4.11. (a) Experimental and simulated light current density (J_{light}) for each cycle of UV illumination. The importance of bimolecular recombination in the photocurrent is shown by setting <BR_{photo}> = 0 for 30 min UV illumination. (b) Calculated spatial average of BR_{photo} as a function of V_{app} for each UV illumination cycle, which gives the fraction of free carriers that recombine via this loss process. (c) The ratio of J_{diode} to J_{photo} given by the equivalent circuit model. All panels show the results for an ideal P3HT:PCBM device where R_{series} = 0 ohm·cm^2.

4.3.9 Light intensity dependence of the OPV performance

The significance of BR_{photo} in limiting J_{photo} can be probed by measuring J_{sc} over a range of light intensities where a non-linear dependence signals the prevalence of this process.[22, 53, 54] When measuring a device with high serial resistance, this tendency is also expected from the circuit model. Due to the UV-controlled series resistance observed here, the relationship between J_{sc} and light intensity should become increasingly linear for prolonged UV illumination. This prediction is observed as shown in Figure 4.12(a) where J_{sc} is given as a function of light intensity under $\lambda = 532$ nm laser illumination. The data are fit to the circuit model by varying only R_{series} using the same diode and shunt parameters as in Figure 4.11. Sub-linear behavior is observed beginning below 1 mW/cm^2 for the 30 min UV illuminated device, and at higher intensity (above 1 mW/cm^2) for the device where the performance becomes UV saturated (~120 min). By assuming $J_{sc} \propto I^{\alpha}$ where I is the light intensity, we find by fitting the power law between 10 and 100 mW/cm^2, that α takes respective values of 0.38 and 0.73 for 30 min and 120 min of UV illumination. As with the current-voltage data, the ratio J_{diode} / J_{photo} (Figure 4.12(b)) demonstrates the relative impact of BR_{diode} for each UV illumination time. Regardless of UV exposure, J_{sc} is increasingly affected by diode losses under higher light intensity. Furthermore, exposure to UV effectively determines the intensity where losses in the diode become significant. It follows that these are nearly the same light intensities where non-linearity in the extracted current begins.

Light intensity measurements prior to UV illumination are not shown due to the high measurement variability from extremely low currents. Therefore, the incident photon to current conversion efficiency (IPCE) measured with a lock-in amplifier is shown in Figure

4.12(c). The IPCE involves intensities near 0.05 mW/cm^2 where the effect of the diode current will be weak relative to higher light intensities. Integration of IPCE to calculate J_{sc}[2, 55] gives values of 3.5 and 7.6 mA/cm^2 for the device prior to UV illumination and after 120 min UV exposure, respectively. By contrast, J_{sc} < 0.1 mA/cm^2 prior to UV illumination as measured under solar simulated light (Figure 4.3). The gross overestimation of the predicted J_{sc} from the IPCE measurement results from the dominance of BR_{diode} near 1 sun conditions where the current does not scale linearly with light intensity. We can now conclude that the electrical properties of the TiO_x ETL effectively determines bimolecular recombination as quantified by diode losses in P3HT:PCBM. Prior to UV illumination, the high layer resistivity drives more photogenerated current through the diode, which in turn, leads to extremely high levels of recombination mimicking device operation at open-circuit. Prolonged UV exposure reduces the ETL resistivity, which lowers the serial resistance resulting in reduced recombination losses.

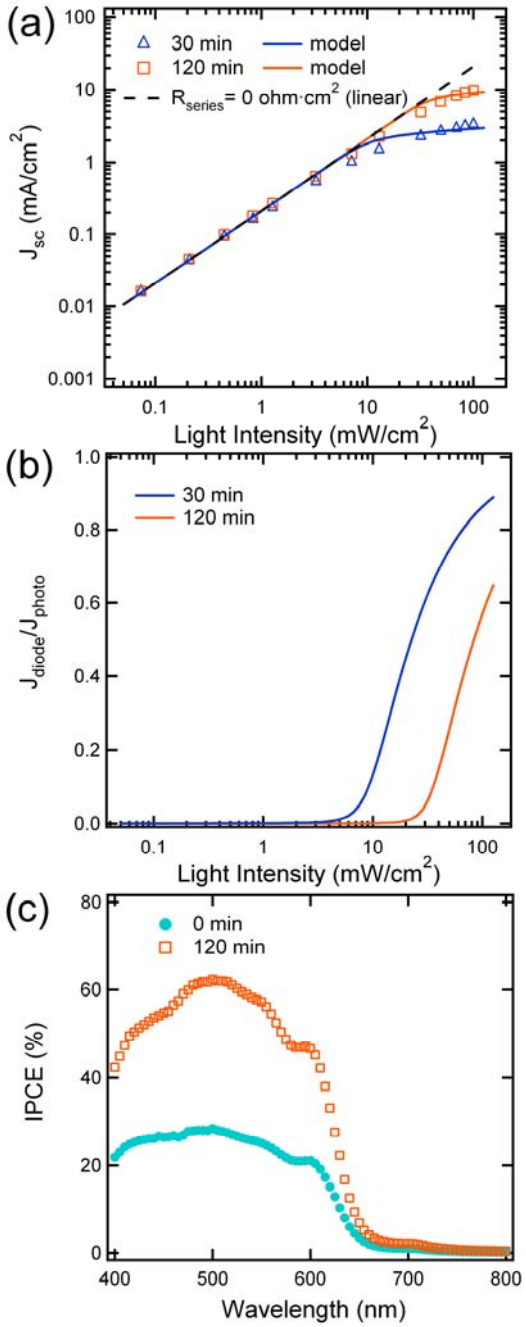

Figure. 4.12. (a) J_{sc} as a function of $\lambda = 532$ nm laser light intensity for a device with TiO_x as the ETL after 30 min and 120 min UV exposure. The prediction from the circuit model is also given for each UV illumination time along with the linear dependence for $R_{series} = 0$ ohm·cm^2. (b) Model calculation of the ratio J_{diode} / J_{photo} for each illumination time. (c) Incident photon to current conversion efficiency (IPCE) prior to UV illumination and after UV saturation where the incident light intensity is ~0.05 mW/cm^2.

4.4 Conclusion

In this chapter, I have shown that the electrical properties of non-photoactive layers significantly affect physical processes in the BHJ material. Improvements in J_{sc} that span two orders of magnitude originate from a resistivity drop in the electron transporting layer induced by UV illumination. The resistivity has a profound effect on serial resistance, which effectively controls bimolecular recombination attributed to the diode current.

4.5 References

(1). Kim, J. Y.; Lee, K.; Coates, N. E.; Moses, D.; Nguyen, T.-Q.; Dante, M.; Heeger, A. J. *Science* **2007,** 317, 222.

(2). Park, S. H.; Roy, A.; Beaupre, S.; Cho, S.; Coates, N.; Moon, J. S.; Moses, D.; Leclerc, M.; Lee, K.; Heeger, A. J. *Nature Photon.* **2009,** 3, 297.

(3). Chaudhary, S.; Lu, H.; Muller, A. M.; Bardeen, C. J.; Ozkan, M. *Nano Lett.* **2007,** 7, 1973.

(4). Irwin, M. D.; Buchholz, D. B.; Hains, A. W.; Chang, R. P. H.; Marks, T. J. *Proc. Natl. Acad. Sci. USA* **2008,** 105, 2783.

(5). Kim, J. Y.; Kim, S. H.; Lee, H. H.; Lee, K.; Ma, W.; Gong, X.; Heeger, A. J. *Adv. Mater.* **2006,** 18, 572.

(6). Gilot, J.; Barbu, I.; Wienk, M. M.; Janssen, R. A. J. *Appl. Phys. Lett.* **2007,** 91, 113520.

(7). Yip, H.-L.; Hau, S. K.; Baek, N. S.; Ma, H.; Jen, A. K. Y. *Adv. Mater.* **2008,** 20, 2376.

(8). Andersson, B. V.; Huang, D. M.; Moule, A. J.; Inganas, O. *Appl. Phys. Lett.* **2009,** 94, 043302.

(9). Park, M.-H.; Li, J.-H.; Kumar, A.; Li, G.; Yang, Y. *Adv. Funct. Mater.* **2009,** 19, 1241.

(10). Tao, C.; Ruan, S.; Zhang, X.; Xie, G.; Shen, L.; Kong, X.; Dong, W.; Liu, C.; Chen, W. *Appl. Phys. Lett.* **2008,** 93, 193307.

(11). Li, G.; Chu, C. W.; Shrotriya, V.; Huang, J.; Yang, Y. *Appl. Phys. Lett.* **2006,** 88, 253503.

(12). Tao, C.; Ruan, S.; Xie, G.; Kong, X.; Shen, L.; Meng, F.; Liu, C.; Zhang, X.; Dong, W.; Chen, W. *Appl. Phys. Lett.* **2009,** 94, 043311.

(13). Shrotriya, V.; Li, G.; Yao, Y.; Chu, C.-W.; Yang, Y. *Appl. Phys. Lett.* **2006,** 88, 073508.

(14). Waldauf, C.; Morana, M.; Denk, P.; Schilinsky, P.; Coakley, K.; Choulis, S. A.; Brabec, C. J. *Appl. Phys. Lett.* **2006,** 89, 233517.

(15). Ameri, T.; Dennler, G.; Waldauf, C.; Denk, P.; Forberich, K.; Scharber, M. C.; Brabec, C. J.; Hingerl, K. *J. Appl. Phys.* **2008,** 103, 084506.

(16). Steim, R.; Choulis, S. A.; Schilinsky, P.; Brabec, C. J. *Appl. Phys. Lett.* **2008,** 92, 093303.

(17). Kyaw, A. K. K.; Sun, X. W.; Jiang, C. Y.; Lo, G. Q.; Zhao, D. W.; Kwong, D. L. *Appl. Phys. Lett.* **2008,** 93, 221107.

(18). Tsai, H.-W.; Pei, Z.; Chan, Y.-J. *Appl. Phys. Lett.* **2008,** 93, 073310.

(19). Blom, P. W. M.; Mihailetchi, V. D.; Koster, L. J. A.; Markov, D. E. *Adv. Mater.* **2007,** 19, 1551.

(20). Marsh, R. A.; McNeill, C. R.; Abrusci, A.; Campbell, A. R.; Friend, R. H. *Nano Lett.* **2008,** 8, 1393.

(21). Gonzalez-Rabade, A.; Morteani, A. C.; Friend, R. H. *Adv. Mater.* **2009,** 21, 3924.

(22). Mihailetchi, V. D.; Xie, H. X.; de Boer, B.; Koster, L. J. A.; Blom, P. W. M. *Adv. Funct. Mater.* **2006,** 16, 699.

(23). Häusermann, R.; Knapp, E.; Moos, M.; Reinke, N. A.; Flatz, T.; Ruhstaller, B. *Journal of Applied Physics* **2009,** 106.

(24). Servaites, J. D.; Yeganeh, S.; Marks, T. J.; Ratner, M. A. *Adv. Funct. Mater.* **2010,** 20, 97.

(25). Chen, L.-M.; Hong, Z.; Li, G.; Yang, Y. *Adv. Mater.* **2009,** 21, 1434.

(26). Kuwabara, T.; Nakayama, T.; Uozumi, K.; Yamaguchi, T.; Takahashi, K. *Sol. Eng. Mater. Sol. Cells* **2008,** 92, 1476.

(27). Kim, C. S.; Lee, S. S.; Gomez, E. D.; Kim, J. B.; Loo, Y.-L. *Appl. Phys. Lett.* **2009,** 94, 113302.

(28). Li, C.-Y.; Wen, T.-C.; Lee, T.-H.; Guo, T.-F.; Huang, J.-C.-A.; Lin, Y.-C.; Hsu, Y.-J. *J. Mater. Chem.* **2009,** 19, 1643.

(29). Hau, S. K.; Yip, H.-L.; Acton, O.; Baek, N. S.; Ma, H.; Jen, A. K. Y. *J. Mater. Chem.* **2008,** 18, 5113.

(30). Hau, S. K.; Yip, H.-L.; Baek, N. S.; Zou, J.; O'Malley, K.; Jen, A. K. Y. *Appl. Phys. Lett.* **2008,** 92, 253301.

(31). White, M. S.; Olson, D. C.; Shaheen, S. E.; Kopidakis, N.; Ginley, D. S. *Appl. Phys. Lett.* **2006,** 89, 143517.

(32). Koster, L. J. A.; Smits, E. C. P.; Mihailetchi, V. D.; Blom, P. W. M. *Phys. Rev. B* **2005,** 72, 085205.

(33). Koster, L. J. A.; Mihailetchi, V. D.; Blom, P. W. M. *Appl. Phys. Lett.* **2006,** 88, 093511.

(34). Koster, L. J. A.; Mihailetchi, V. D.; Blom, P. W. M. *Appl. Phys. Lett.* **2006,** 88, 052104.

(35). Mihailetchi, V. D.; Koster, L. J. A.; Blom, P. W. M.; Melzer, C.; de Boer, B.; van Duren, J. K. J.; Janssen, R. A. J. *Adv. Funct. Mater.* **2005,** 15, 795.

(36). Goh, C.; Scully, S. R.; McGehee, M. D. *J. Appl. Phys.* **2007,** 101, 114503.

(37). Haick, H.; Ambrico, M.; Ligonzo, T.; Cahen, D. *Adv. Mater.* **2004,** 16, 2145.

(38). Goodman, A. M.; Rose, A. *J. Appl. Phys.* **1971,** 42, 2823.

(39). Mihailetchi, V. D.; Koster, L. J. A.; Hummelen, J. C.; Blom, P. W. M. *Phys. Rev. Lett.* **2004,** 93, 216601.

(40). Dennler, G.; Forberich, K.; Scharber, M. C.; Brabec, C. J.; Tomis, I.; Hingerl, K.; Fromherz, T. *J. Appl. Phys.* **2007,** 102, 054516.

(41). Kotlarski, J. D.; Blom, P. W. M.; Koster, L. J. A.; Lenes, M.; Slooff, L. H. *J. Appl. Phys.* **2008,** 103, 084502.

(42). Uhrich, C.; Wynands, D.; Olthof, S.; Riede, M. K.; Leo, K.; Sonntag, S.; Maennig, B.; Pfeiffer, M. *J. Appl. Phys.* **2008,** 104, 043107.

(43). Tikhodeev, S. G.; Yablonskii, A. L.; Muljarov, E. A.; Gippius, N. A.; Ishihara, T. *Phy. Rev. B* **2002,** 66, 45102.

(44). Palik, E. D.; Ghosh, G. E., *Handbook of Optical Constants of Solids*. Academic Press: New York, 1998.

(45). Takahashi, M.; Tsukigi, K.; Uchino, T.; Yoko, T. *Thin Solid Films* **2001,** 388, 231.

(46). Verbakel, F.; Meskers, S. C. J.; Janssen, R. A. J. *J. Appl. Phys.* **2007,** 102, 083701.

(47). Verbakel, F.; Meskers, S. C. J.; Janssen, R. A. J. *Appl. Phys. Lett.* **2006,** 89, 102103.

(48). Shuttle, C. G.; O'Regan, B.; Ballantyne, A. M.; Nelson, J.; Bradley, D. D. C.; Durrant, J. R. *Phys. Rev. B* **2008,** 78, 113201.

(49). Servaites, J. D.; Yeganeh, S.; Marks, T. J.; Ratner, M. A. *Adv. Funct. Mater.* **Early View,** DOI: 10.1002/adfm.200901107.

(50). Schilinsky, P.; Waldauf, C.; Hauch, J.; Brabec, C. J. *J. Appl. Phys.* **2004,** 95, 2816.

(51). Waldauf, C.; Schilinsky, P.; Hauch, J.; Brabec, C. J. *Thin Solid Films* **2004,** 451-452, 503.

(52). Shuttle, C. G.; Maurano, A.; Hamilton, R.; O'Regan, B.; de Mello, J. C.; Durrant, J. R. *Appl. Phys. Lett.* **2008,** 93, 183501.

(53). Huynh, W. U.; Dittmer, J. J.; Teclemariam, N.; Milliron, D. J.; Alivisatos, A. P.; Barnham, K. W. J. *Phys. Rev. B* **2003,** 67, 115326.

(54). Koster, L. J. A.; Mihailetchi, V. D.; Xie, H.; Blom, P. W. M. *Appl. Phys. Lett.* **2005,** 87, 203502.

(55). Nelson, J., *The Physics of Solar Cells*. Imperial College Press: London, 2003.

Chapter V

GENERAL CONCLUSIONS
AND
FUTURE RESEARCH DIRECTIONS

5.1 General Conclusions

The light trapping system is a promising method to improve OPV performance. The photonic crystals (PC) would be the best choice for the possible light trapping system because they provide unique properties to control propagation of the light as a waveguide. In addition, excitations of resonance modes in PC offer the benefit of being able to target the desired wavelength of the solar spectrum for further absorption enhancement. The fact that absorption and electrical performance can be improved simultaneously using the PC structures makes the PC approach for OPV more valuable. Also, this approach is not restricted to any particular type of solar cell and presumably even inorganic solar cells are expected to be improved in this way. Moreover, our route to the 2-D photonic crystal is scalable via a facile processing strategy called PRINT, Pattern Replication In Non-wetting Templates,[1] where nanofabrication of PC OPVs can be achieved over large area at low cost.

Incorporating UV-sensitive electron transport layers (ETL) into organic bulk heterojunction (BHJ) photovoltaic devices significantly affect physical processes in the BHJ photoactive material. Resistivity changes induced by UV illumination in the ETL of inverted BHJ devices suppress bimolecular recombination via a profound effect on serial resistance. Electro-optical modeling and light intensity experiments have shown that the resistivity changes in the ETL effectively controls bimolecular recombination attributed to the diode current.

5.2 Research Directions

We showed potential possibilities to improve OPV performance via PC nanostructures. The PC effects are strongly dependent on physical dimension of nanopattern,

materials, and device architecture;[2] therefore, further improvement for OPV performance would be possible via optimized PC nanostructures and materials.[3, 4] In this chapter, the bio-inspired PC nanostructures for OPV will be introduced with previous theoretical studies, and appropriate photoactive materials for PC organic photovoltaic cells will be discussed.

5.2.1 Bio-inspired Photonic Crystals ('structural' blackness)

Biological photonic crystals have been much attracted a lot of attention due to their complex, but perfect optical system through creatures' evolution. In specific, the brilliant metallic blue wings of *Papilio Ulysses* butterflies have been well studied.[5] It is interesting that the blue luster produced from the butterfly's scale is originated, not from blue pigment, but rather from nanoscale structure. This color from nanoscale structure, which is called as structural color, is created from photonic crystal structure in *Papilio Ulysses* butterfly scale, as shown in Figure 5.1. These photonic crystals in butterfly appear brightly colored as they act as a mirror to reflect light of that color. Therefore, this principle provides potential possibility to confine light within a device.

In addition to the blue metallic color in the butterfly wings, the absence of reflection in insect exocuticles is very striking: The matt black exhibited by the *Papilio Ulysses* butterfly is a case in point. Vukusic et al.[6] have shown that the absorption characteristics of the *Papilio Ulysses* butterfly wing is derived not from pigments, but from a very specific ultra-structure on the surface of the wing scales: The scale surface is composed of optimally-spaced, parallel ridges wherein each ridge is itself ribbed, i.e., the ridge has a "corrugated" triangular cross section (see electron microscope image c.). This absorbance-assisted structure of black scale

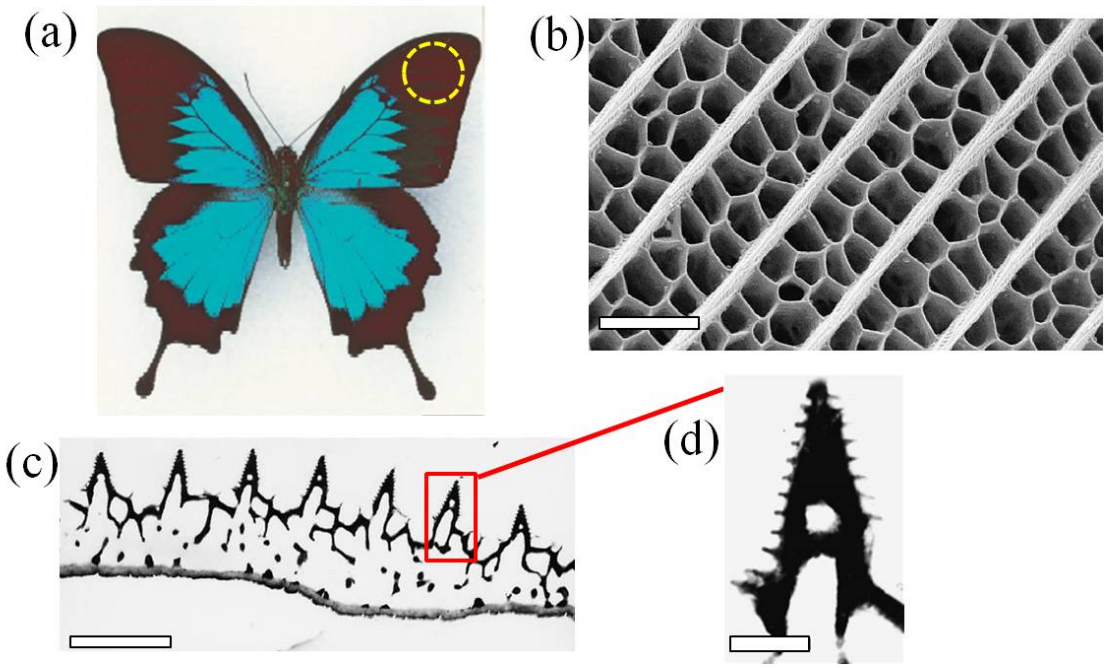

Figure 5.1. (a) *Papilio Ulysses* butterfly,[7] (b) SEM images of the surface of a black scale indicated by the yellow circle of (a), (c, d) TEM images of the cross-section through a black scale. Scale bars: (b) 2μm, (c) 2μm (d) 300nm[6]. (The photograph and SEM images are taken from references 6 and 7.)

consists of periodic ridges, of pitch 2~3μm, wherein each ridge is itself ribbed and tapered with corrugated structure (Figure 5.1 (b) and (c)). Through the tapering of the ridge, a gradual transition of optical impedance from one medium to the next is possible and results in reducing back-reflection.

Herein I propose to replicate an idealized form of this ultra-structure, one with optimally spaced corrugated ridges that are designed to trap incident light when interfaced in a photovoltaic cell geometry.

The biologically inspired light-trapping ultra-structure based on that observed in butterfly scales would be fabricated by using PRINT methodology.[1] The master template with desired rib spacing **p** will be made by taking advantage of differential etching rates of two-component, lamellar (dielectric-mirror-like) monoliths, with component thicknesses governed by *p*. This corrugated ultra-structure would be fabricated from a sol-gel precursor to give a metal oxide (TiO_2, ZnO etc.)[8] base suitable for enabling either solid state organic (P3HT polymer) or "wet" dye-electrolyte Gratzel cells. The initial target structure is shown in Figure 5.2. The critical periodicities **P** and *p* will be optimized to trap light with wavelengths longer than the primary absorption maximum of the polymer/dye. This optimization will be carried out using theoretical modeling through the FDTD (Finite Difference Time Domain) method in conjunction with input consisting of the refractive indices of the components (i.e. for TiO_2 and the polymer or dye-electrolyte). The punctuated base on which the corrugated ridges lie can be PRINTed from molds derived from AAO membranes[9] or a photo-lithographically produced master template. The ultra-structure will be "backfilled" with polymer such as P3HT in the case of solid state OPV cells or, coated with a dye and backfilled with the redox couple/electrolyte in the case of a Gratzel cell[10].

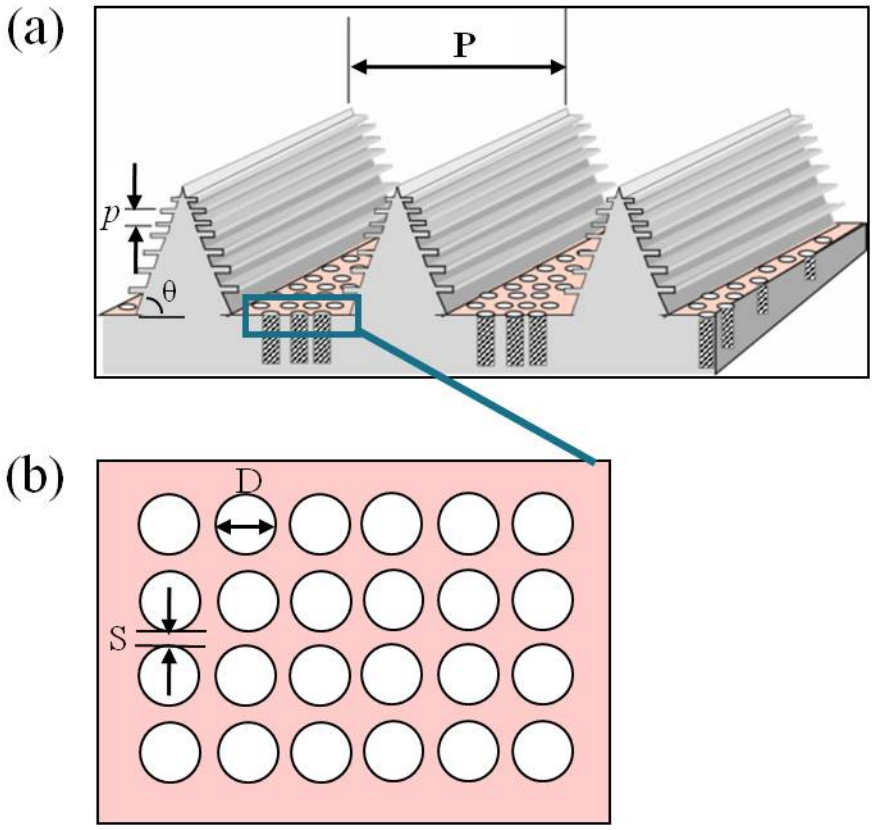

Figure 5.2. Bio-inspired light-trapping ultra structure. (a) Rib spacing (**P**), lamellar pitch (*p*) and tapering of ridge (θ) is optimized to trap long wavelength light and localize light in the absorbing material, and therefore make higher absorbance of incident light.; (b) Magnified structure (top view) of blue rectangle region in (a). Diameter of puncture (**D**) and spacing (**S**) between neighboring puncture is designed to confine the diffracted lights inside the holes.

In principal, there are five parameters in the nanostructure in Figure 5.2 to efficiently trap light; namely, rib spacing (P), lamellar pitch (p) and tapering(θ) of ridge are optimized to trap long wavelength light and localize light in the photoactive material, and therefore make higher absorbance of incident light. In particular, the lamellar pitch is especially related to the multilayer interference. For example, the lamellar structure in butterfly can be understood as an antireflection coating with simple model shown in Figure 5.3.

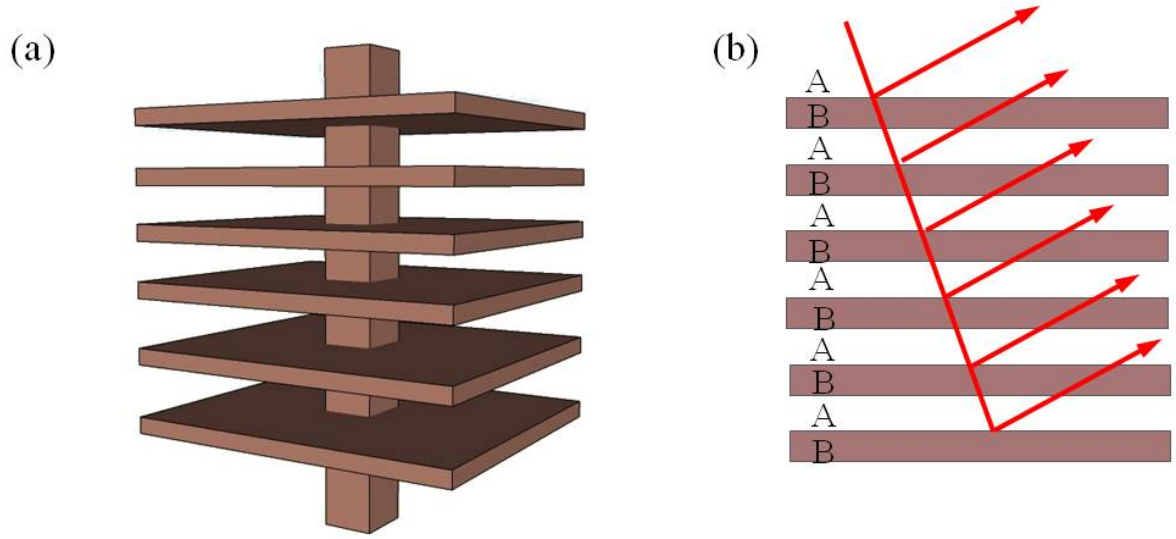

Figure 5.3. Configuration of the multilayer interference. (a) Lamellar structure in butterfly, (b) Simplified model of lamellar structure. In the simplified model, the incident light is reflected on each layer.

From multilayer interference, the relation of constructive interference condition can be gained, as shown in the equation (5.1).

$$2(n_A d_A \cos\theta_A + n_B d_B \cos\theta_B) = m\lambda \qquad (5.1)$$

where the angles of refraction in layer A and B are θ_A and θ_B, respectively, and n_A and n_B are refractive indexes of each layer, and d_A and d_B are layer thickness.

S. Kinoshita et al[11] reported that the system with infinite numbers of layers can be taken as 1D photonic crystal, and high reflection band center (λ_c) can be calculated from the equation (5.2).

$$\lambda_c = 2a / \sqrt{\frac{1}{n_B^2}\left(1 + \frac{n_B^2 - n_A^2}{n_B^2} X_A\right)} \qquad (5.2)$$

where a is the period of multilayer, X_A is the ratio of thickness of the layers A and B to their sum, and n_A and n_B are refractive index of each layer A. In the case that the heights of the ridges in butterfly are not so regular as shown in Figure 5.1, the light diffracted at each ridge is randomly superimposed and no interference should occur. Then, the reflection intensity also can be calculated by the simplified model as shown in Figure 5.4 and equation (5.3)[12].

$$I_\Phi = I_\theta \cdot 2b^2 \frac{\sin^2\left(\frac{kavM}{2}\right)}{\sin^2\left(\frac{kav}{2}\right)} \cdot \frac{\sin^2\left(\frac{kb\mu}{2}\right)}{\left(\frac{kb\mu}{2}\right)^2} \cdot \cos^2\left(\frac{k}{2}(b\mu + av)\right) \cdot \sin^2\theta \qquad (5.3)$$

where I_θ is incident light intensity from θ direction, I_Φ is the reflection intensity from Φ direction, a is the pitch of the layer, b is the layer width, M is the number of layers, $v = \sin\theta + \sin\Phi$, $\mu = \cos\theta + \cos\Phi$ and $k = \lambda/2\pi$. Therefore we can control reflection band center (λ_c) and intensity (I_Φ) by adjustment of the period of multilayer.

In sum, the novel ultra structures may provide a solution to improve the efficiencies of OPV devices and furthermore understand the mechanism employed by nature to efficiently utilize the energy of light.

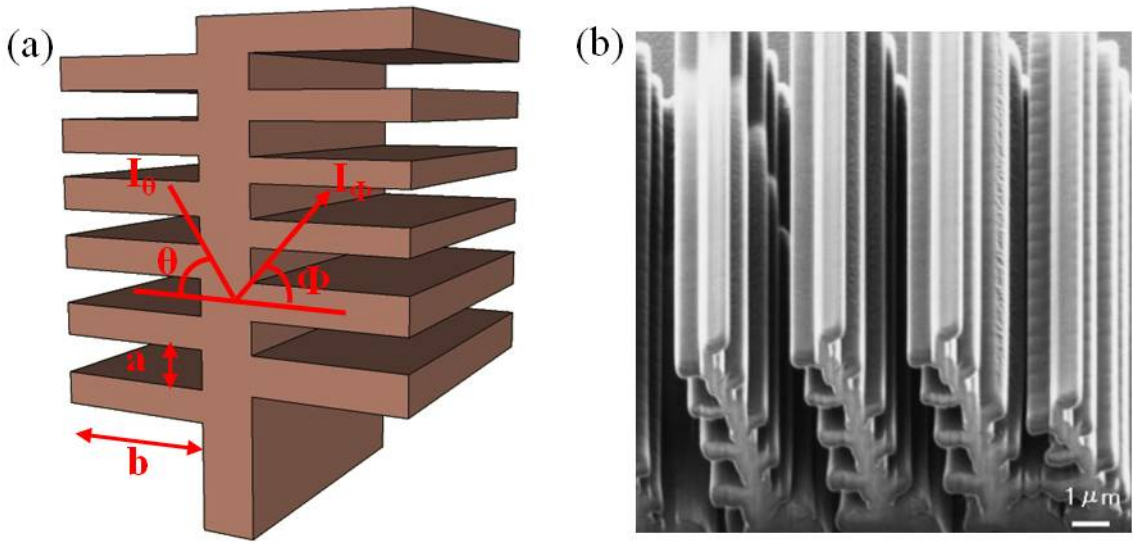

Figure 5.4. (a) Schematic of butterfly scale reflection, (b) SEM image of Morpho-butterfly-scale quasi-structure fabricated by FIB-CVD (focused-ion-beam chemical-vapor-deposition). The SEM image was taken from reference 12.

5.2.2 Photonic crystal organic photovoltaic cells with small band gap photoactive materials

The excitation of resonant modes in PC boosts up the performance for OPV. Optical absorption losses due to the mismatch between the solar spectrum and the band structure of the photoactive materials have led us to design new materials which can capture whole range of the solar spectrum. However, the widely used organic materials such as P3HT or functionalized PPV absorb strongly only over the wavelength range 350~650nm (3.5~1.9eV), whereas the photon flux of the AM1.5G Solar Spectrum peaks around 700nm (1.8eV) as shown in Figure 5.5.[13]

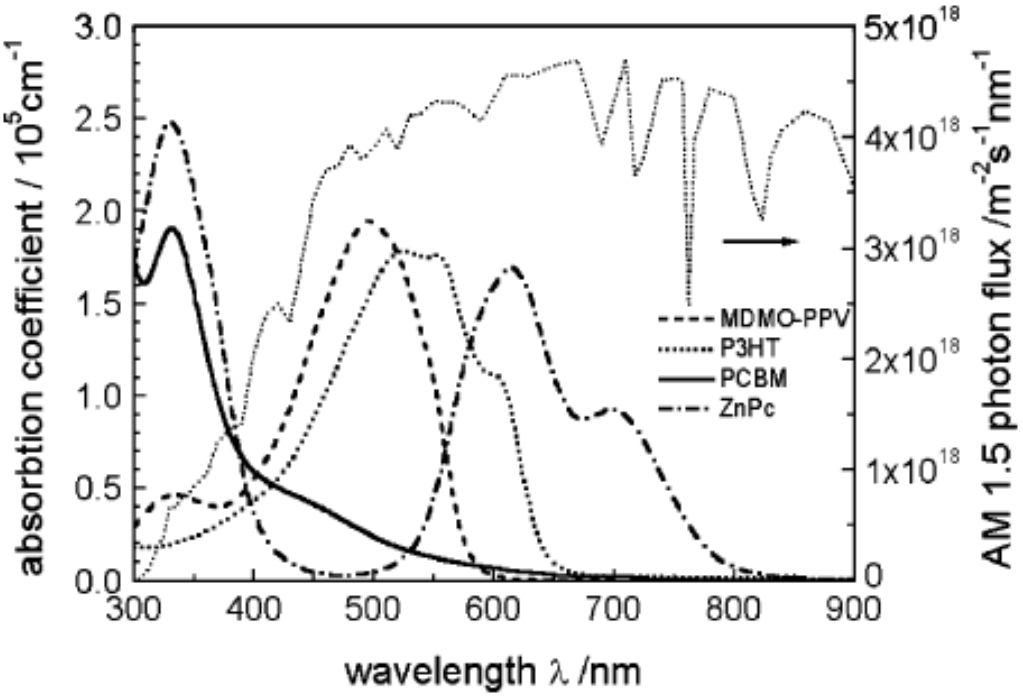

Figure 5.5. Absorbance spectrum of commonly used photoactive materials and the photon flux of the AM 1.5 terrestrial solar spectrum. (Reprinted with permission from reference 13. Copyright 2007 © American Chemical Society.)

Hence, the band gap of organic photoactive materials should be well adjusted. For example, the use of organic photoactive materials with 1.38eV band gap instead of 1.91eV give rise to photon harvesting of about 80% instead of 45% as detailed in Figure 5.5. The keys to lowering absorbance in the 700~900nm range is to increase the photoactive layer thickness or to broaden absorbing range of the organic photoactive layer. From this point of view, small band gap photoactive materials which have a wide range of absorption spectrum have been actively investigated. Peet et al.[14] reported the enhanced performance of OPV with small band gap photoactive materials due to increased absorption of solar spectrum. Recently, Zhou et al.[15] showed a creative way to harness the high wavelength of solar spectrum as well as to maximize the open circuit voltage (V_{oc}) at the same time (Figure 5.6). However, these solutions still have limitation due to increased series resistance with relatively thick photoactive layer. Also the tortuous carrier transport path in BHJ photoactive layer becomes more problematic.

The light trapping scheme with the small band gap photoactive material offers a solution to efficiently improve the performance of the OPV without side effects. As previously discussed in chapter I, the excitation of resonant mode in PC structure provides another possibility to harness the IR region of solar spectrum by resonant mode exictaions. However, the enhanced photocurrents in Chapter I are relatively small due to the extremely low absorption coefficient of the used photoactive material (TDPTD:PCBM) at the resonant mode wavelength. The intrinsic limitation can be solved by incorporating the small band gap photoactive material into the PC cells, which provide flexibility to target desired region of the solar spectrum for absorption enhancements in part through multiple excitation

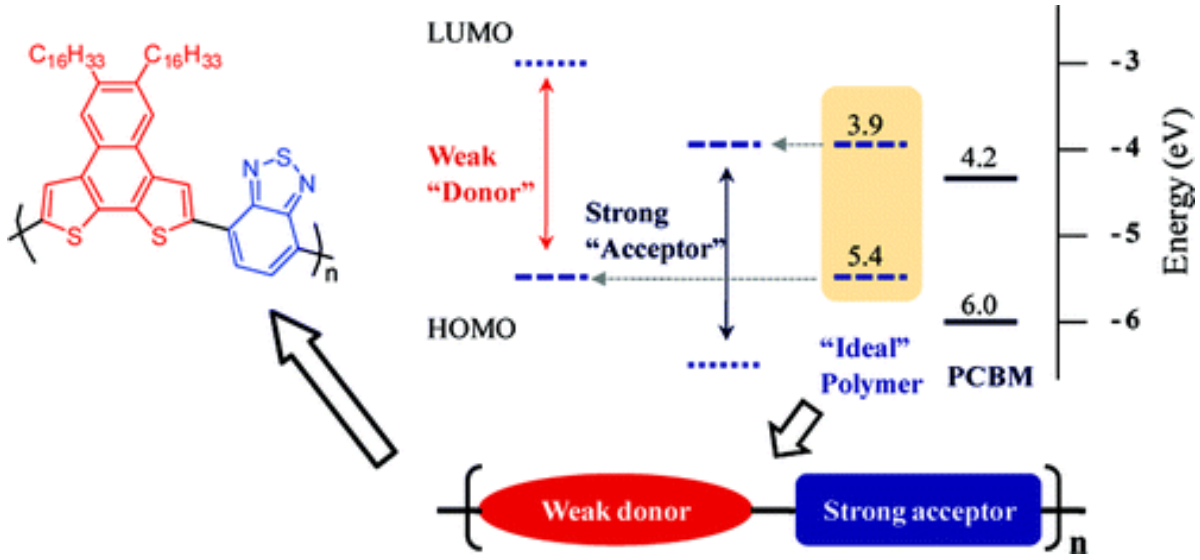

Figure 5.6. Schematic of weak donor - strong acceptor concept and designed photoactive polymer (PNDT-BT).[15] (Reprinted with permission from reference 15, Copyright 2010 © American Chemical Society.)

resonances. For instance, the IR region where solar spectrum has maximum photon flux can be utilized via the excited resonant manners.

Consequently, the PC geometry with the small band gap photoactive material may give an ultimate solution to improve the OPV performances. This approach offers the possibility to increase photocurrents by matching the resonant modes to the absorption spectrum of the photoactive materials via controlling the photonic crystal dimensions[16]. In particular, wide absorption spectrum of the small band gap photoactive materials would provide advantage to harness the IR region of light as well as the visible region. The photonic effects caused by a periodic nanostructure avail the possibility of using thinner layers of the photoactive material which in turn, has the potential advantage of decreasing the series resistance in devices leading to an increase in OPV performance.

5.2.3 Capturing the NIR with QD composites coupled to surface plasmons

QD (Quantum Dot) light absorbance is dot-size dependent[17] and when incorporated into photovoltaic cells yields tangible advantages: i) QD-polymer hybrid PV composites enhance NIR (near infrared) harvesting,[18-20] ii) high efficiency carrier multiplication in the QDs improves PV performance;[21] however reported efficiencies are low due to the low absorbance of QDs[20]. Nobel metal surfaces via the surface plasmon phenomenon can improve solar energy conversion[22, 23] The Plasmon's electromagnetic field propagating along interface of metal-dielectric material is concentrated on the interface. This localized electromagnetic field has been engineered to provide many applications such as surface enhanced Raman Spectroscopy(SERS)[24], extraordinary optical transmission of light through sub-wavelength hole arrays,[25] enhanced semiconductor optical absorption in metal

nanoparticles[26] and enhanced light absorption in QD-metal composite[27] etc. Song et al. [28] reported resonant coupling to spatially controlled surface plasmons in CdSe/ZnS QDs proximate to the surface plasmon polariton (SPP) field generated in a periodic array of Ag nanoparticles. The SPP field using periodic nanostructured metallic surfaced can be generated by PRINT methodology in conjunction with QD composites.

Herein, strong absorbance of NIR through localized surface plasmon can anticipated when the resonant region of surface plasmon is matched to the QD absorbance spectrum. Based on strong absorbance of NIR in QDs, efficient carrier multiplication in the QDs will be studied with effect of localized surface plasmon, and exciton-surface plasmon coupling at metal-dielectric boundary will be investigated experimentally as well as theoretically.

This endeavor is differentiated from other attempts to make nano-scale periodic substrates[29] and observe light localization[30] via the PRINT methodology: wide-area, periodic nano-patterns for surface plasmon effect can be fabricated by patterning the photoactive composite containing QDs by PRINT[1] and subsequent deposition of a metal (Ag, Au and Al) on the patterned PV-active composite. The resulting intimate association between the deposited metal and the QD composite enables one to exploit the surface plasmon effect by using a periodic nano-pattern accurately fabricated by PRINT and resonant to the QDs' absorbance spectrum.

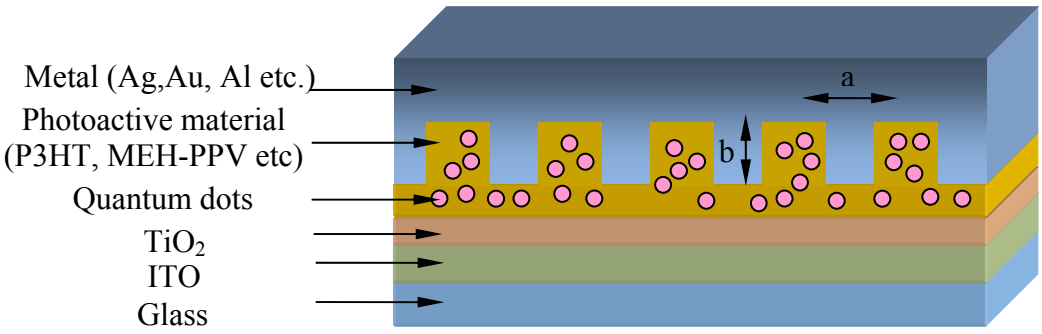

Figure 5.7. Proposed structure of QD embedded photovoltaics. Periodicity (a) and height (b) of nano-pattern is determined by the resonant region of surface plasmon matched to the QD absorbance spectrum

5.2.4 Various PC geometries for OPV cells

As discussed in Chapters 1 and 2, the PC effect comes from different refractive indices between adjacent nanopatterns. Consequently, various PC geometries are fabricated via combination of the used layers in OPV. Here the PRINT technique provides flexibility to fabricate various PC organic photovoltaic cells. In particular, Hampton et al.[8] reported the sub-500nm patterns of various metal oxides by PRINT as shown in Figure 5.8. These nanopatterned metal oxides can be incorporated into the OPV to show a PC behavior with components in OPV.

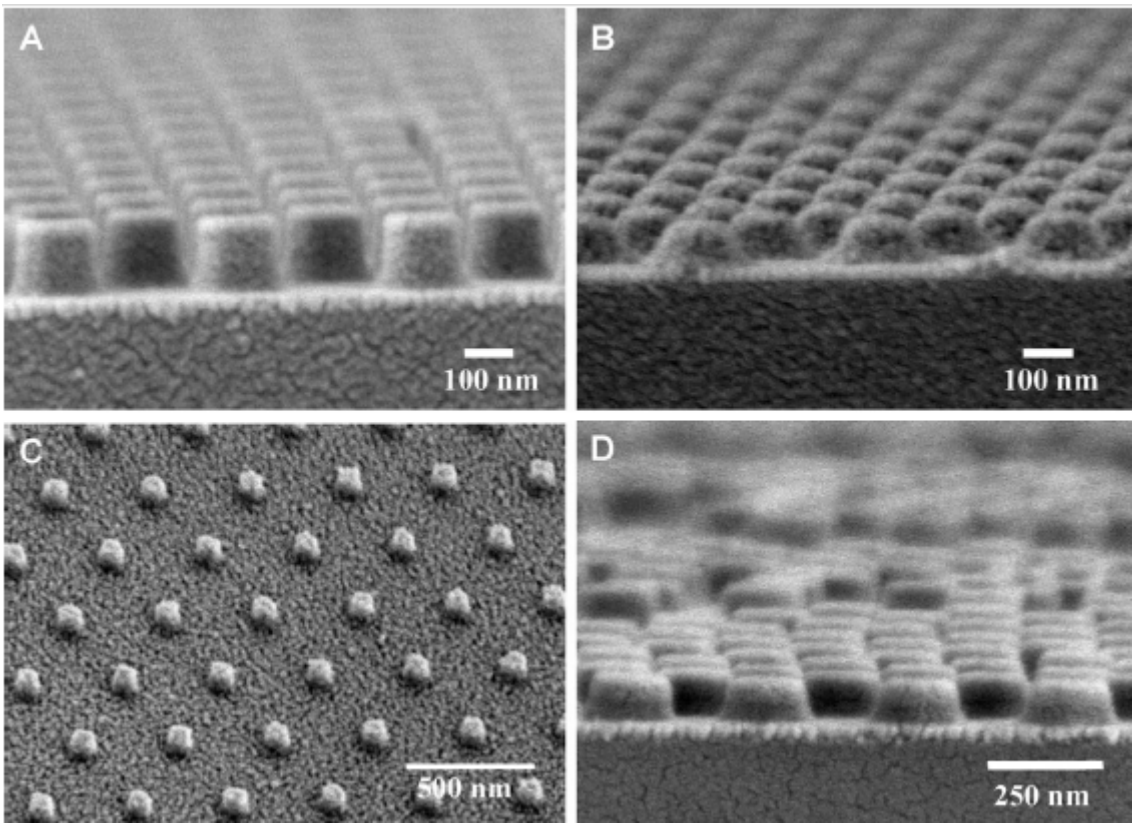

Figure 5.8. SEM images of arrays of various inorganic oxide features on glass made from a 200nm × 200nm mold: (A) SnO_2; (B) ZnO; (C) ITO; (D) $BaTiO_3$. (Reprinted with permission from reference 8, Copyright © 2008 Wiley-VCH Verlag GmbH & Co. KGaA.)

The nanopatterned OPV can be utilized to inquire into the origin of photocurrent generation and electrical loss process in the OPV devices. Blom et al.[31, 32] have reported dependence of exciton dissociation probability on electrical field in OPV devices, showing the dissociation probability in MDMO-PPV:PCBM devices is only 60 % at short circuit current (V=0). Here, the dissociation probability varied according to the internal electric field in the devices where the electric field intensity is dependent on device architecture. Therefore, the nanopatterns of highly conductive material may induce a change of the electric field in OPV and result in variation of the exciton dissociation probability. In the same way, the variation of electric field intensity in the nanopattened OPV may induce a change to the recombination process. Thus, these experiments may provide creative ways to investigate the working theory of OPV and optimize the devices to achieve high performances.

5.3 References

(1). Rolland, J. P.; Maynor, B. W.; Euliss, L. E.; Exner, A. E.; Denison, G. M.; DeSimone, J. M. *J. Am. Chem. Soc.* **2005,** 127, 10096.

(2). Tikhodeev, S. G.; Yablonskii, A. L.; Muljarov, E. A.; Gippius, N. A.; Ishihara, T. *Phy. Rev. B* **2002,** 66, 45102.

(3). Tumbleston, J. R.; Ko, D.-H.; Samulski, E. T.; Lopez, R. *Appl. Phys. Lett.* **2009,** 94, 043305.

(4). Tumbleston, J. R.; Ko, D.-H.; Samulski, E. T.; Lopez, R. *Opt. Express* **2009,** 17, 7670.

(5). Vukusic, P.; Sambles, J. R. *Nature* **2003,** 424, 852.

(6). Vukusic, P.; Sambles, J. R.; Lawrence, C. R. *Proc. R. Soc. Lond. B* **2004,** 271, S237.

(7). Vukusic, P.; Sambles, R.; Lawrence, C.; Wakely, G. *Appl. Opt.* **2001,** 40, 1116.

(8). Hampton, M. J.; Williams, S. S.; Zhou, Z.; Nunes, J.; Ko, D.-H.; Templeton, J. L.; Samulski, E. T.; DeSimone, J. M. *Adv. Mater.* **2008,** 20, 2667.

(9). Zhang, L.; Cheng, B.; Shi, W.; Samulski, E. T. *J. Mater. Chem.* **2005,** 15, 4889.

(10). O'Regan, B.; Grätzel, M. *Nature* **1991,** 353, 737.

(11). Kinoshita, S.; Yoshioka, S. *ChemPhysChem* **2005,** 6, 1442.

(12). Watanabe, K.; Hoshino, T.; Kanda, K.; Haruyama, Y.; Matsui, S. *Jpn. J. Appl. Phys.* **2005,** 44, L48.

(13). Günes, S.; Neugebauer, H.; Sariciftci, N. S. *Chem. Rev.* **2007,** 107, 1324.

(14). Peet, J.; Kim, J. Y.; Coates, N. E.; Ma, W. L.; Moses, D.; Heeger, A. J.; Bazan, G. C. *Nature Mater.* **2007,** 6, 497.

(15). Zhou, H.; Yang, L.; Stoneking, S.; You, W. *ACS Appl. Mater. Interfaces* **2010,** 2, 1377.

(16). Gippius, N. A.; Tikhodeev, S. G.; Ishihara, T. *Phys. Rev. B* **2005,** 72.

(17). Huynh, W. U.; Dittmer, J. J.; Alivisatos, A. P. *Science* **2002,** 295, 2425.

(18). McDonald, S. A.; Konstantatos, G.; Zhang, S.; Cyr, P. W.; Klem, E. J. D.; Levina, L.; Sargent, E. H. *Nature Mater.* **2005,** 4, 138.

(19). Thapa, R.; Choudhury, K. R.; Kim, W. J.; Sahoo, Y.; Cartwright, A. N.; Prasad, P. N. *Appl. Phys. Lett.* **2007,** 90, 252112.

(20). Cui, D.; Xu, J.; Zhu, T.; Paradee, G.; Ashok, S.; Gerhold, M. *Appl. Phys. Lett.* **2006,** 88, 183111.

(21). Schaller, R. D.; Klimov, V. I. *Phys. Rev. Lett.* **2004,** 92, 186601.

(22). Morfa, A. J.; Rowlen, K. L.; Reilly, T. H.; Iii; Romero, M. J.; van de Lagemaat, J. *Appl. Phys. Lett.* **2008,** 92, 013504.

(23). Hagglund, C.; Zach, M.; Kasemo, B. *Appl. Phys. Lett.* **2008,** 92, 013113.

(24). Johannessen, C.; White, P. C.; Abdali, S. *J. Phys. Chem. A* **2007,** 111, 7771.

(25). Ebbesen, T. W.; Lezec, H. J.; Ghaemi, H. F.; Thio, T.; Wolff, P. A. *Nature* **1998,** 391, 667.

(26). Schaadt, D. M.; Feng, B.; Yu, E. T. *Appl. Phys. Lett.* **2005,** 86, 063106.

(27). Ma, G. H.; He, J.; Rajiv, K.; Tang, S. H.; Yang, Y.; Nogami, M. *Appl. Phys. Lett.* **2004,** 84, 4684.

(28). Song, J.-H.; Atay, T.; Shi, S.; Urabe, H.; Nurmikko, A. V. *Nano Lett.* **2005,** 5, 1557.

(29). Noginov, M. A.; Zhu, G.; Bahoura, M.; Adegoke, J.; Small, C.; Ritzo, B. A.; Drachev, V. P.; Shalaev, V. M. *App. Phys. B* **2007,** 86, 455.

(30). Peyrade, D.; et al. *Europhys. Lett.* **2001,** 56, 517.

(31). Blom, P. W. M.; Mihailetchi, V. D.; Koster, L. J. A.; Markov, D. E. *Adv. Mater.* **2007,** 19, 1551.

(32). Mihailetchi, V. D.; Koster, L. J. A.; Hummelen, J. C.; Blom, P. W. M. *Phys. Rev. Lett.* **2004,** 93, 216601.